NOTICE

The quality of this microform is heavily dependent upon the quality of the original thesis submitted for microfilming. Every effort has been made to ensure the highest quality of reproduction possible.

If pages are missing, contact the university which granted the degree.

Some pages may have indistinct print especially if the original pages were typed with a poor typewriter ribbon or if the university sent us an inferior photocopy.

Reproduction in full or in part of this microform is governed by the Canadian Copyright Act, R.S.C. 1970, c. C-30, and subsequent amendments.

AVIS

La qualité de cette microforme dépend grandement de la qualité de la thèse soumise au microfilmage. Nous avons tout fait pour assurer une qualité supérieure de reproduction.

S'il manque des pages, veuillez communiquer avec l'université qui a conféré le grade.

La qualité d'impression de certaines pages peut laisser à désirer, surtout si les pages originales ont été dactylographiées à l'aide d'un ruban usé ou si l'université nous a fait parvenir une photocopie de qualité inférieure.

La reproduction, même partielle, de cette microforme est soumise à la Loi canadienne sur le droit d'auteur, SRC 1970, c. C-30, et ses amendements subséquents.

STUDY OF THE FLOW CHARACTERISTICS IN THE ABDOMINAL AORTA

KONSTANTINOS STAVRIANOS

A Thesis

in

the Department

of

Mechanical Engineering

Presented in Partial Fulfillment of the Requirements
for the Degree of Master of Engineering at
Concordia University
Montreal, Quebec, Canada

September 1989

ISBN 0-315-51397-7

ABSTRACT

STUDY OF THE FLOW CHARACTERISTICS
IN THE ABDOMINAL AORTA

KONSTANTINOS STAVRIANOS

The abdominal aorta is prone to atherosclerosis. Hemodynamic factors are known to be directly related to the development of the disease. Numerical solutions of steady, unsteady harmonic, and physiological flows in simplified aortic models are presented. The effects of Reynolds number, angle of the divider, amplitude and frequency of oscillation and unsymmetry of the inlet velocity on the development of velocity profiles, separation zones and wall shear are investigated. The results obtained are confirmed with the work previously published by the other researchers. During steady flow, no reverse flow regions and oscillatory (in space) wall shear behaviour are found in areas known to be subjected to atherogenesis. During flow deceleration, in the case of physiological flow conditions, these areas have been found to be under the influence of large recirculation zones and time varying oscillations. No stagnation points and space oscillations occur during flow acceleration.

ACKNOWLEDGEMENTS

The author expresses his appreciation to his supervisor, Professor G.H. Vatistas for his guidance and valuable advises throughout the course of this investigation.

Sincere thanks go to Dr. A.M. Graham of the Royal Victoria Hospital who partially supported the project and who provided the author with information relevant to his medical expertise. For typing the manuscript, thanks are extended to Miss. Jayne Claassen.

The author is deeply grateful to his parents, Christos and Vera, and his wife Eftichia for their love, patience and encouragement.

TABLE OF CONTENTS

CHAPTER FOUR

CHAPTER FIVE

LIST OF TABLES

LIST OF FIGURES

NOMENCLATURE

A	Amplitude of flow rate oscillation [m^3/sec]
A_{IN}	Dimensionless cross-sectional area at inlet
A_R	Daughter-to-parent branch area ratio
C_f	Skin friction coefficient
D	Divergence of cell
e	Eccentricity of maximum velocity [m]
FUX,FUY,FVX,FVY	Convective fluxes
g	Gravitational acceleration [m/sec^2]
h_1,h_2,h_3,h_4,h_5	Dimensionless height (see Fig. 5)
$\bar{h}_1,\bar{h}_2,\bar{h}_3,\bar{h}_4,\bar{h}_5$	Height [m], (see Fig. 5)
l_1,l_2l_3	Dimensionless length (see Fig. 5)
$\bar{l}_1,\bar{l}_2,\bar{l}_3,$	Length [m], (see Fig. 5)
p	Dimensionless pressure
$\bar{p}$	Pressure [kPa]
q	Dimensionless velocity, parallel to the wall
Q_1,Q_2,Q_3,Q_4,Q_5	Flow rate [m^3/sec], (see Fig. 4)
Q_{1MEAN}	Average input flow rate for pulsatile flow [m^3/sec]
Re	Reynolds number
St	Strouhal number
T	Transit time [sec]
t	Dimensionless time
$\bar{t}$	Time [sec]
u	Dimensionless velocity in x-direction
$\bar{u}$	Velocity in x-direction [m/sec]
u_{av}	Dimensionless average velocity in x-direction

u_{IN}	Dimensionless inlet velocity in x-direction
v	Dimensionless velocity in y-direction
$\bar{v}$	Velocity in y-direction [m/sec]
VISX,VISY	Viscous fluxes
x	Dimensionless cartesian coordinate
$\bar{x}$	Cartesian coordinate [m]
y	Dimensionless cartesian coordinate
$\bar{y}$	Cartesian coordinate [m]

Greek Symbols

α	Donor cell constant, Womersley parameter
Δx	Dimensionless increment in x-direction [$= \delta x/\bar{h}_1$]
δx	Distance increment in x-direction [m]
Δy	Dimensionless increment in y-direction [$= \delta y/\bar{h}_1$]
δy	Distance increment in y-direction [m]
δt	Time increment [sec]
δp	Pressure difference [kPa]
ϵ	Small scalar parameter
η	Distance in the inwards, normal to the wall
ν	Kinematic viscosity [m/sec^2]
ξ	Dimensionless distance along the walls
$\bar{\xi}$	Distance along the walls [m]
ρ	Density [kg/m^3]
ϕ	Angle of flow divider
ω	Over-relaxation factor

Subscripts

i,j	Mesh points indexes
IN	Inlet conditions
max	Maximum values
min	Minimum values
MEAN	Average values

Superscripts

n, n+1	Previous and updated value of the variable

CHAPTER ONE

INTRODUCTION

1.1 History of Hemodynamic Research

Early records in Egyptian hieroglyphics and Greek and Roman manuscripts indicate the interest of man to acquire knowledge of the anatomy of the major blood vessels and the mechanics of the circulation. The old theories were sustained until the Renaissance, when studies in anatomy led the way to the modern scientific approach [1].

At that period Leonardo da Vinci illustrated the great vessels of man, see Fig. 1, and remarked on the thickening and hardening of the arterial walls with age, which we now call atherosclerosis. William Harvey, an English physician, presented the modern conception of the circulation of blood [1].

Later in the eighteenth and in the nineteenth centuries, well known fluid dynamicists, such as Euler, and recognized polymaths who paid little regard to the distinction between biological and physical science, such as Bernoulli, Poiseuille and Young, made significant contributions to our understanding of hemodynamics [2].

By the beginning of the twentieth century, the development of science and specialization created a separation between the physical science and the study of the cardiovascular system. Physiological researchers were lacking in mathematics and mechanics while physical scientists found the complexity, empiricism and terminology of physiological studies restricting [3].

As a result there was limited advancement in the study of blood hydrodynamics, i.e. hemodynamics, until the mid 1960's. During that era vascular surgery became common and created a need to broaden the subject of cardiovascular fluid dynamics and to master the details of flow through branches. The shortage of information caused engineers,

physicians and physicists to form teams in order to provide answers to questions such as, how the circulatory diseases were generated and how surgical implants interfere with the normal function of the system [4].

1.2 Atherosclerosis and Hypotheses for the Etiology of the Disease

A term that designates a variety of conditions that cause arterial walls to become thickened and hardened is arteriosclerosis. Atherosclerosis is a type of arteriosclerosis. Many different risk factors such as family history, high cholesterol, diets rich in saturated fat, smoking and elevated blood pressure can injure the endothelium of the arterial wall. The injury causes plasma proteins including lipoproteins and cholesterol to rapidly penetrate into the subendothelial tissues, and platelets and white cells to accumulate on the exposed subendothelial structures. As platelets react with subendothelial constituents they release several factors, such as mitogen, which stimulate both the migration of the smooth muscle cells into the intima and their proliferation. As the intima thickens, it decreases the size of the artery, thus diminishing blood flow and resulting in insufficient supply of oxygen to the organs perfused by the artery, i.e. they produce ischemic damage [5,6].

Atherosclerotic lesions develop in certain areas of the arterial system such as the coronary arteries, the carotid arteries and the abdominal aorta resulting in complications such as heart attack, stroke and peripheral vascular disease [5,7], see Fig. 2.

Certain regions of the arterial tree, such as bifurcations, branchings and curvatures, are particularly prone to develop the disease. The propensity for plaque formation in areas where the local features of the flow profile is affected, has led to the assumption that local mechanical factors of blood flow potentiate atherogenesis. However, for a realistic answer to the etiology of the disease, hemodynamics must be integrated with the biochemical, neurological, hormonal, and pathological influences that interact with and may often dominate the mechanical aspects of blood flow [1,7,8].

Hemodynamic parameters that have been inferred as contributing factors in the development of atherosclerosis include pressure, shear stress, flow separation and turbulence. The pressure hypothesis by Texon et al [39] suggests that atheromatous plaques emerge in regions of low pressure due to a suction action exerted on the surface endothelium. This suction causes a tearing response and damages the adjacent wall layers, with eventual plaque development. However, the model assumes that the transmural pressure is negative, which is very unlikely to occur in the real arterial system and thus making the pressure proposal untenable [9,10].

Two opposing theories have been attained by researchers regarding the influence of wall shear stress on the growth of lesions. Fry [12] proposed that deformation and eventual erosion of the endothelium may occur at sites where the local shear stress is high. Caro et al [13] suggested that early plaques tend to develop in areas of low wall shear. A shear-dependent mass transfer theory put forward by Caro argued the possible reasons for the diverging results [10,11,12,13].

Fox and Hugh [14] debated that zones of stasis form in areas of local flow separation. Lipids are trapped as the bloodstream stagnates locally and ultimately coalesce to form atheromatous plaques. However, the model did not comply with proper geometric similarity [14].

The basic theory for the turbulence hypothesis is given by Mitchell and Schwartz [38], who suggest that turbulent velocity fluctuations cause platelets in the flow to coalesce on the wall. Since the turbulent fluctuations may also cause particles that have coalesced to break up as they move in random fashion, this assumption is questionable and difficult to assess [10].

In conclusion, even though an understanding of the role of blood flow dynamics in atherogenesis has been sought for years, there is no clear answer to what causes the disease.

1.3 Scope of the Thesis

The present study concentrates on the flow in the abdominal aorta. Geometric transitions and wall shear stress variations are suspected of inducing the development of atheromatous lesions, causing severe atherosclerosis beneath the renal arteries. A numerical method scheme is utilized to obtain solutions on a simplified aorta. Flow patterns for steady, pulsatile and physiological flow conditions are analyzed and conformed with those acquired by other researchers.

Wall shear stress distributions are calculated for steady flow in two bifurcation models. One model includes both the renal and iliac arteries, while the other considers only the iliac bifurcation. The effects of Reynold's number, angle of the divider and unsymmetry of the inlet velocity on the coefficient of friction are investigated.

In pulsatile flow the frequency and amplitude of the oscillation are altered, wall shear stress distributions are obtained and the consequences of these variations are examined. Finally, velocity profiles and wall shear stress distributions are determined for straight pipe and bifurcation models under physiological flow conditions.

CHAPTER TWO

THE PROBLEM

2.1 Assumptions and Model Description

The aorta is the main elastic artery that provides the internal organs and lower extremities of the body with their blood supply. It is composed of the ascending aorta, the aortic arch, the thoracic aorta and the abdominal aorta. The latter refers to the continuation of the thoracic aortic segment through the abdominal cavity [3], see Fig. 3.

Any attempt to theoretically determine a solution of the flow through the aorta encounters complexities due to the rheological properties of the fluid, the nature of the flowfield and the geometry of the area. It seems inevitable that, in order to attain any explanation, certain assumptions must be made. A schematic of an idealized abdominal aortic segment including parts of the renal and iliac arteries is shown in Fig. 4.

Blood is assumed to be an incompressible, homogeneous, Newtonian fluid. The Fahreus-Lindquist effect, which is characterized by viscosity variations, is significant only when the vessel diameter is less than one milimeter, while the aorta is approximately seventeen milimeters in diameter [15,16].

The flow is supposed to be two-dimensional and laminar. Even though it is well known that arterial junctions have a complex three-dimensional geometry, a two-dimensional approximation is made in order to facilitate the mathematical analysis of the flow and reduce the computational time required for a numerical solution. Favourable conditions for the turbulence exist in large arteries. However, velocities exceed their critical value for short periods of time only and there is no certainty that fully developed turbulence is ever attained. This uncertainty supports the laminar assumption [16].

The aortic wall is considered to be rigid and with a constant diameter. The distensibility of the aorta is quite small and its effect is minimal. Although the artery tapers, an average value of the diameter is calculated [3,16,17]. Precise measurements of the arterial dimensions are difficult to obtain due to the dilatation of the segment when it is removed from the body. There is also variation in size with age and sex. The geometry of the simplified problem is shown in Fig. 5 and the relative dimensions, obtained from a replica of the aorta taken from a middle aged male, are given in Table 1. Finally typical experimental measurements of flow division and geometry in the aorta are shown in Table 2 [13,18].

2.2 Governing Equations

The conservative forms of the equations of motion that describe the flow in the abdominal aorta, after incorporating all the previously mentioned simplifying assumptions, are [19]:

$$\text{continuity: } \frac{\partial \bar{u}}{\partial \bar{x}} + \frac{\partial \bar{v}}{\partial \bar{y}} = 0 \tag{1}$$

$$\text{x-momentum: } \frac{\partial \bar{u}}{\partial \bar{t}} + \bar{u}\frac{\partial \bar{u}}{\partial \bar{x}} + \bar{v}\frac{\partial \bar{u}}{\partial \bar{y}} = -\frac{1}{\rho}\frac{\partial \bar{p}}{\partial \bar{x}} + \nu\left\{\frac{\partial^2 \bar{u}}{\partial \bar{x}^2} + \frac{\partial^2 \bar{u}}{\partial \bar{y}^2}\right\} \tag{2}$$

$$\text{y-momentum: } \frac{\partial \bar{v}}{\partial \bar{t}} + \bar{u}\frac{\partial \bar{v}}{\partial \bar{x}} + \bar{v}\frac{\partial \bar{v}}{\partial \bar{y}} = -\frac{1}{\rho}\frac{\partial \bar{p}}{\partial \bar{y}} + \nu\left\{\frac{\partial^2 \bar{v}}{\partial \bar{x}^2} + \frac{\partial^2 \bar{v}}{\partial \bar{y}^2}\right\} \tag{3}$$

To transform the equations in non-dimensional forms, let:

$$u = \frac{\bar{u}}{u_{AV}}\ ,\ v = \frac{\bar{v}}{u_{AV}}\ ,\ x = \frac{\bar{x}}{h_1}\ ,\ y = \frac{\bar{y}}{h_1}\ ,\ t = \frac{\bar{t}}{T} \tag{4}$$

where $u_{AV} = \iint_{A_{in}} u_{IN}\ dA_{in}$

After substituting (4) into (1), (2) and (3):

$$\text{continuity: } \frac{\partial u}{\partial x} + \frac{\partial v}{\partial y} = 0 \tag{5}$$

$$\text{x-momentum: } \frac{u_{AV}}{T}\frac{\partial u}{\partial t} + \frac{u_{AV}^2}{h_1} u \frac{\partial u}{\partial x} + \frac{u_{AV}^2}{h_1} v \frac{\partial u}{\partial y} = -\frac{1}{\rho h_1}\frac{\partial \bar{p}}{\partial x} + \nu \frac{u_{AV}}{h_1^2}\left\{\frac{\partial^2 u}{\partial x^2} + \frac{\partial^2 u}{\partial y^2}\right\} \tag{6}$$

$$\text{y-momentum: } \frac{u_{AV}}{T}\frac{\partial v}{\partial t} + \frac{u_{AV}^2}{h_1} u \frac{\partial v}{\partial x} + \frac{u_{AV}^2}{h_1} v \frac{\partial v}{\partial y} = -\frac{1}{\rho h_1}\frac{\partial \bar{p}}{\partial y} + \nu \frac{u_{AV}}{h_1^2}\left\{\frac{\partial^2 v}{\partial x^2} + \frac{\partial^2 v}{\partial y^2}\right\} \tag{7}$$

Multiply equations (6) and (7) by $\frac{h_1}{u_{AV}^2}$ to get:

$$\text{x-momentum: } \frac{h_1}{u_{AV}T}\frac{\partial u}{\partial t} + \frac{\partial u^2}{\partial x} + \frac{\partial uv}{\partial y} = -\frac{\partial(\bar{p}/\rho u_{AV}^2)}{\partial x} + \frac{\nu}{u_{AV}h_1}\left\{\frac{\partial^2 u}{\partial x^2} + \frac{\partial^2 u}{\partial y^2}\right\} \tag{8}$$

$$\text{y-momentum: } \frac{h_1}{u_{AV}T}\frac{\partial v}{\partial t} + \frac{\partial vu}{\partial x} + \frac{\partial v^2}{\partial y} = -\frac{\partial(\bar{p}/\rho u_{AV}^2)}{\partial y} + \frac{\nu}{u_{AV}h_1}\left\{\frac{\partial^2 v}{\partial x^2} + \frac{\partial^2 v}{\partial y^2}\right\} \tag{9}$$

To obtain the final forms, let:

$$\text{Re} = \frac{u_{AV}h_1}{\nu}\ ,\ P = \frac{\bar{p}}{\rho u_{AV}^2}\ ,\ \text{St} = \frac{h_1}{u_{AV}T}\ ,\ \nabla^2 = \frac{\partial^2}{\partial x^2} + \frac{\partial^2}{\partial y^2}$$

where Re and St are the non-dimensional Reynolds and Strouhal numbers respectively. The former number relates the inertial forces in the fluid to the viscous forces. A critical Re number classifies flows as laminar, transient or turbulent. The latter number is used in studing the vibrations of a body past while a fluid is flowing [20]. Substituting in equations (5), (8), (9)

continuity: $$\frac{\partial u}{\partial x} + \frac{\partial v}{\partial y} = 0 \tag{10}$$

x-momentum: $$St\frac{\partial u}{\partial t} + \frac{\partial u^2}{\partial x} + \frac{\partial uv}{\partial y} = -\frac{\partial p}{\partial x} + \frac{1}{Re}\nabla^2 u \tag{11}$$

y-momentum: $$St\frac{\partial v}{\partial t} + \frac{\partial vu}{\partial x} + \frac{\partial v^2}{\partial y} = -\frac{\partial p}{\partial y} + \frac{1}{Re}\nabla^2 v \tag{12}$$

CHAPTER 3

NUMERICAL SOLUTION PROCEDURE

3.1 The Method

The governing partial differential equations are mathematically classified as parabolic (in time). Parabolic equations are associated with diffusion processes and require a marching procedure to obtain the solution. Beginning with initial conditions for the velocity and pressure throughout the closed domain, a time marching technique is used to advance the flowfield forward in time until steady-state is reached [21,22].

The Navier-Stokes equations can be solved numerically either directly or indirectly. The first method solves for velocities (u and v) and pressure while the second for the stream and vorticity functions. The numerical method employed belongs to the first category, and uses the forward time, centered-space difference scheme.

The finite difference mesh used is shown in Fig. 6. The grid consists of rectangular cells of length δx and width δy. The region containing fluid is bound by the darker lines and is surrounded by a single layer of imaginary boundary cells. The horizontal component of the velocity (u) is located at the middle of the vertical sides of the cell, the vertical velocity component (v) at the middle of the horizontal sides and the pressure (p) at the cell center [23], see Fig. 7.

The difference equations approximating the governing equations (10), (11), and (12) are:

$$\text{continuity: } \frac{1}{\delta x}(u_{i,j}^{n+1} - u_{i-1,j}^{n+1}) + \frac{1}{\delta y}(v_{i,j}^{n+1} - v_{i,j-1}^{n+1}) = 0 \tag{13}$$

$$\text{x-momentum: } u_{i,j}^{n+1} = u_{i,j}^{n} + \delta t \left[\frac{1}{\delta x}(p_{i,j}^{n} - p_{i+1,j}^{n}) - FUX - FUY + VISX\right] \tag{14}$$

$$\text{y-momentum: } v_{i,j}^{n+1} = v_{i,j}^{n} + \delta t \left[\frac{1}{\delta y}(p_{i,j}^{n} - p_{1,j+1}^{n}) - FVX - FVY + VISY\right]$$

where the convective (FUX, FUY, FVX, FVY) and viscous (VISX, VISY) fluxes are defined as:

$$FUX = \frac{1}{4\delta x}\left[(u_{i,j} + u_{i+1,j})^2 + \alpha\left|u_{ij} + u_{i+1,j}\right|(u_{i,j} - u_{i+1,j}) - (u_{i-1,j} + u_{i,j})^2\right.$$

$$\left. - \alpha\left|u_{i-1,j} + u_{i,j}\right|(u_{i-1,j} - u_{i,j})\right]$$

$$FUY = \frac{1}{4\delta y}\left[(v_{i,j} + v_{i+1,j})(u_{i,j} + u_{i,j+1}) + \alpha\left|v_{i,j} + v_{i+1,j}\right|(u_{i,j} - u_{i,j+1})\right.$$

$$\left. - (v_{i,j-1} + v_{i+1,j-1})(u_{i,j-1} + u_{i,j}) - \alpha\left|v_{i,j-1} + v_{i+1,j-1}\right|(u_{i,j-1} - u_{i,j})\right]$$

$$FVX = \frac{1}{4\delta y}\left[(u_{i,j} + u_{i,j+1})(v_{i,j} + v_{i+1,j}) + \alpha\left|u_{i,j} + u_{i,j+1}\right|(v_{i,j} - v_{i+1,j})\right.$$

$$\left. - (u_{i-1,j} + u_{i-1,j+1})(v_{i-1,j} + v_{i,j}) - \alpha\left|u_{i-1,j} + u_{i-1,j+1}\right|(v_{i-1,j} - v_{i,j})\right]$$

$$FVY = \frac{1}{4\delta y}\left[(v_{i,j} + v_{i,j+1})^2 + \alpha\left|v_{ij} + v_{i,j+1}\right|(v_{i,j} - v_{i,j+1}) - (v_{i,j-1} + v_{i,j})^2\right.$$

$$\left. - \alpha\left|v_{i,j-1} + v_{i,j}\right|(v_{i,j-1} - v_{i,j})\right]$$

$$VISX = \nu\left[\frac{1}{\delta x^2}(u_{i+1,j} - 2u_{i,j} + u_{i-1,j}) + \frac{1}{\delta y^2}(u_{i,j+1} - 2u_{i,j} + u_{i,j-1})\right]$$

$$VISY = \nu\left[\frac{1}{\delta x^2}(v_{i+1,j} - 2v_{i,j} + v_{i-1,j}) + \frac{1}{\delta y^2}(v_{i,j+1} - 2v_{i,j} + v_{i,j-1})\right]$$

All quantities in the convective and viscous fluxes are evaluated at time $n\delta t$. The coefficient α gives the desired amount of upstream differencing to remove the unconditional instability of the algorithm.

Nevertheless, continuity (Eq. 13) is not satisfied by the velocities computed according to Eq. 14. This incompressibility constraint is imposed by adjusting iteratively the cell pressures until the divergence D of each cell is driven to zero. The iteration proceeds from left to right starting with the bottom row and working upwards. The pressure δp required to make D equal to zero is:

$$\delta p = -D/[2\delta t\,(\frac{1}{\delta x^2} + \frac{1}{\delta y^2})] \tag{15}$$

The velocity components and pressure of each cell are then adjusted to reflect this change:

$$\begin{aligned} p_{i,j} &\rightarrow p_{i,j} + \delta p \\ u_{i,j} &\rightarrow u_{i,j} + \frac{\delta t \delta p}{\delta x} \\ v_{i,j} &\rightarrow v_{i,j} + \frac{\delta t \delta p}{\delta y} \\ v_{i,j-1} &\rightarrow v_{i,j-1} - \frac{\delta t \delta p}{\delta y} \end{aligned} \tag{16}$$

The iteration converges when all cells have D values satisfying the inequality $|D| < \varepsilon$ where ε is of the order 10^{-3} or smaller. If there is a desire to accelerate the convergence, δp can be multiplied by an over-relaxation factor ω [23].

3.2 Boundary Conditions

The boundary conditions are easily imposed by assigning suitable velocities in the fictitious cells surrounding the flowfield. The walls are considered impenetrable, rigid and with no-slip. The rigidity of the wall is simulated by applying an equal to the mainflow and opposite tangential velocity to the boundary cell, so that the transverse velocity on the wall

is zero. The no-slip condition is imposed on the wall by equating the axial velocity to zero, see Fig. 8.

At inlet, a parabolic variation for the u-velocity and zero value for v are assumed. Continuative boundary conditions are prescribed for the outlet plane. Zero velocity gradient is achieved by setting the respective u and v velocities of adjacent cells equal, see Fig. 9.

All boundary conditions, except the ones for the outlet, must be imposed after each pressure iteration. The outflow boundaries are required only after each cycle.

3.3 Numerical Stability

Computed quantities can often exhibit large oscillations in space, time or both. In order to avoid these numerical instabilities, restrictions must be applied in defining the mesh increments δx and δy, the time increment δt, and the upstream differencing coefficient α.

The mesh increments should be small and in accordance with the limitations imposed by the computing time and memory requirements. Once δx and δy are chosen, the time increment must be established in a way that satisfies the inequalities:

$$\delta t < \min \left\{ \frac{\delta x}{|u|} , \frac{\delta y}{|v|} \right\} \tag{17}$$

and

$$\delta t < \frac{1}{2\nu} \frac{\delta x^2 \delta y^2}{\delta x^2 + \delta y^2} \tag{18}$$

The first constraint accounts for the fact that material can not move through more than one cell in one time step, while the second assures that momentum does not diffuse more than one cell in one time step.

The centered equations ($\alpha = 0$) tend to be unstable, so a certain amount of upstream differencing is required for stability. A proper choice for α [23] is:

$$1 \geq \alpha > \max \left\{ \left| \frac{u\delta t}{\delta x} \right| , \left| \frac{v\delta t}{\delta y} \right| \right\} \tag{19}$$

Finally, the over-relaxation factor should not exceed 2.0, because an infinite number of pressure iterations will be required to obtain the solution. A value of $\omega = 1.8$, which proved to be the optimum in the present calculations is used. Other important computational parameters are given in Table 3.

CHAPTER FOUR

RESULTS

4.1 Steady Flow

Computations with the aim to obtain the flow characteristics in the abdominal aorta are made for models I and II. At inlet, the vertical component of the velocity is neglected, while the horizontal one is assumed to have a general profile given by:

$$u_{IN} = \frac{2}{(e^2 - e + 0.167)} \{(2e - 1)\, y^3 - (3e^2 - 1)\, y^2 + (3e^2 - 2e)\, y\} \qquad (20)$$

where e is the eccentricity of the maximum velocity from the center line of the main artery. The local wall friction coefficient is calculated according to:

$$C_f = \frac{2}{Re} \left.\frac{dq}{d\eta}\right|_{\eta=0} \qquad (21)$$

where q is the non-dimensional velocity parallel to the wall and η is the distance in the inwards normal to the wall.

A velocity field plot for model I is shown in Fig. 10. The inlet velocity profile is considered to be symmetric (e = h/2) and the Reynold's number is varied from 100 (rest conditions) to 2000 (exercise conditions). Reverse flow regions are not found at any Reynold's number.

Bifurcations with a daughter-to-parent branch area ratio (A_R) less than one contain flow which accelerates, converting pressure energy into kinetic energy and resulting in a negative pressure gradient in the direction of flow. These factors, which quicken flow and reduce pressure have been associated with boundary layer stability and laminar flow [41]. As a result, reverse flow regions are most probable to occur at $A_R > 1$. During steady flow visualization of the abdominal aorta, performed in our laboratory, secondary effects due to

horseshoe vortex at low Reynolds are also present. These eddy type flow regions disappear as Re increase. However, the simplified two-dimensional computational model is not capable of predicting these secondary flows.

The parabolic profile of the horizontal velocity is maintained from the entrance up to the junction. In the daughter branches, the velocity profile is skewed towards the inner wall. Due to the sudden change in direction, a centrifugal force drives the fluid away from the center of curvature, i.e. to the third wall. This effect disappears and the flow resumes to a parabolic profile as ξ increases.

Although geometrical and similitude parameters are different, the results obtained can be qualitatively correlated to those acquired by other researchers. After experimental measurements, El Masry et al [24], Walburn and Stein [25], Batten and Nerem [26], Siouffi et al [27], Feuerstein et al [28] and Frederick et al [29] found that there is no flow reversal during steady flow conditions and that the maximum velocity parallel to the wall, just after the flow divider, is shifted towards the inner wall. In the last three papers there is a double peak observed in the velocity profile downstream in the iliac branches which is not evident in the present study, see Fig. 11. Theoretical computations performed by Fernandez et al [30], and Kandapra et al [31], show a separation region on the outer wall just after the corner. Finally, Lynn et al [32] found no reverse flow and skewing of the velocity profile towards the outer wall. This effect might be due to the imposed parabolic velocity profile at the exit.

One of the many parameters considered responsible for the initiation and development of atherosclerosis is the wall shear stress behaviour. Figure 12 shows C_f as a function of ξ in the second wall of model I. It can be seen that C_f is almost constant upstream point B. At approximately $x = 0.8\,\bar{h}_1$, C_f increases to a maximum in the area of the bend C. After this point, C_f drops drastically to a minimum slightly downstream ($x = 0.18\,\bar{h}_1$) and

gradually increases, most likely to a constant value, further down. Since there is no asymmetry introduced to the inlet velocity profile, the first wall experiences exactly the same distribution of C_f along ξ as the second wall. On the third wall, the local friction coefficient exhibits a Gaussian distribution, see Fig. 13, with a maximum value attained at the tip of the divider (point A).

As Re increases, qualitatively similar profiles of C_f to those shown on Fig. 12 and 13 are obtained. The maximum and minimum C_f values as well as their difference decrease with increasing Re for both the first, see Fig. 14, and the third, see Fig. 15, walls. For low Reynold's numbers the maximum C_f on the flowfield is located at the tip of the flow divider with a value approximately 80% larger than that of the maximum C_f at the corner of the outer wall. Increasing Re, lessens the difference between maximum C_f's at points A and C. At a certain range ($1100 < Re < 1600$) the C_f of the first wall is the highest, see Fig. 16. The abrupt escalation of C_f, from a constant value upstream to a maximum value just before the bend, increases along with Re, see Fig. 17. Also, as Re rises so does the distance from which the elevation of C_f begins, see Fig. 18, contemplating that as Re increases, the wall just before C is subjected to higher elevations of C_f and is affected to a greater extent.

The bifurcation angle ϕ is altered for a constant Reynolds number (Re = 700). Figure 19 shows the maximum values of C_f at the tips of the bend and the flow divider. It is interesting to note that for $\phi \simeq 60°$ both C_{fmax}'s are almost equal. The increase of the angle ϕ generally increases the C_f elevation on the first wall, see Fig. 20. The area affected by C_f's escalation reaches a peak at $\phi \simeq 50$ and narrows as ϕ increases, see Fig. 21.

Similar C_f behaviour as the one shown in Fig. 12 can be found in the computational work of Friedman and Ehrlich [33], and in the experimental research by Mark et al [34], see Fig. 22.

A non-symmetric inlet velocity profile (e = 0.375 h_1), produces different C_f distributions. Even though the C_f oscillation is present on both first and second walls, see Fig. 23 and 24, the values of C_f are no longer symmetric. Upstream, on the first wall, C_f increases with ξ while it decreases on the second wall. An interesting behaviour of C_f appears with the introduced asymmetry on the third wall, see Fig. 25. A combination of high-low shear appears around the flow divider with the highest shear on the side where the asymmetry is introduced and where the flowrate is larger. A similar effect is obtained when $Q_5 \neq Q_4$ is introduced to simulate increased resistance in one of the iliacs.

A number of investigators, such as Caro et al [13], Mitchell and Schwartz [38], Texon [39] and Mustard et al [40], reported relative sparing of the flow divider from atheroma and heavy involvement of the disease on the outer wall of the junction. Sharp et al [8] notes, after experiments on aortic models similar to those in our study, that with acute bifurcation angles there are higher rates of shear on the inner walls of the iliac arteries, and lower rates of shear on the outer walls. As the bifurcation angle increases, the difference between rates of shear stress diminishes.

It is apparent from the results of steady flow conditions obtained, that low Reynold's numbers and small bifurcation angles result in severe oscillations of C_f value around corner C. These sudden changes in shear stress might interfere with the normal interactions of the endothelial cells, damaging the area of the bend. The injury will upset the symmetric nature of the flow, causing C_f oscillations at point A and thus eventually harming the tip of the flow divider. With age, endothelial cells are expected to have a delayed reaction to abrupt shear stress fluctuations, thus inducing the above mentioned irregularities.

For the aorta with the renal arteries, model II, the velocity field plot is given in Fig. 26. It shows the same characteristics as model I downstream from the renals. A small area of flow reversal is observed just after the downstream corner of the junction. The same

high-low behaviour of C_f is also present, see Fig. 27, with negative shear after the right corner of the bifurcation. In addition, Fig. 28, illustrates a second oscillatory behaviour of C_f taking place in the neighbourhood of the renal artery. Similar distributions of wall shear can be found in the theoretical work of O'Brien and Ehrlich [35].

Table 4 gives the percentage error between the theoretically calculated average exit velocity and the one computed numerically. The average error is found to be 0.18% or 1.8 ml/lit.

4.2 Pulsatile Flow

The pulsatile nature of the aortic flow is simulated by a sinusoidal periodic function. The introduction of time-dependent flow adds complexity to the computations. The input flow rate varies according to Fig. 29 and is distributed conforming to Eq. (20). Different amplitudes (A) and periods of oscillation (T), as well as the corresponding Womersley (α) parameter are given in Table 5. Due to previously mentioned assumptions, such as incompressibility of the fluid and rigidity of the wall, it is safe to consider that the pulse wave will propagate at infinite velocity from the entrance to the exit and thus no phase lag between the inlet and outlet pulses will be present. Steady periodic conditions are achieved after five periods.

A plot of the velocity profile is shown in Fig. 30. The shape of the velocity is skewed towards the inner wall, as was the case for steady flow conditions. However, when compared with the steady flow case, the location of maximum velocity for pulsatile flow is slightly shifted toward the center of the channel. Variation of amplitude and period of oscillation produces no apparent effect on the skewing of the velocity profile. Similar profiles are found in the experimental results of Walburn and Stein [25], Siouffi et al [27], Batten and Nerem [26] and the numerical solutions of Fernandez et al [30] and Einav and Stolero [36].

The distribution of the wall friction coefficient is similar to that for steady flow conditions. Figures 31 and 32 show the alteration of C_{fmax} on the outer and inner walls respectively, as the amplitude of oscillation increases. The amplitude plays an important role in the variation of maximum C_f only at the time of minimum flow input. No influence is noticed on the minimum C_f just after point C, when amplitude changes.

As the fluid accelerates, C_f increases at the corners of the bend and decreases at the apex of the flow divider. When the fluid decelerates, C_f increases at the tip of the third wall while it decreases just before point C, see Fig. 33. The C_f fluctuations are higher as the amplitude of oscillation increases. During one period, the tip of the inner wall is exposed to the highest wall shear friction coefficient. As amplitude increases, the difference between C_{fmax}'s at inner and outer walls increases dramatically at minimum flow, where the third wall experiences fourteen times higher shear stress than the corner of the outer wall. At maximum flow both walls have equal C_{fmax}, see Fig. 34.

Reverse flow regions are not present at accelerating flows and for small amplitudes of oscillation ($A < 0.2$). However, transient flow reversals appear at small ratios of mean velocity to amplitude of oscillation, on the outer wall. Further decrease of the ratio prolongs the presence of flow separation. The third wall is not influenced by velocity reversals.

Secondary effects may be the main cause for the absence of the flow separation during maximum flow conditions on the outer wall. Brech and Bellhouse [42] reported that at accelerating flows, streamlines from the top and bottom of the pipe cross over to fill the region on the outer wall of the trunk. A forward moving deflected streamline would result in positive velocities in areas where otherwise reverse flow might be expected. These secondary effects vanish during the decelerating stage of the cycle. Experimental results from Walburn and Stein [25], Batten and Nerem [26], Mark et al [34] and the

numerical solution by Fernandez [30], suggest the existence of negative velocities at the vicinity of point C for low Re. For such Reynolds numbers which imply large amplitudes of oscillation, similar effects can be predicted from the present study. In reference [26] the recirculation zone is extended upstream corner C, complying with the results mentioned above. Ku et al [43] report that reverse flow regions occur rapidly with decelerating flows in the carotid bifurcation, while they do not appear during accelerating flows. After a detailed comparison of hemodynamic measurements with quantitative morphologic studies of the distribution of atherosclerosis they concluded that, low mean shear stress and oscillations in the direction of wall shear stress may be critical factors in the atherogenetic process.

Frequency variation does not produce a significant effect on the magnitude of the wall friction coefficient. There is only a small growth in the reverse flow region area along the first and second walls.

4.3 Physiological Flow

Velocities and the local wall friction coefficient are computed for physiological inlet flow conditions. The aortic blood flow is assumed to vary according to Fig. 35. Discretization of the time steps give the corresponding input flow rates, the maximum being 5.68 *l*it/min during systole and the minimum 0.89 *l*it/min during diastole. Difficulties to measure velocities in the human abdominal aorta leave us only with flow rate information of the ascending aortic input and restricts us to the assumption that there is constant wave propagation and no blood bleed as the fluid travels towards the abdominal aorta. Velocity measurements performed by Rieu et al [37] on the arterial tree confirm our input as that of the ascending aorta. The abdominal aortic input is qualitatively similar to that of Fig. 35, but with a reduced maximum flow rate to 2.6 *l*it/min.

Velocity plots are obtained for models I and III. Six cycles are required before steady periodic conditions can be reached. The period is characterized according to the presence of reverse flow regions, by four distinct sections. On the early systolic acceleration a large recirculation zone is present on the outer walls of the bifurcation, mainly due to the deceleration of the flow at the end of the previous period. As the flow continues to accelerate the reverse flow region contracts to a small area upstream the bend on the first and second walls, and disappears at approximately t = c, see Fig. 36 and Fig. 37. During the remaining systolic acceleration and the beginning of the deceleration no fluid reversal is found, see Fig. 37. At t = e the fluid starts slowly to invert at the outer wall, near the entrance. As the deceleration persists, the separation zone thickens and extends into the positive axis of walls 1 and 2, see Fig. 38. As the diastole starts, a new region of flow reversal appears downstream the flow divider at the third wall. At the same time, the inverse flow region at the outer walls propagates past the exit As diastole advances, so does the reverse flow region at wall 3 towards the flow divider tip, see Fig. 39 and Fig. 40.

The velocity profile in the daughter tube is skewed towards the inner wall just downstream from the apex. However, at the exit and at t = a, the maximum velocity moves towards the outer wall. As time progresses, the exit profile exhibits two points of inflection close to the walls, see Fig. 41. When flowrate maximizes, the exit velocity profile becomes parabolic and remains such until the late stages of systole, see Fig. 42. At t = f and prior to the diastole, the exit profile is skewed towards the outer wall and during diastole it attains the so called, "m" distribution, see Fig. 42. Finally the velocity profile upstream the junction maintains its parabolic distribution during the early stages of systolic acceleration and at the late stages of systolic deceleration. At Re > 1600 the profile is flat, while during diastole, it exhibits the "m" distribution. It seems that for physiological type flow, the centrifugal forces exerted on the turning fluid are weaker than for steady flow.

Qualitatively similar experimental results are reported by Siouffi et al [27], at peak systolic and diastolic conditions. Rieu et al [37] show similar velocity plots for the entire period with comparable flow reversal regions and skewing of the velocity.

The wall friction coefficient is calculated according to Eq 21 along the ξ-axis. At the onset of the systole until Re = 785 the first and second walls experience small, steady, negative shear stress values along the negative ξ-axis. Just before the bend, C_f increases continuously until Re = 338, while it drops suddenly and then rises gradually at Re= 785. At the third wall, C_f drops to a minimum at approximately $x = 0.8\,\bar{h}_1$ and escalates as ξ increases, see Fig. 43 and Fig. 44. As Re increases, C_f becomes positive at all locations, increasing rapidly at the entrance. No oscillations occur in space up until the bend, where the familiar high-low pattern appears. At wall no. 3, the Gaussian distribution previously obtained for steady and pulsatile flow conditions reemerges, see Fig. 45. Where the systolic deceleration originates, walls no. 1 and no. 2 experience a sudden decrease in C_f at inlet, followed by a gradual increase. The area of steady C_f along the wall diminishes and no space oscillations are apparent at the corners of the bend, see Fig. 46. For Re less than 1000, as well as during diastole, C_f becomes negative along the outer walls. The shear augments prior to reaching point C and continues to increase downstream the daughter tube, see Fig. 47. Figure 48 shows the difference between the local wall friction coefficients of the apex and the corner of the bend as a percentage of C_f at point A. At prior and post-peak systolic conditions, the outer corner experiences the highest shear stress while during diastole and both early and late systole, the greatest amount of shear stress is endured by the flow divider. The position of maximum and minimum C_f at the outer walls during one period is shown in Fig. 49. Maximum C_f takes place at the exit, at the time of diastole and decelerating systole (Re < 1015). During the remaining systole, C_f maximizes just before corner C. C_f is minimum at the inlet during peak systole and progresses downstream never exceeding x= -2.4. Lastly, in Fig. 50, the C_f difference

between points D and C is given as a percentage of C_f at C, for one time period. Once again, shear at the corner dominates during systole while the shear at point D is highest for diastole and late systole.

The area of the outer wall upstream the bifurcation is subjected to low shear during diastole and accelerating systole. At the time of decelerating systole, C_f increases sharply as it travels towards the corner. At the vicinity of point C, the high-low C_f fluctuation appears when $c < t < f$. During the remaining period, C_f does not oscillate in space but rather experiences an increase just before and after the corner. Downstream the daughter branch, C_f increases to a maximum value for $t > f$ and $t < a$, and eventually becomes constant for $c < t < f$.

In conclusion, unsteady flows are characterized by periods of space and time oscillations of C_f. Space oscillations are defined as variations of skin friction coefficient along the wall at a fixed time level, while time oscillations designate variations of Cf at a fixed location on the wall durimg different time levels. The outer corners of the junction are subjected to space oscillations during accelerating flows while large oscillations in time are present during decelerating flows.

In order to examine the effect of the bifurcation of the flow characteristics of the abdominal aorta, a straight pipe model is used. Model III produces results with similar velocity profiles as those obtained in model I. As expected, after the flow adjusts to the inlet changes, it maintains a constant velocity profile and wall shear stress coefficient, see Fig. 51. The minimum C_f along the first and second walls of model III remains the same as that in model I during one period of oscillation. However, the maximum C_f of the bifurcation is greater throughout the period than that of the straight channel, see Fig. 52. At the accelerating phase of systole, the difference in C_{fmax} between the two models, drops to a minimum where Re peaks and gradually increases to a maximum at decelerating

systolic conditions (t = e). As flow rate continues to drop, so does the C_{fmax} difference which becomes zero at the decelerating phase of diastole.

In conclusion, the bifurcation proves to increase the wall shear stress. However, the actual shape of the flow-type input function appears to be the factor responsible for initiating reverse flow regions in the model and bifurcation serves to amplify them.

CHAPTER FIVE

CONCLUSION

Numerical solutions of steady, unsteady harmonic and physiological flows in simplified abdominal aortic models were presented. Many assumptions were made in order to obtain an explanation on the influence of hemodynamic factors on atherogenesis. Blood was considered Newtonian, incompressible and homogeneous, the flow was supposed to be two-dimensional and laminar, while the aortic wall was assumed to be rigid and with constant diameter. Also during unsteady flow conditions, the inlet and outlet pulses were assumed to have no phase lag.

During steady flow conditions, sites most prone to atherosclerosis, such as the outer corners of the bifurcation, were found to be subjected to large space oscillations of shear stress. Small Reynolds numbers and angles of bifurcation, increased the magnitudes of the shear oscillation. Regions of reverse flow were not present. Strong centrifugal forces caused skewing of the velocity towards the outer wall of the bifurcation. The flow asymmetry, introduced at the inlet, in order to simulate increased resistance in one of the iliac arteries, produced fluctuations in wall shear stress at the leading edge of the flow divider. Models simulating both the iliac and renal arteries showed a space oscillation of the wall friction coefficient just before and after the renal arteries along with a small recirculation zone downstream the renals.

Pulsatile flow conditions produced reverse flow regions on the outer walls during decelerating flow and large amplitudes of oscillation. The shear stress distribution along the walls was similar to that of steady flow. Frequency variation did not produce a significant effect on the flow characteristics.

Physiological flow conditions complicated not only the computations but the response of the wall shear to inlet flow acceleration and deceleration as well. In addition to space oscillatory behaviour, the wall shear stress near the outer corners of the bifurcation exhibited time varying oscillations. Time dependent reverse flow regions appeared on both the inner and outer walls. The effects of the centrifugal force on the skewing of the velocity profile at the entrance of the doughter tubes proved to be weaker than in the case of steady flow conditions. Finally, the straight pipe model demonstrated the great influence of the input function on the development of the reverse flow regions and produced lower shear stress values than the bifurcation model.

Based on arteriograms, the progressive history of atherogenesis has shown to initiate on the outer wall and progresses to the inner wall. The results of the study give us confidence to believe that it is not the low or high shear stress that is responsible for the formation of atherosclerotic lesions but rather the drastic fluctuation of the shear stress that may trigger an abnormal response in the endothelial cells.

Future work in biochemistry should focus on studies which will assess the influence of shear stress as well as shear stress variations in time and space on the functional behaviour of endothelial cells. From the engineering point of view, the response of hemodynamic properties to alterations in the input normal cardiac wave so as to simulate hypertension and high blood pressure must be examined. Furthermore, a realistic three-dimensional model is required for more meaningful answers to be obtained with respect to the etiology of atherogenesis.

REFERENCES

1. Skalak, R., Keller, S.R. and Secomb, T.W., "Mechanics of Blood Flow", Trans. ASME/Journal of Biomechanical Engineering, Vol. 103, May 1981, pp. 102-115.

2. Pedley, T.J., "The Fluid Mechanics of Large Blood Vessels, Cambridge University Press, London, England, 1980.

3. Caro, C.G., Pedley, T.J., Schroter, R.C. and Seed, W.A., "The Mechanics of the Circulation", Oxford University Press, London, England, 1978.

4. Pedley, T.J., "Physiological Fluid Mechanics", International Union of Theoretical and Applied Mechanics, 1980, pp. 151-161.

5. Patel, D.J. and Vaishnav, R.N., "Basic Hemodynamics and its Role in Disease Processes", University Park Press, Baltimore, 1980.

6. Kinlough-Rothbone, R.L. and Mustard, J.F., "Atherosclerosis, Current Concepts", The American Journal of Surgery, Vol. 141, Jun. 1981, pp. 638-642.

7. Glagov, S., Zarins, C., Giddens, D.P. and Ku, D.N, "Hemodynamics and Atherosclerosis", Arch. Pathol. Lab. Med., Vol. 112, October 1988, pp. 1018-1031.

8. Nerem, R.M. and Cornhill, J.F., "The Role of Fluid Mechanics in Atherogenesis", Trans. ASME/Journal of Biomechanical Engineering, Vol. 102, Aug. 1980, pp. 181-189.

9. Sharp, W.V., Donovan, D.L., Teague, P.C. and Mosteller, R.D., "Arterial Occlusive Disease: A Function of Vessel Bifurcation Angle", Surgery, Vol. 91, Number 6, 1982, pp. 680-685.

10. Gessner, F.B., "Hemodynamic Theories of Atherogenesis", Circulation Research, Vol. 33, Number 3, Sep. 1973, pp. 259-266.

11. Friedman, M.H., O'Brien, V. and Ehrlich, L.W., "Calculation of Pulsatile Flow through a Branch. Implication for the Hemodynamics of Atherogenesis", Circulation Research, Vol. 36, Feb. 1975, pp. 277-285.

12. Fry, D.L., "Acute Vascular Endothelial Changes Associated with increased Blood Velocity Gradients", Circulation Research, Vol. 22, Feb. 1968, pp. 164-197.

13. Caro, C.G., Fitz-Gerald, J.M. and Schroter, R.C., "Atheroma and Arterial Wall Shear. Observation Correlation and Proposal of a Shear Dependent Mass Transfer Mechanism for Atherogenesis", Proc. Roy. Soc. Lond. B., Vol. 177, 1971, pp. 109-159.

14. Fox, J.A. and Hugh, A.E., "Localization of Atheroma: A Theory Based on Boundary Layer Separation", British Heart Journal, Vol. 28, 1966, pp. 388-399.

15. Zamir, M. and Roach, M.R., "Blood Flow Downstream of a Two-Dimensional Bifurcation", Journal of Theoretical Biology, Vol. 42, 1973, pp. 33-48.

16. McDonald, D.A., "Blood Flow in Arteries", Edward Arnold Ltd., London, England, 1960.

17. Bergel, D.H., "Cardiovascular Fluid Dynamics", Volume 2, Academic Press, London, England, 1972.

18. Ku, D.N., Glagov, S., Moore, J.E. and Zarins, C.K., "Flow Patterns in the Abdominal Aorta under Simulated Postprandial and Exercise Conditions: An Experimental Study", Journal of Vascular Surgery, Vol. 9, Number 2, Feb. 1989, pp. 309-316.

19. Yuan, S.W., "Foundations of Fluid Mechanics", Prentice-Hall Inc., Englewood Cliffs, N.J., 1967.

20. Streeter, V.L. and Wylie, E.B.,"Fluid Mechanics", McGraw Hill-Ryerson Lim., Toronto, 1981.

21. Anderson, D.A., Tannehill, J.C. and Pletcher, R.H., "Computational Fluid Mechanics and Heat Transfer", Hemisphere Publishing Corporation, Philadelphia, 1984.

22. Stavrianos, K., Vatistas, G.H. and Graham, A.M., "Numerical Solution of the Flow in the Abdominal Aorta", Proceedings of ASME International Computers in Engineering Conference, Anaheim, California, 1989.

23. Hirt, C.W., Nichols, B.D. and Romero, N.C., "SOLA: A Numerical Solution Algorithm for Transient Fluid Flows", Report LA-5882, Los Alamos Scientific Laboratory and the University of California, Los Alamos, N.M., 1975.

24. El-Masry, O.A., Feuerstein, I.A. and Round, G.F., "Experimental Evaluation of Streamline Patterns and Separate Flows in a Series of Branching Vessels with Implications for Atherosclerosis and Thrombosis", Circulation Research, Vol. 43, Number 4, Oct. 1978, pp. 608-618.

25. Walburn, F.J. and Stein, P.D., "Flow in a Symmetrically Branched Tube Simulating the Aortic Bifurcation: The Effects of Unevenly Distributed Flow", Annals of Biomedical Engineering, Vol. 8, 1980, pp. 159-173.

26. Batten, J.R. and Nerem, R.M., "Model Study of Flow in Curved and Planar Arterial Bifurcations", Cardiovascular Research, Vol. 16, 1982, pp. 178-186.

27. Siouffi, M., Pelissier, R, Farahifar and D., Rieu, R., "The Effect of Unsteadiness on the Flow through Stenoses and Bifurcations", Journal of Biomechanics, Vol. 17, Number 5, 1984, pp. 299-315.

28. Feuerstein, I.A., El Masry, O.A. and Round, G.F., "Arterial Bifurcation Flows - Effects of Flow Rate and Area Ratio", Canadian Journal of Physiology and Pharmacology, Vol. 54, Number 6, Dec. 1976, pp. 795-807.

29. Walburn, F.J. and Stein, P.D., "Velocity Profiles in Symmetrically Branched Tubes Simulating the Aortic Bifurcation", Journal of Biomechanics, Vol. 14, Number 9, 1981, pp. 601-611.

30. Fernandez, R.C., De Witt, K.J. and Botwin, M.R., "Pulsatile Flow Through a Bifurcation with Applications to Arterial Disease", Journal of Biomechanics, Vol. 9, 1975, pp. 575-580.

31. Kandapra, K. and Davids, N., "Analysis of the Fluid Dynamic Effects on Atherogenesis at Branching Sites", Journal of Biomechanics, Vol. 9, 1976, pp. 735-741.

32. Lynn, N.S., Fox, V.G. and Ross, L.W., "Computation of Fluid-Dynamical Contributions to Atherosclerosis at Arterial Bifurcations", Biorhelogy, Vol. 9, 1972, pp. 61-66.

33. Friedman, M.H. and Ehrlich, L.W., "Effect of Spatial Variations in Shear on Diffusion at the Wall of an Arterial Branch", Circulation Research, Vol. 37, Oct. 1975, pp. 446-454.

34. Mark, F.F., Bargeron, C.B., Deters, O.J. and Friedman, M.H., "Experimental Investigations of Steady and Pulsatile Laminal Flow in a 90° Branch", Trans. ASME/Journal of Applied Mechanics, Sep. 1977, pp. 372-377.

35. O'Brien, V. and Ehrlich, L.W., "Simulation of Unsteady Flow at Renal Branches", Journal of Biomechanics, Vol. 10, 1977, pp. 623-631.

36. Einav, S. and Stolero, D., "Pulsatile Blood Flow in an Arterial Bifurcation: Numerical Solution", Medical and Biological Engineering and Computing, Vol. 25, Jan. 1987, pp. 12-17.

37. Rieu, R., Friggi, A., Pelissier, R., "Velocity Distribution Along an Elastic Model of Human Arterial Tree", Journal of Biomechanics, Vol. 18, Number 9, 1985, pp. 703-715.

38. Mitchell, J.R.A. and Schwartz, C.J., "Arterial Disease", Oxford Press, London, England, 1965.

39. Texon, M., "The Role of Vascular Dynamics in the Development of Atherosclerosis", Academic Press, London, England, 1963.

40. Mustard, J.F., Roswell, H.C., Murphy, E.A. and Downie, H.G., "In Evolution of the Atherosclerotic Plaque", University of Chicago Press, Chicago, Il., 1963.

41. Schlichting, H., "Boundary Layer Theory", Sixth Edition, McGraw-Hill Book Co., New York, N.Y., 1968.

42. Brech, R. and Bellhouse, B.J., "Flow in Branching Vessels", Cardiovascular Research, Vol. 7, 1973, pp. 593-600.

43. Ku, D.N., Giddens, D.P., Zarins, C.K. and Glagov, S., "Pulsatile Flow and Atherosclerosis in the Human Carotid Bifurcation", Arteriosclerosis, Vol. 5, May-June 1985, pp. 293-302.

Table 1. Dimensions of simplified aorta

ϕ	A_R	$\bar{h}_1$	$\bar{h}_2 = \bar{h}_3$	$\bar{h}_4 = \bar{h}_5$	$\bar{l}_1$	$\bar{l}_2$	$\bar{l}_3$	Δx	Δy
30°	0.564	1	0.531	0.187	3.452	1.352	0.933	0.187	0.05
40°	0.535	1	0.517	0.137	3.503	1.316	0.687	0.137	0.05
48°	0.601	1	0.548	0.112	3.425	1.353	0.562	0.112	0.05
50°	0.592	1	0.544	0.107	3.485	1.301	0.536	0.107	0.05
60°	0.541	1	0.520	0.087	3.421	1.300	0.433	0.087	0.05

Table 2. Typical experimental measurements of diameters and division of flow in the abdominal aorta

a) Average values based on 16 models of various ages [13]				
$\bar{h}_1 = 1$	$\bar{h}_2 = 0.594$		$\bar{h}_3 = 0.626$	
b) Average values based on 55 models of various ages [18]				
Abdominal Aorta	Left Iliac	Right Iliac	Left Renal	Right Renal
$\bar{h}_1 = 1$	$\bar{h}_2 = 0.743$	$\bar{h}_3 = 0.743$	$\bar{h}_4 = 0.343$	$\bar{h}_5 = 0.343$
Angle with horizontal	25°	25°	65°	60°
Flow division at Rest in [ml/min]	390 [15%]	390 [15%]	390[15%]	390 [15%]
Post prandial	370 [13%]	370 [13%]	370 [13%]	370 [13%]
Exercise	2270[40%]	2270 [40%]	290 [5%]	290 [5%]

Table 3. Computational models and parameters

Model*	Flow Conditions			Inlet Conditions		ϕ					Re	T(sec)	Q_2	Q_4
	Steady	Pulsatile	Physiol.	Sym.	Non-sym.	30	40	48	50	60				
I	x				x			x			400		$.50Q_1$	
	x			x		x					700			
	x			x			x				700			
	x			x					x		700			
	x			x						x	700			
	x			x				x			100-2000			
		x		x				x			280-520	0.6		
		x		x				x			280-520	0.8		
		x		x				x			280-520	1.0		
			x	x				x			0-2300	0.8		
II	x			x		x					700		$.45Q_1$	$.05Q_1$
	x			x			x				700			
	x			x					x		700			
	x			x						x	700			
	x			x				x			100-2000			
III		x		x				x			280-520	0.8	$.50Q_1$	
			x	x				x			0-2300	0.8		

*Model I corresponds to the abdominal aorta without renal arteries, model II includes the renals and model III is a straight pipe. For all models $\epsilon = 10^{-4}$ and $\nu = 3.5 \times 10^{-6}$ m^2/s

Table 4: Error between theoretical and numerical exit velocities

Re	Model I	Model II	$\bar{v}_{THEO}$(m/s)	$\bar{v}_{NUM}$(m/s)	% error
400	X		0.0851	0.0849	0.24
600	X		0.1277	0.1273	0.31
700	X		0.1487	0.1485	0.14
800	X		0.1701	0.1698	0.18
900	X		0.1914	0.1910	0.21
1000	X		0.2126	0.2121	0.24
400		X	0.0765	0.0764	0.13
600		X	0.1150	0.1148	0.17
700		X	0.1339	0.1338	0.08

Table 5: Computational parameters for pulsatile flow

$Q_{1\,MEAN}$ (lit/min)	T (sec)	A (%Q_{1MEAN})	Re	α
0.988	1.0	10	360-440	10.05
		20	320-480	
		30	280-520	
	0.8	10	360-440	11.24
		20	320-480	
		30	280-520	
	0.6	10	360-440	12.97
		20	320-480	
		30	280-520	

Table 6. Input parameters for physiological conditions

POINT	CYCLE	Q_1 (lit/min)	t	Re	α
a	5	0.84	0.221	338	11.24
b	10	1.94	0.239	785	
c	20	5.04	0.275	2039	
d	30	5.68	0.311	2296	
e	60	3.69	0.419	1492	
f	70	2.51	0.455	1015	
g	80	1.15	0.491	466	
h	85	0.00	0.509	0	
i	90	-0.57	0.527	-232	
j	95	0.21	0.545	86	
k	100	0.00	0.564	0	

Fig. 1. Illustration of the great vessels at the root of the neck by Leonardo da Vinci [1]

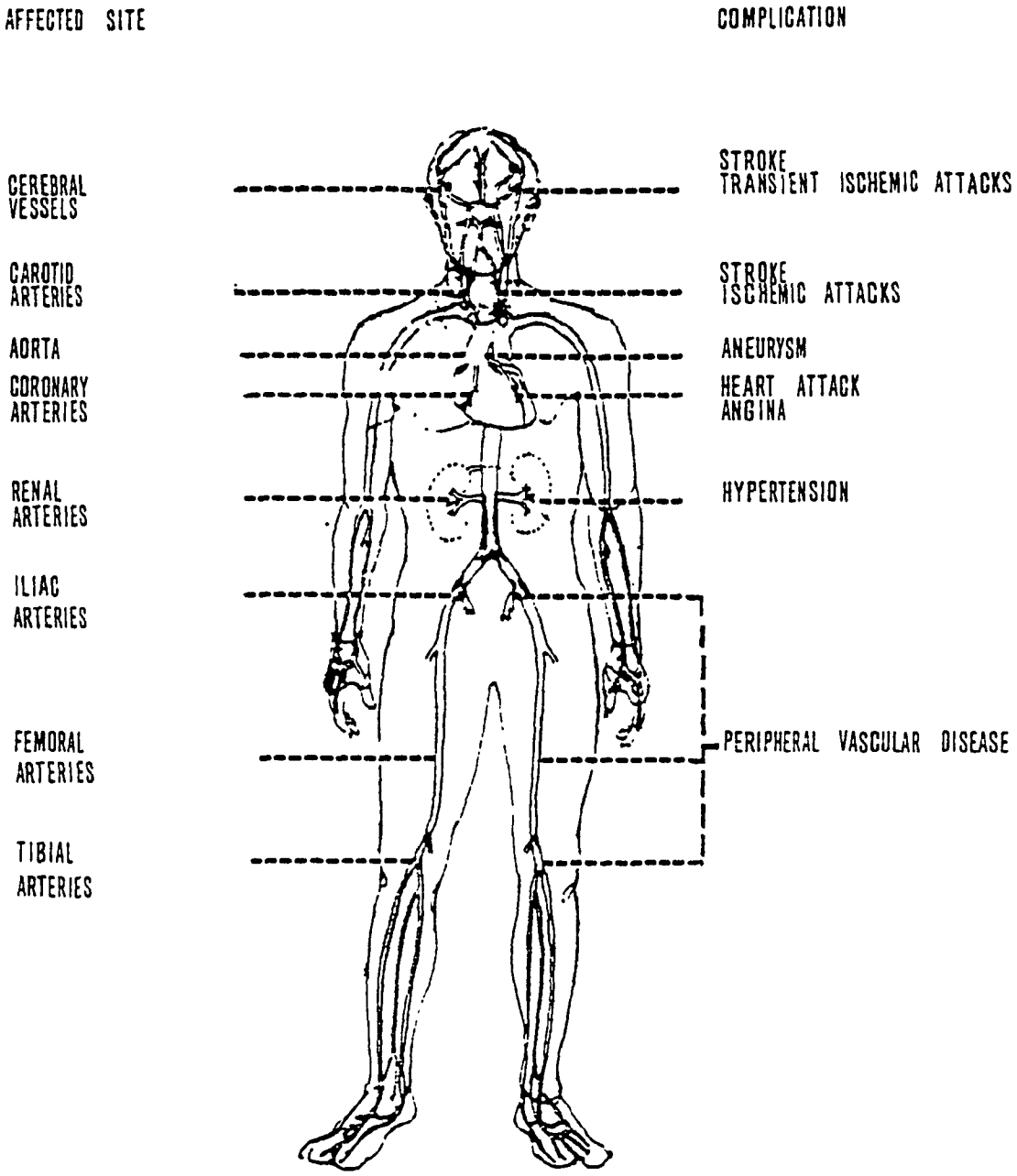

Fig. 2. Schematic representation of the discrete character of atherosclerotic lesions and the major complications associated with them in the aorta and its branches [5] (From the United States Department of Health, Education and Welfare, 1977)

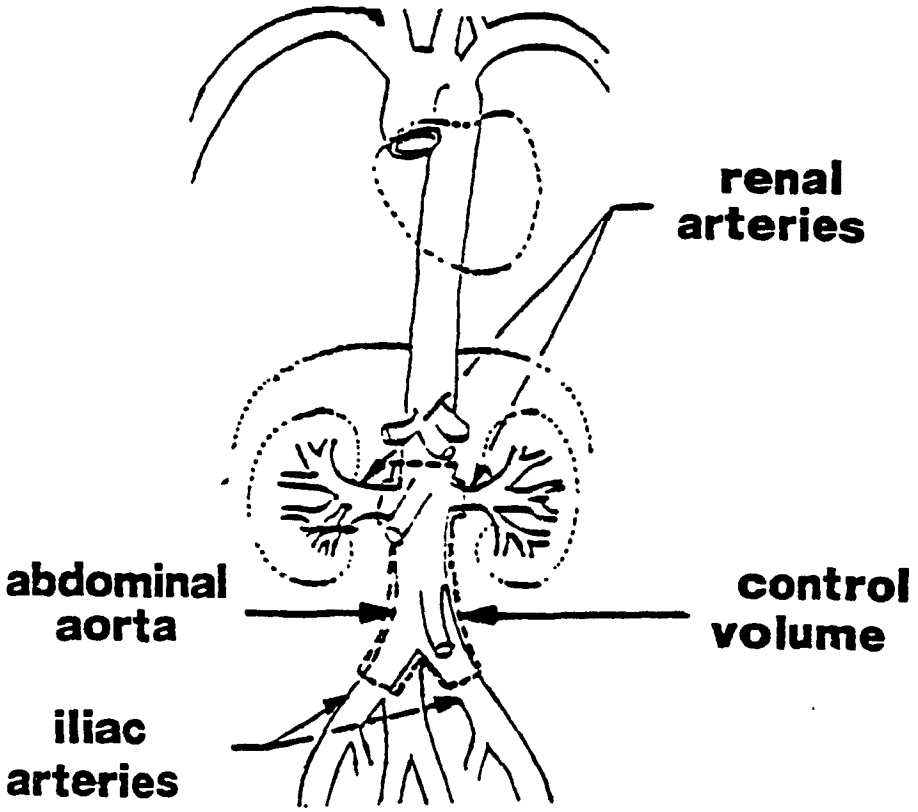

Fig. 3. Main arterial tree

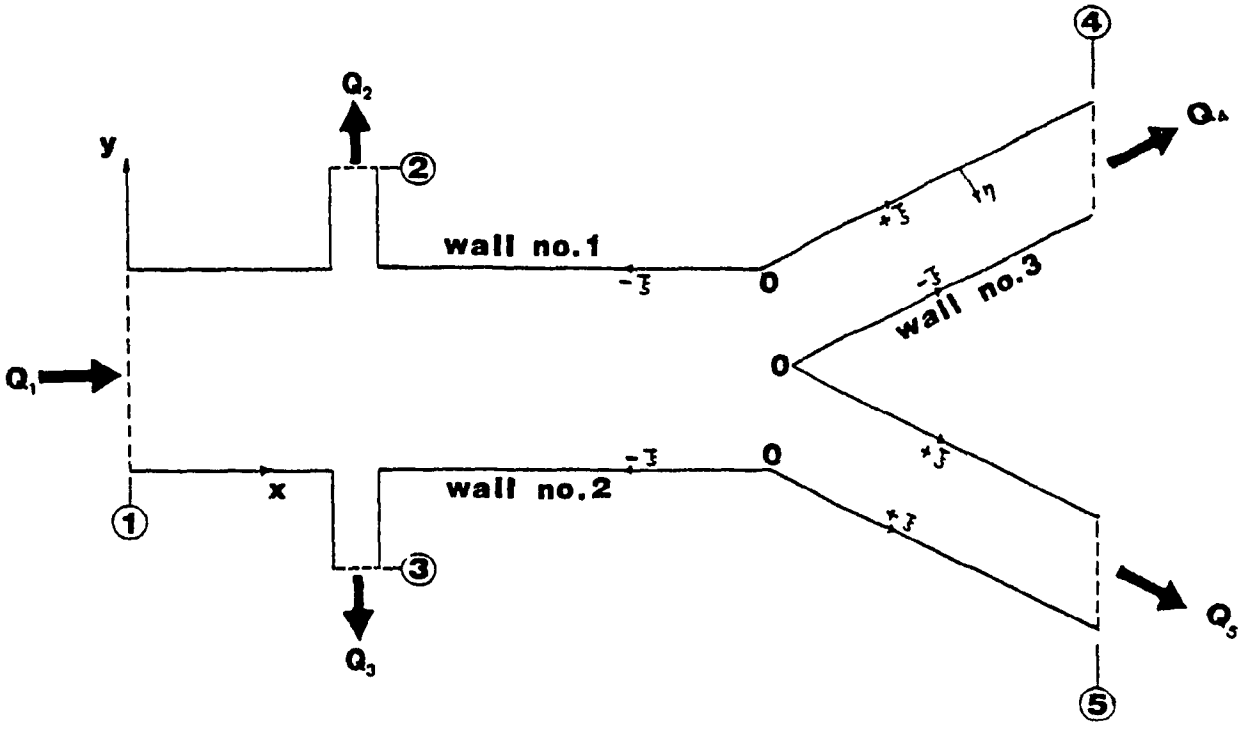

Fig. 4. Schematic of a simplified aorta

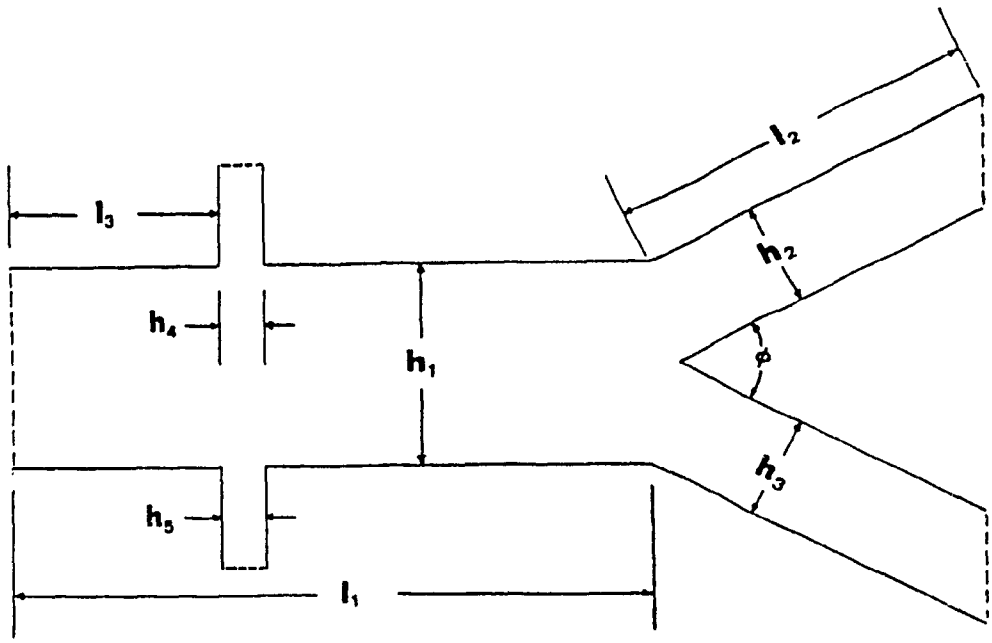

Fig. 5. Schematic of geometric parameters

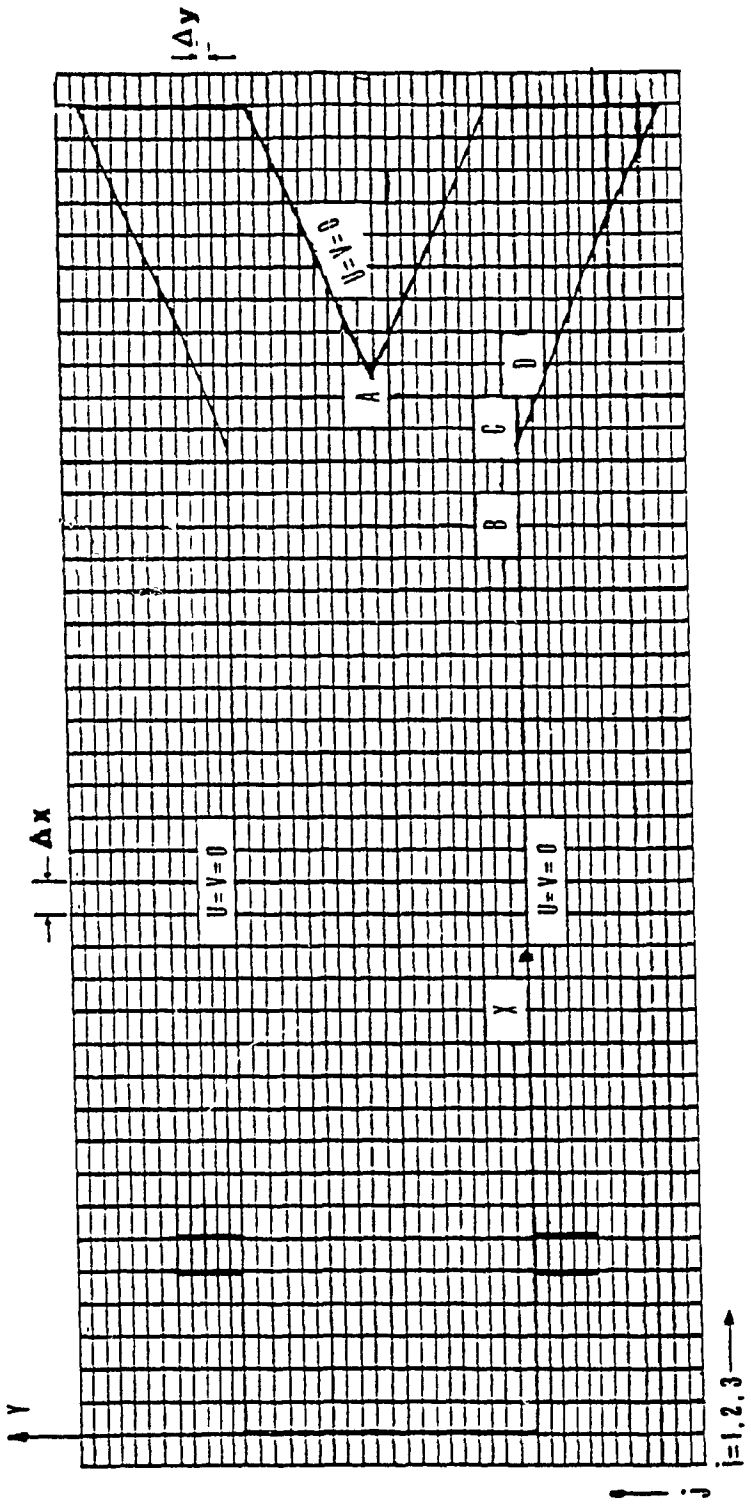

Fig. 6. Computational domain

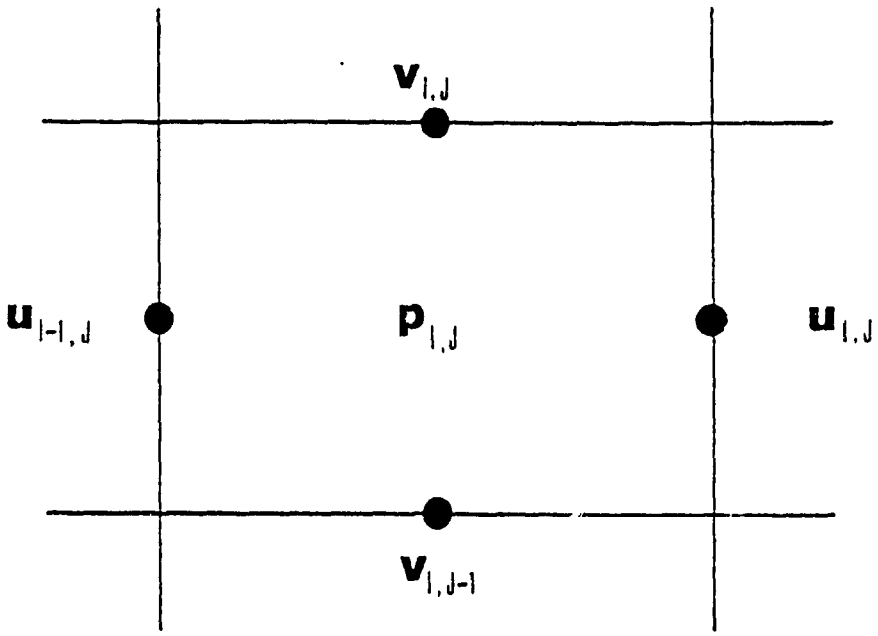

Fig. 7. Typical cell with the arrangement of finite difference variables

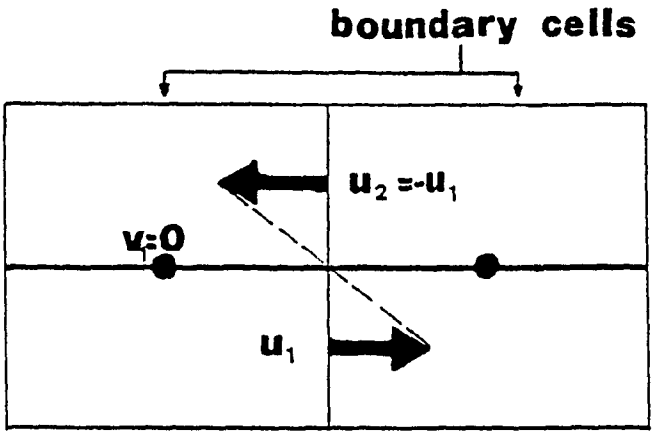

a) Straight wall

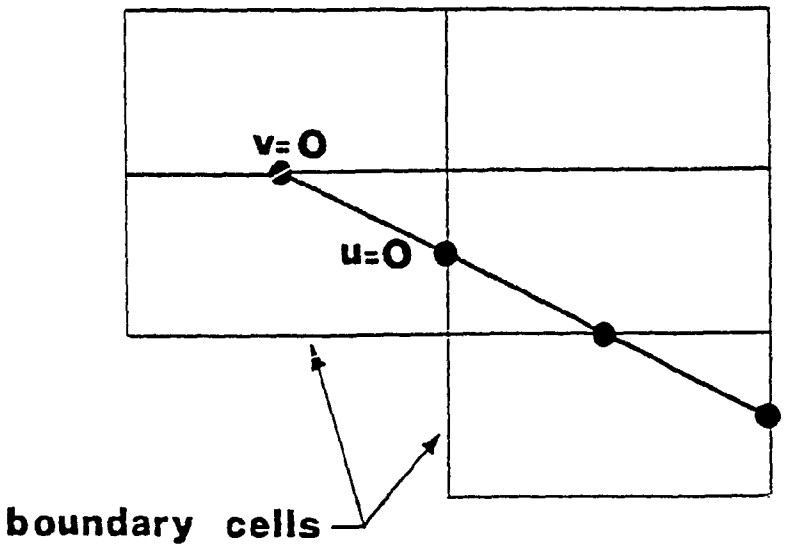

b) Wall at an angie

Fig. 8. No-slip boundary conditions

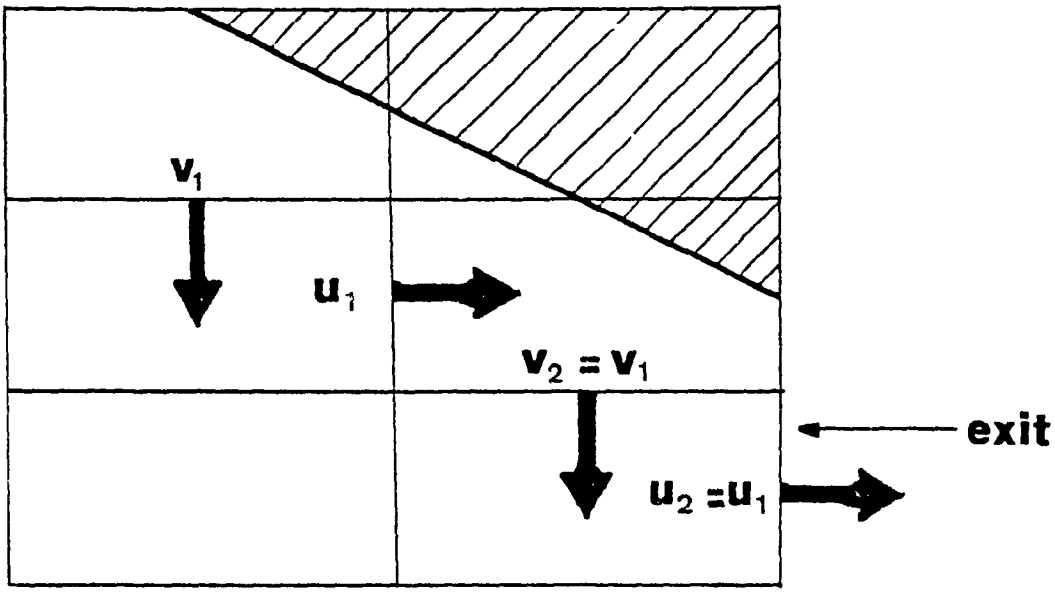

Fig. 9. Zero gradient boundary condition

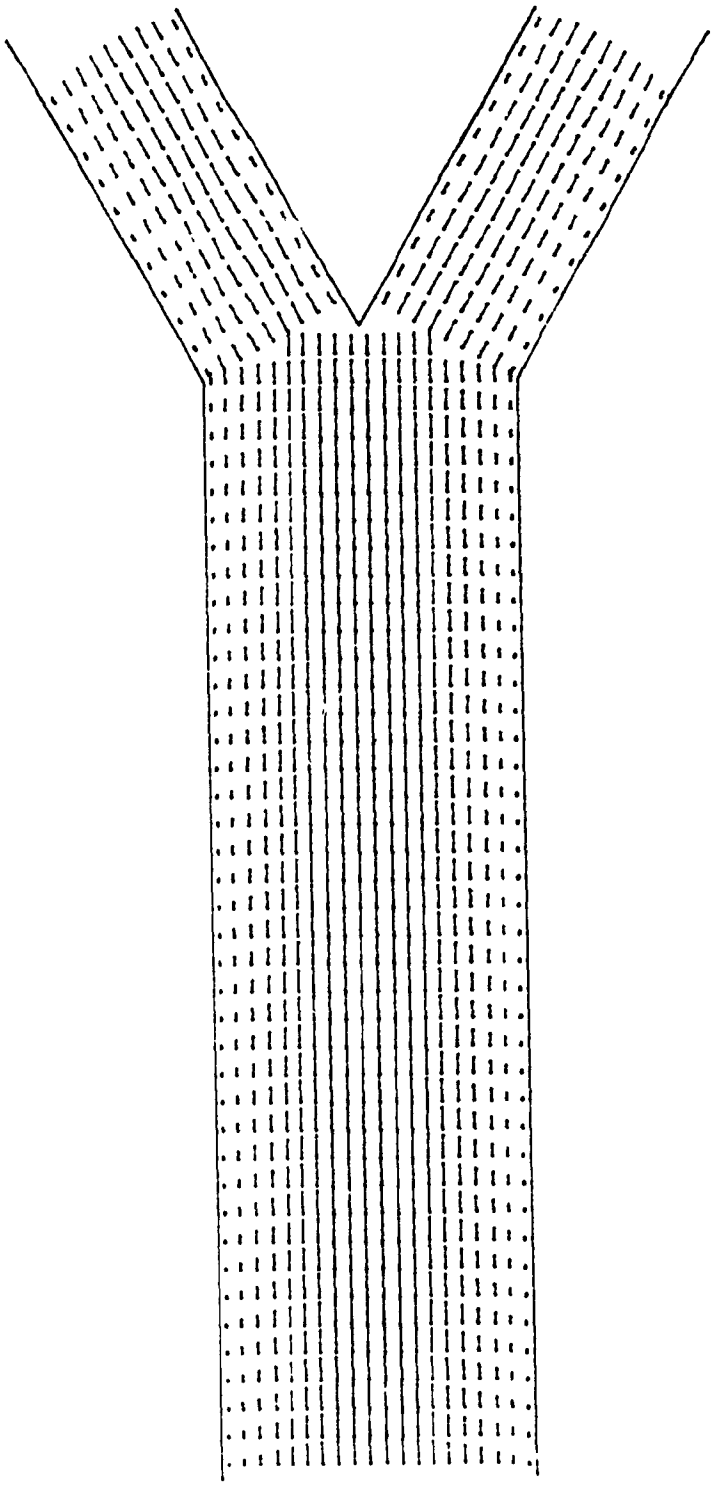

Fig. 10. Velocity plot . Steady, flow conditions, symmetrical inlet velocity, model I
(Re = 700, ϕ = 60°)

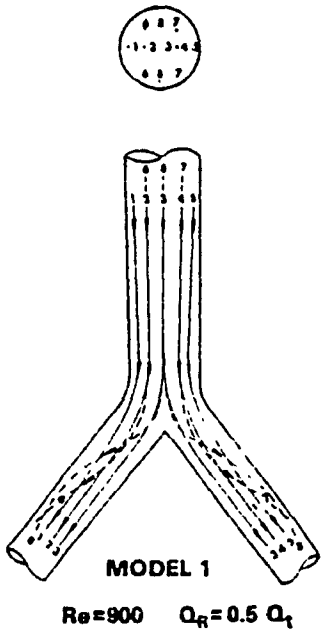

a) Stream line patterns from El Masry et. al [24]

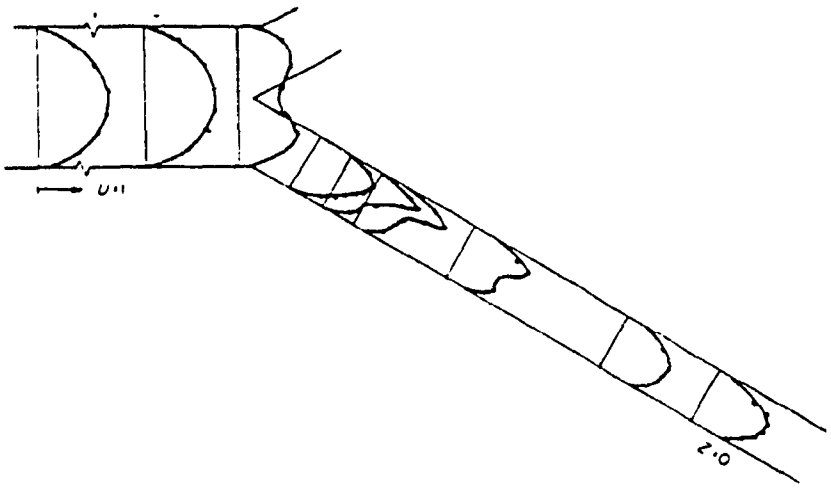

b) Spatial Variation of U, steady flow, Re = 900 Siouffi et. al [27]

Fig. 11. Velocity profiles obtained by other investigators

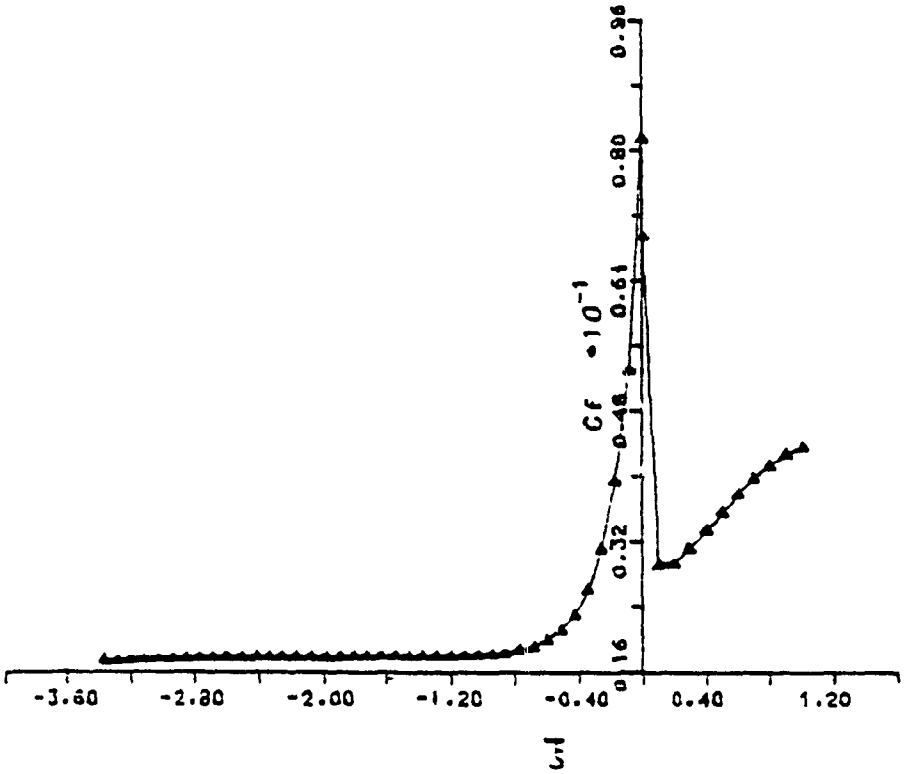

Fig. 12. Friction coefficient vs ξ. Symmetrical inlet velocity, model I, first and second wall (Re = 700, $\phi = 60°$)

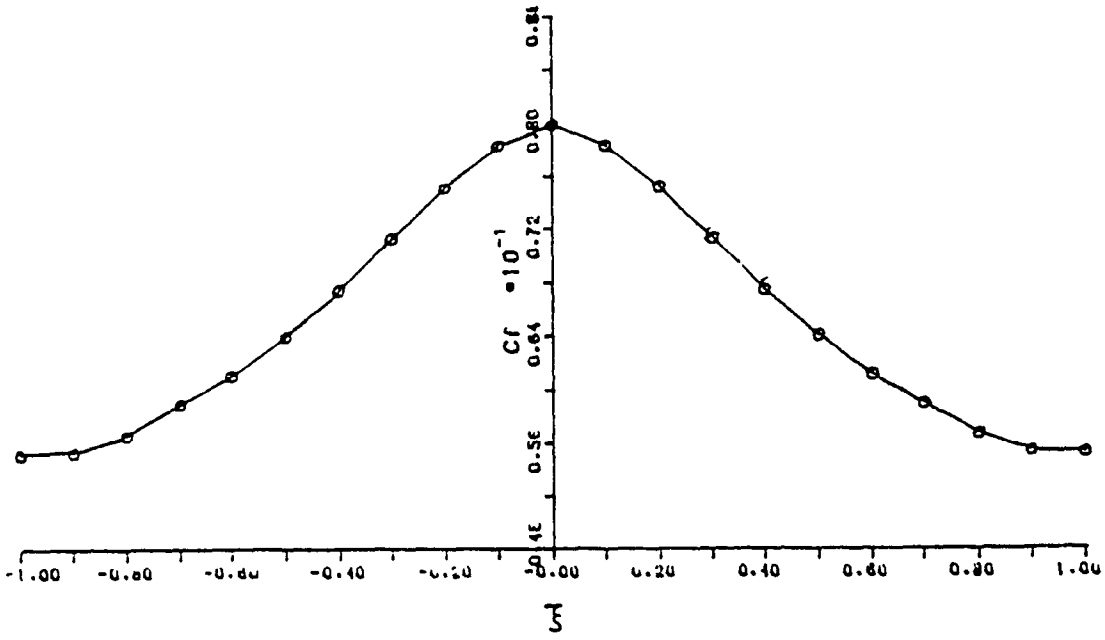

Fig. 13. Friction coefficient vs. ξ. Symmetrical inlet velocity, model I, third wall (Re = 700, $\phi = 60°$)

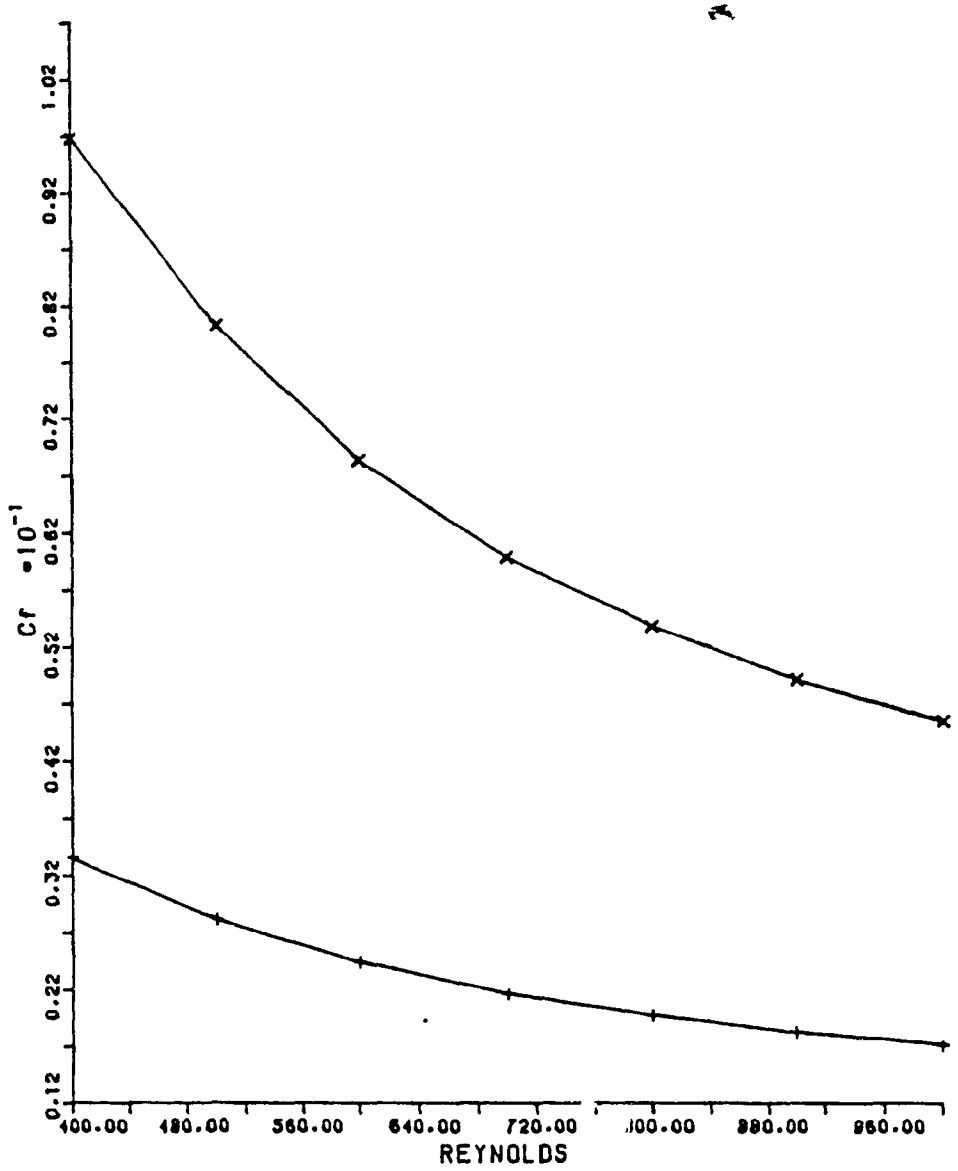

Fig. 14. Variation of maximum and minimum C_f with Reynolds number. Symmetrical inlet velocity, model I, first and second wall.
($\phi = 48°$, x - max, + - min)

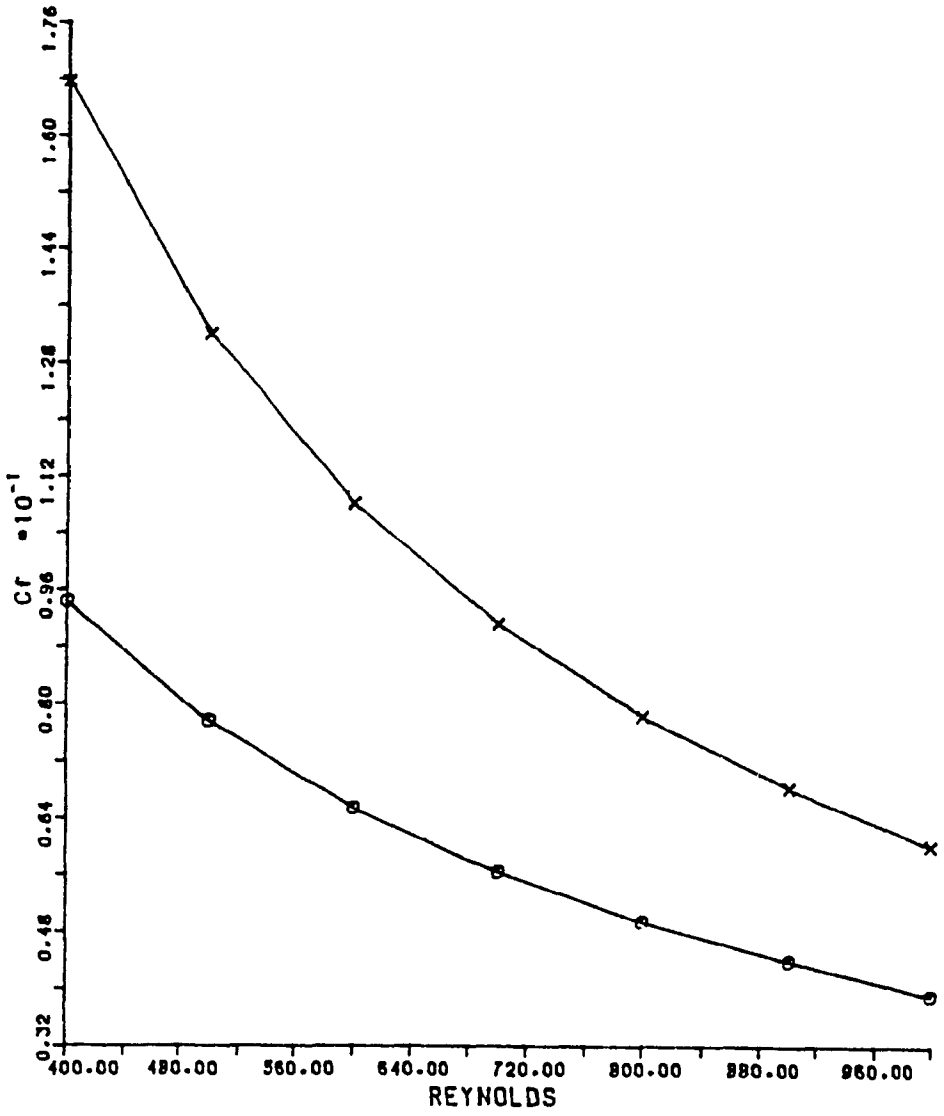

Fig. 15. Variation of maximum and minimum C_f with Reynolds number. Symmetrical inlet velocity, model I, third wall
($\phi = 48°$, x - max, 0 - min)

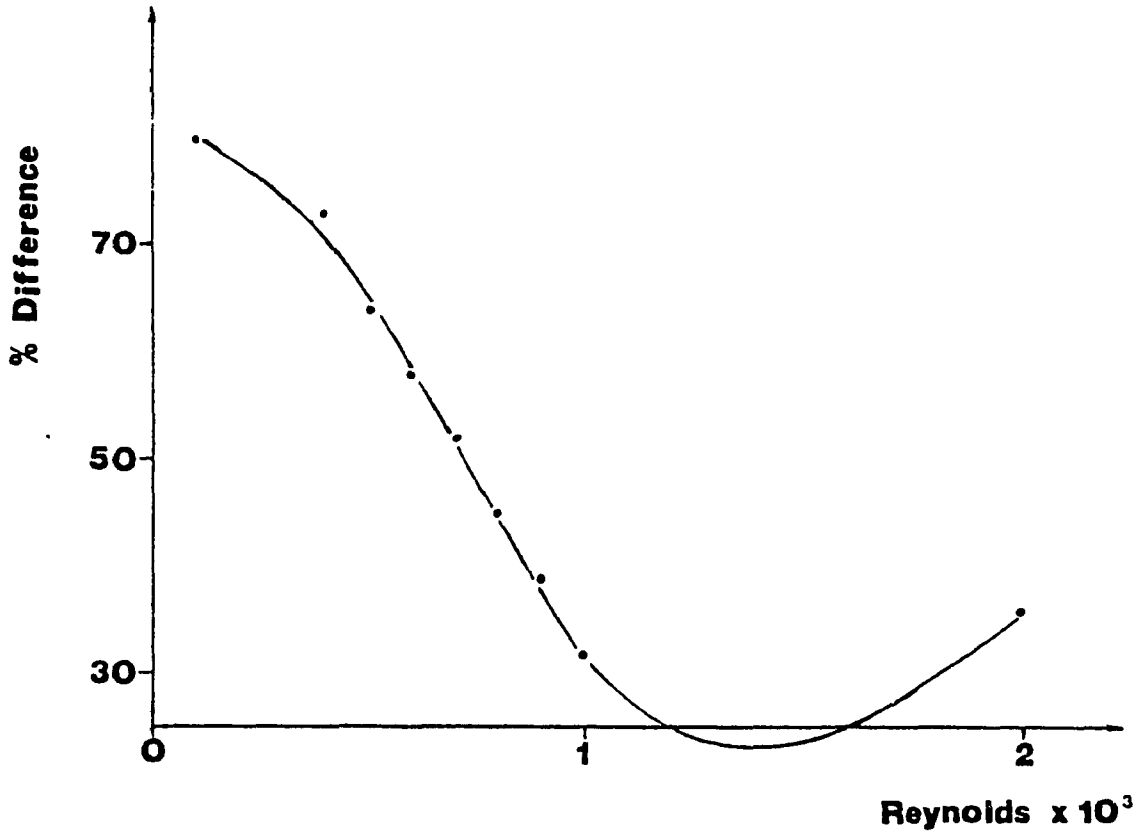

Fig. 16. Reynolds number vs difference between maximum friction coefficients on third and first walls as a percentage of the first

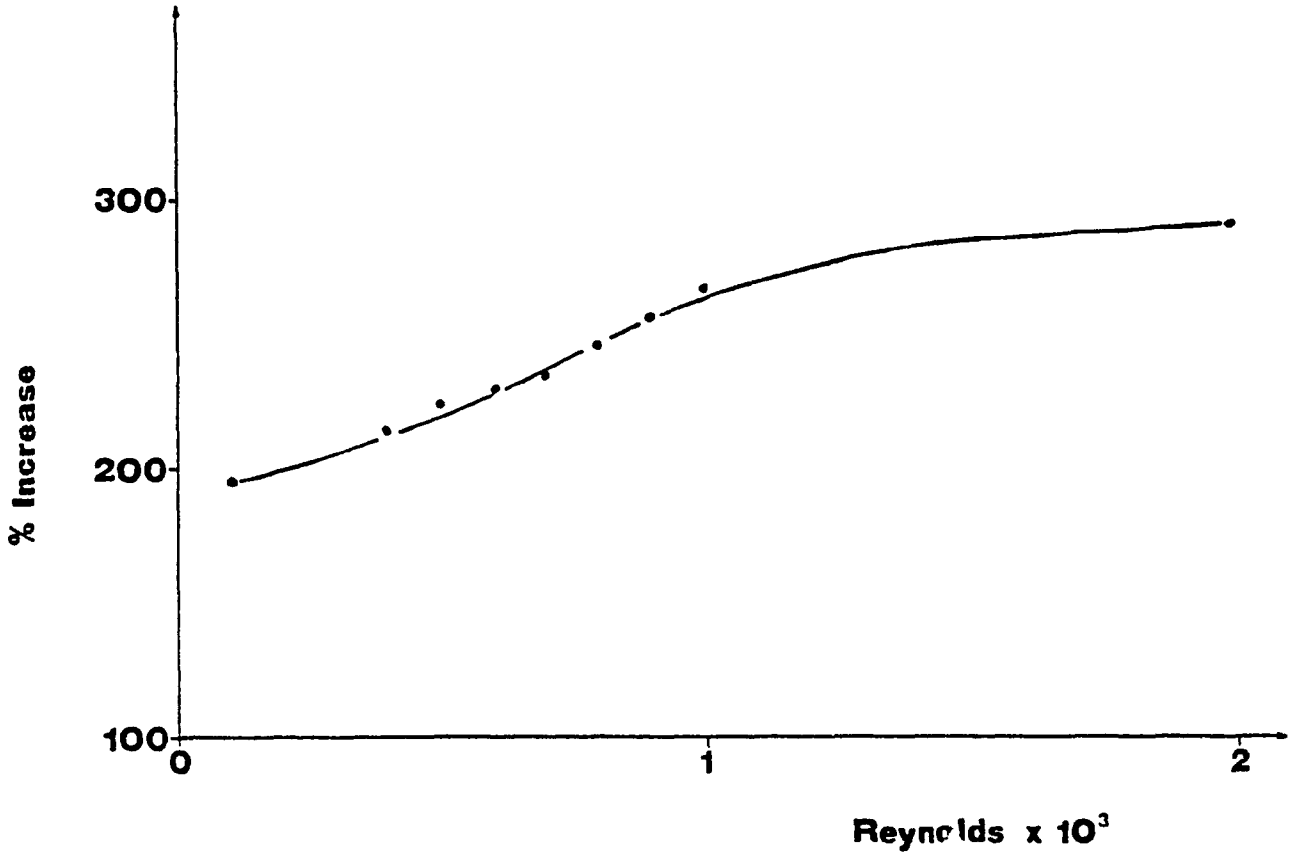

Fig. 17. Reynolds number vs percentage increase of C_f between points just before the bend and upstream on first and second walls.

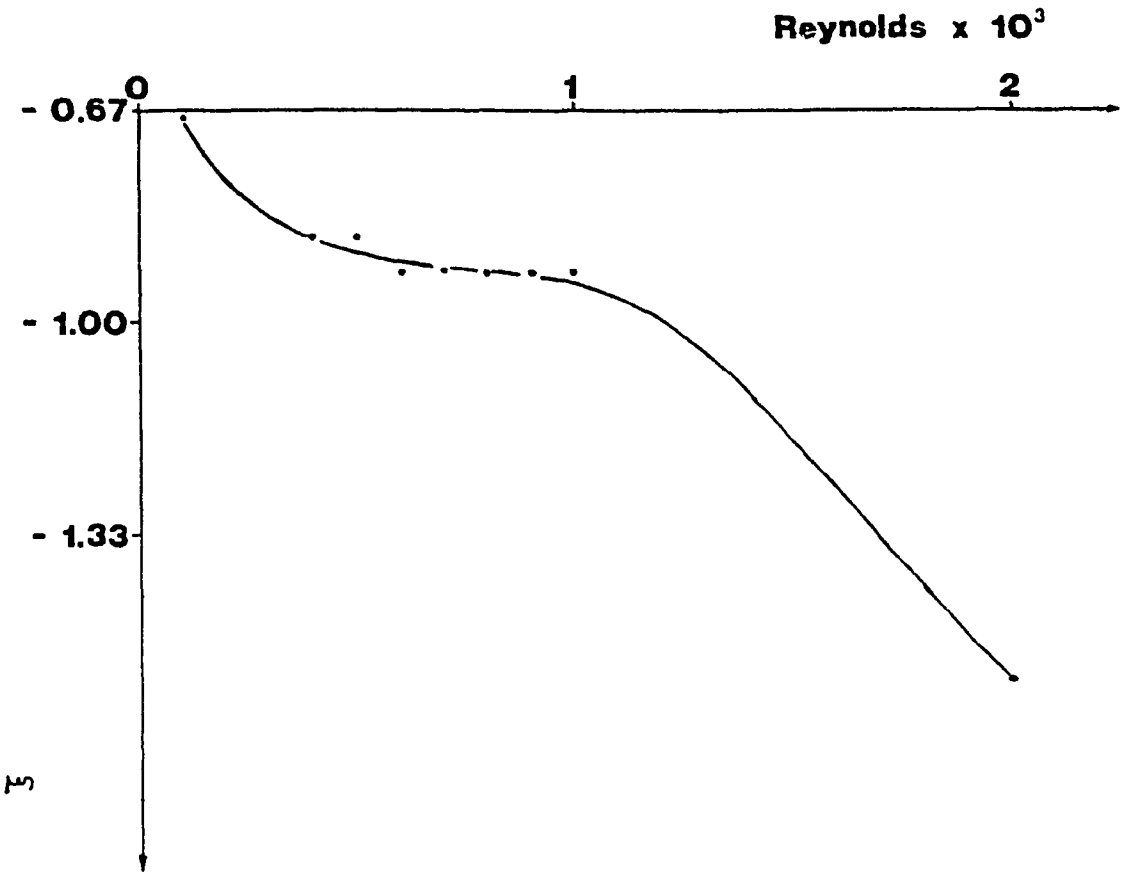

Fig. 18. Reynolds number vs position ξ where C_f starts rising surply on walls no. 1 and 2

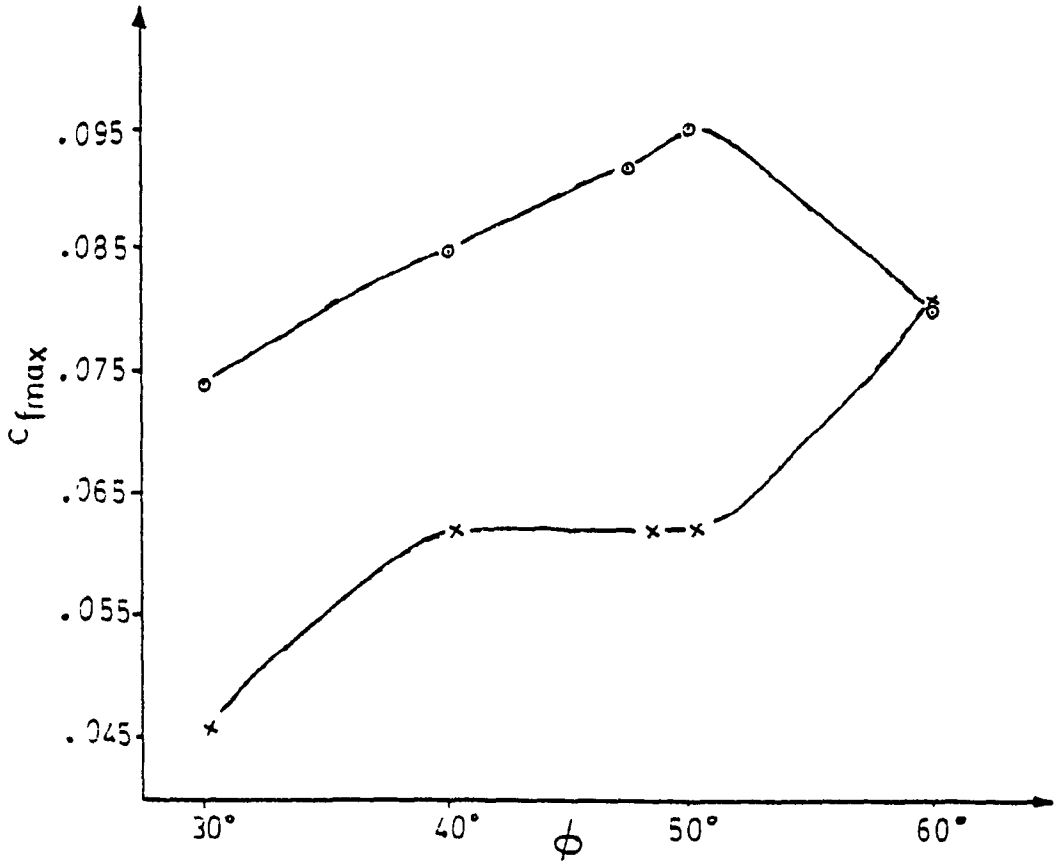

Fig. 19. Variation of maximum C_f with angle ϕ. Symmetrical inlet velocity, model I (Re = 700, 0 - wall 3, x - walls 1,2)

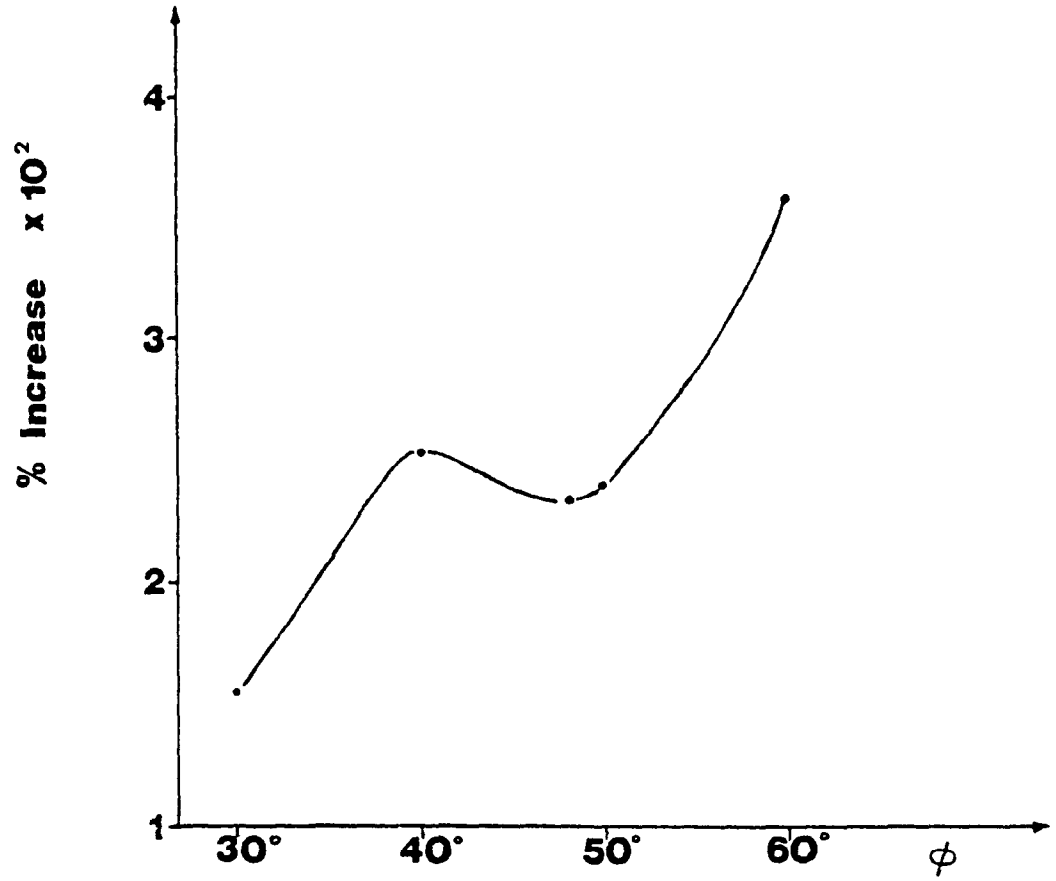

Fig. 20. Angle ϕ vs percent increase of C_f between points just before the bend and upstream on first and second walls (Re = 700)

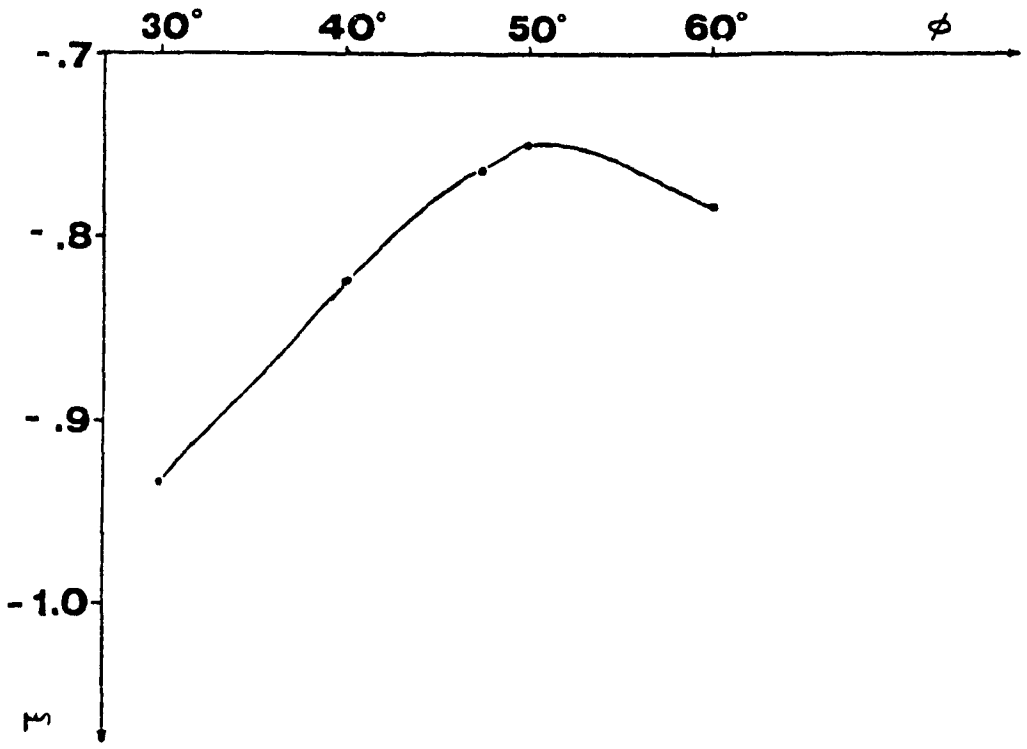

Fig. 21. Angle ϕ vs position ξ where C_f starts rising surply on walls no. 1 and 2 (Re = 700)

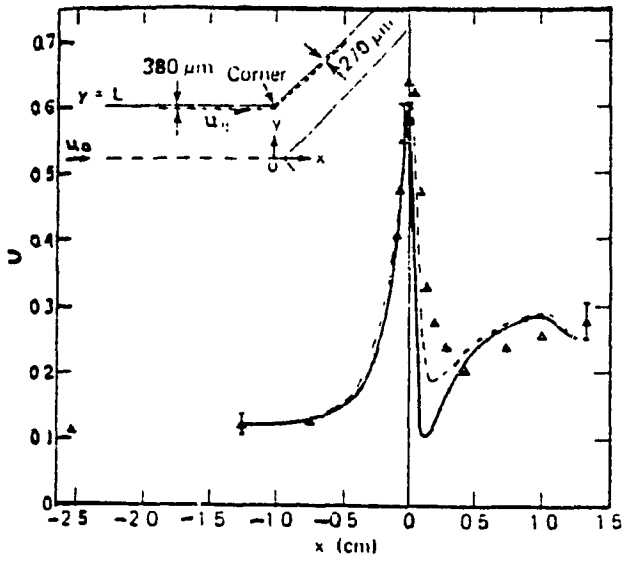

a) Velocity near the wall, steady flow, Re = 230 [34]

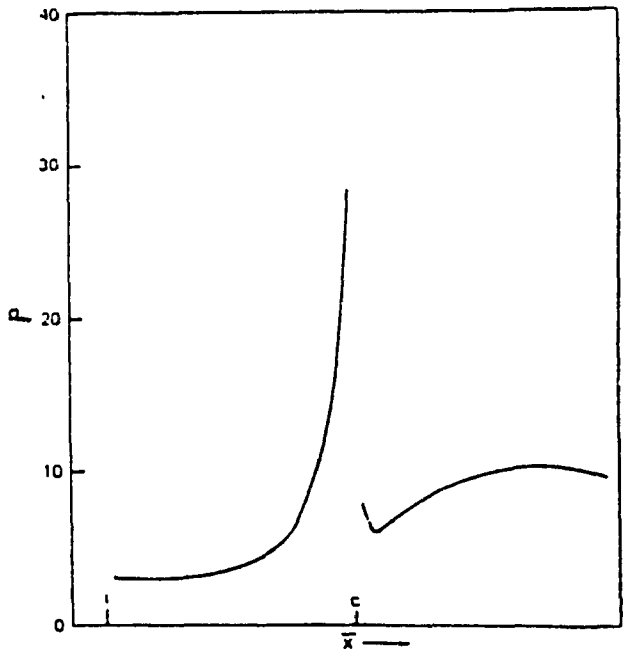

b) Non-dimensional shear profile on the outer wall [33]

Fig. 22. Comparison with C_f distributions of other researchers

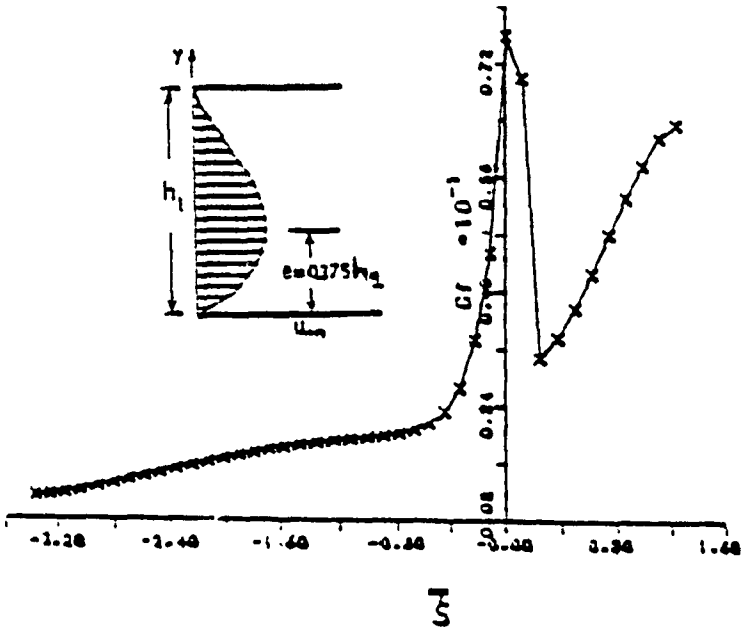

Fig. 23. C_f vs ξ for unsymmetrical inlet velocity, model I, first wall
(Re = 400, ϕ = 48°)

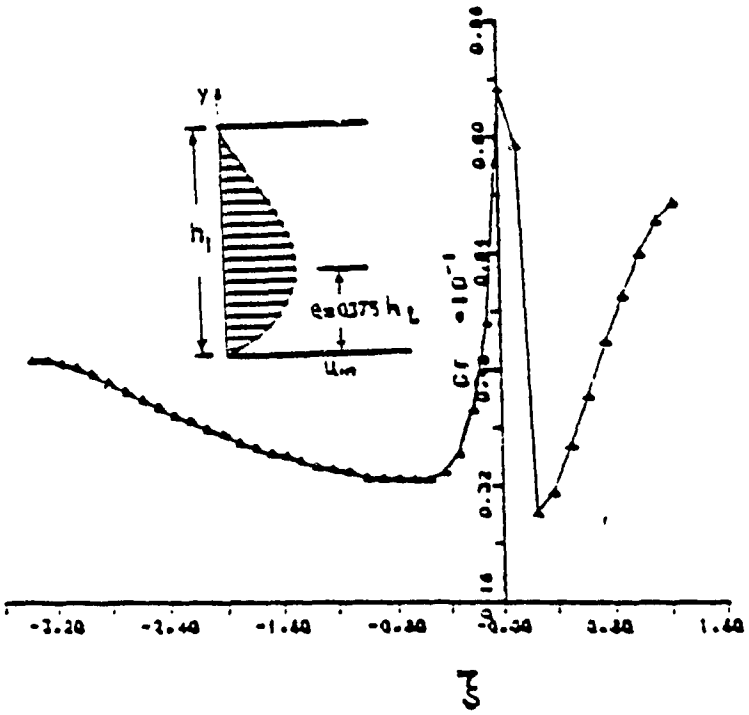

Fig. 24. C_f vs ξ. non-symmetrical inlet velocity, model I, second wall
(Re = 400, ϕ = 48°)

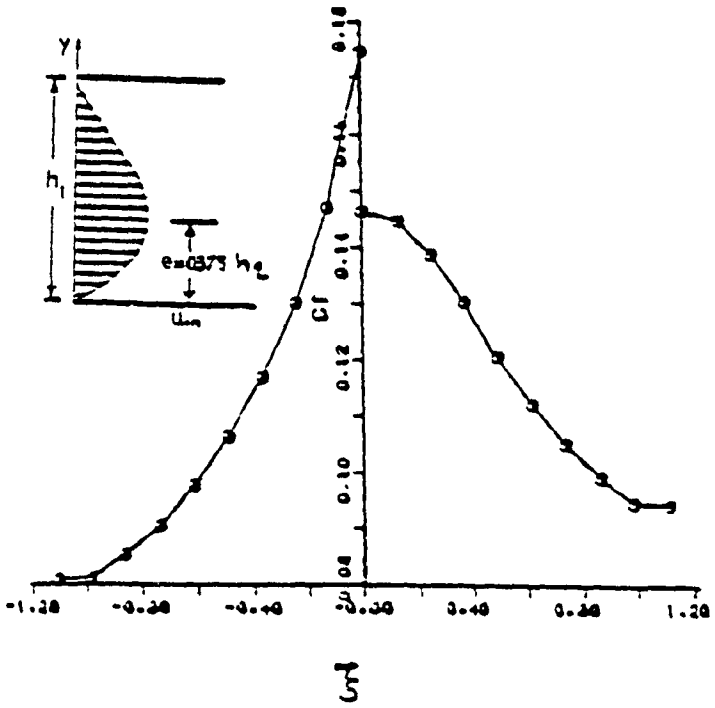

Fig. 25. C_f vs ξ for non-symmetrical inlet velocity, model I, third wall
(Re = 400, ϕ = 48°)

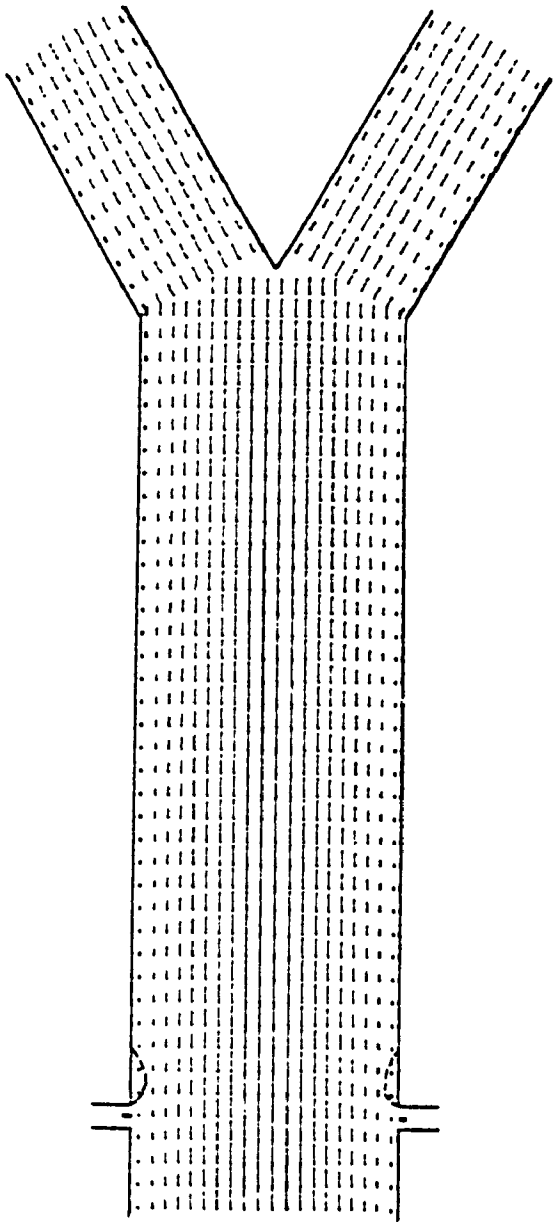

Fig. 26. Velocity plot. Steady flow conditions, Symmetrical inlet velocity, model II
(Re = 700, ϕ = 60°)

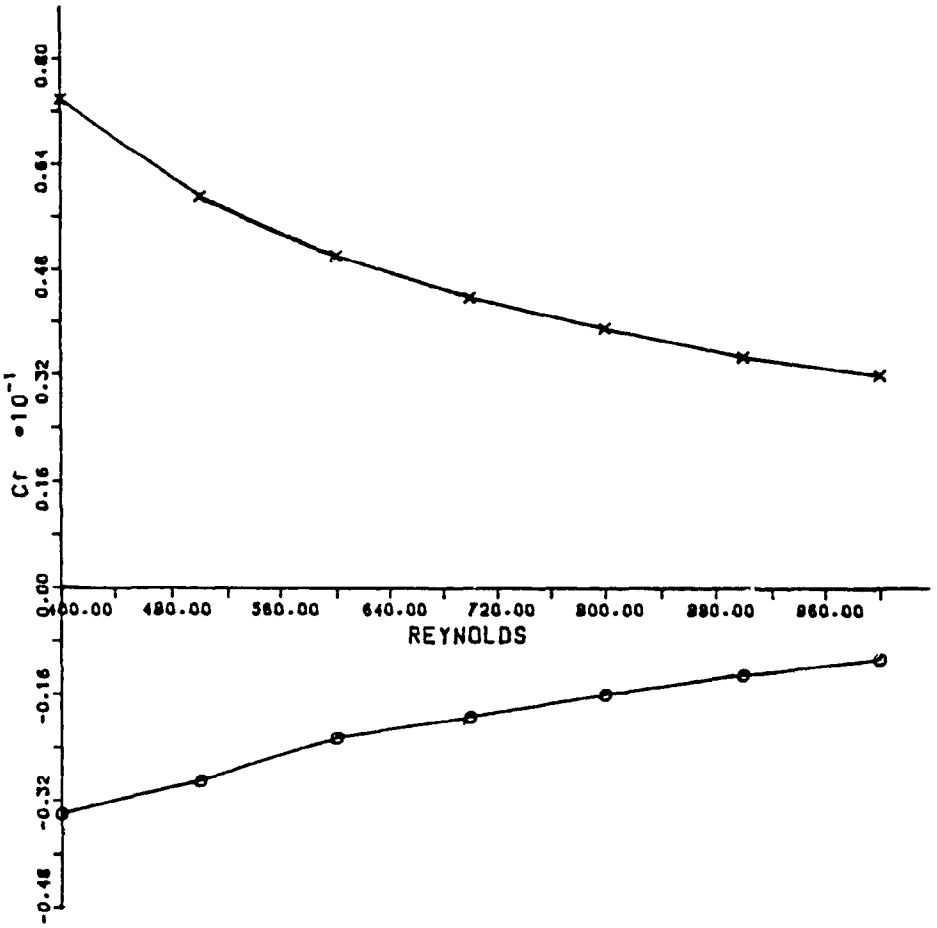

Fig. 27. Variation of maximum and minimum C_f with Reynolds number at the renal bifurcation for symmetrical inlet velocity

($\phi = 48°$, x - max, 0 - min)

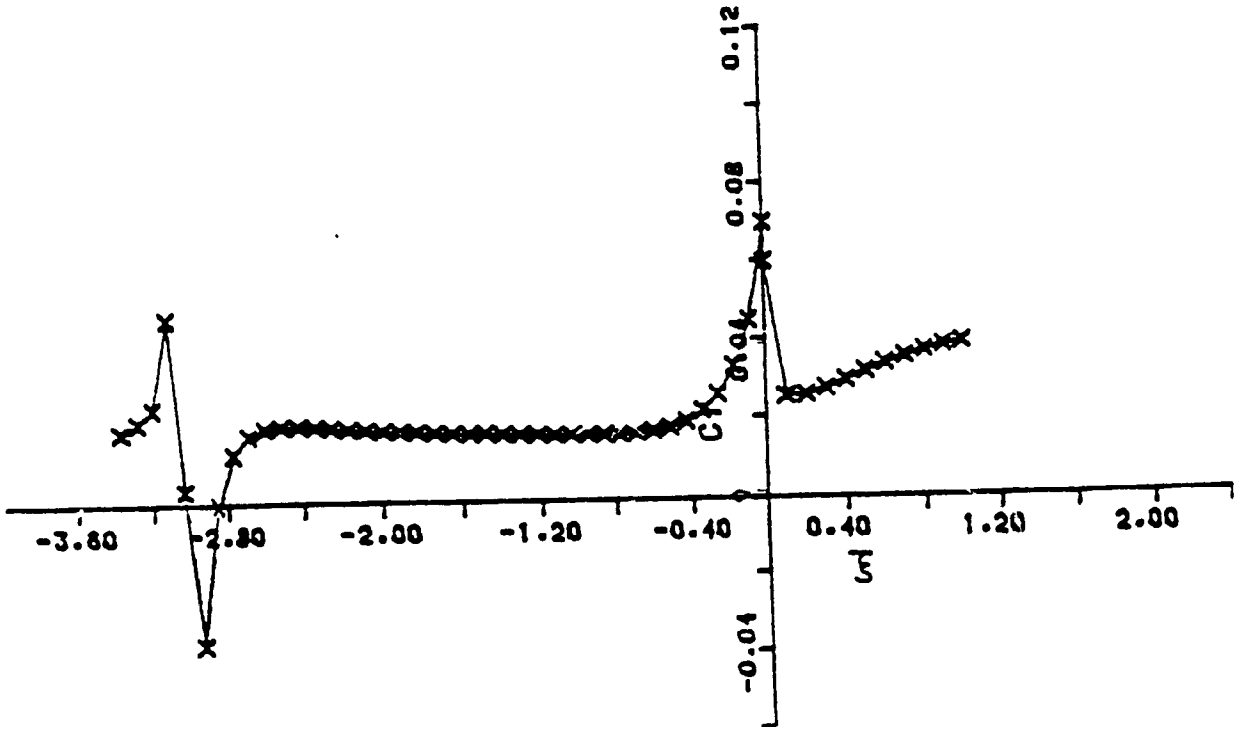

Fig. 28. C_f vs ξ for symmetrical inlet velocity, model II, first and second wall ($Re = 700$, $\phi = 60°$, $Q_2 = Q_3 = 5\%\ Q_1$)

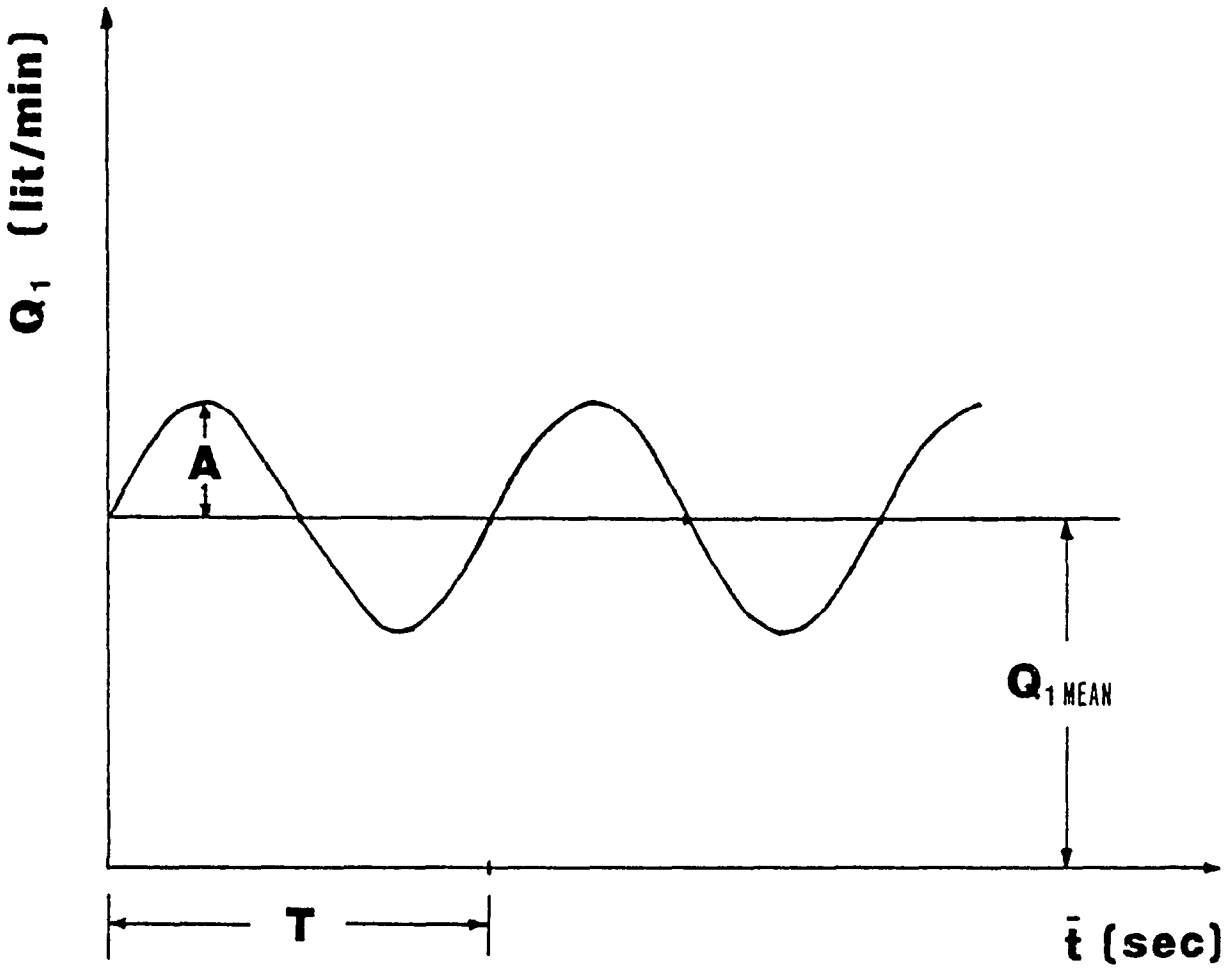

Fig. 29. Sinusoidal input for pulsatile flow conditions

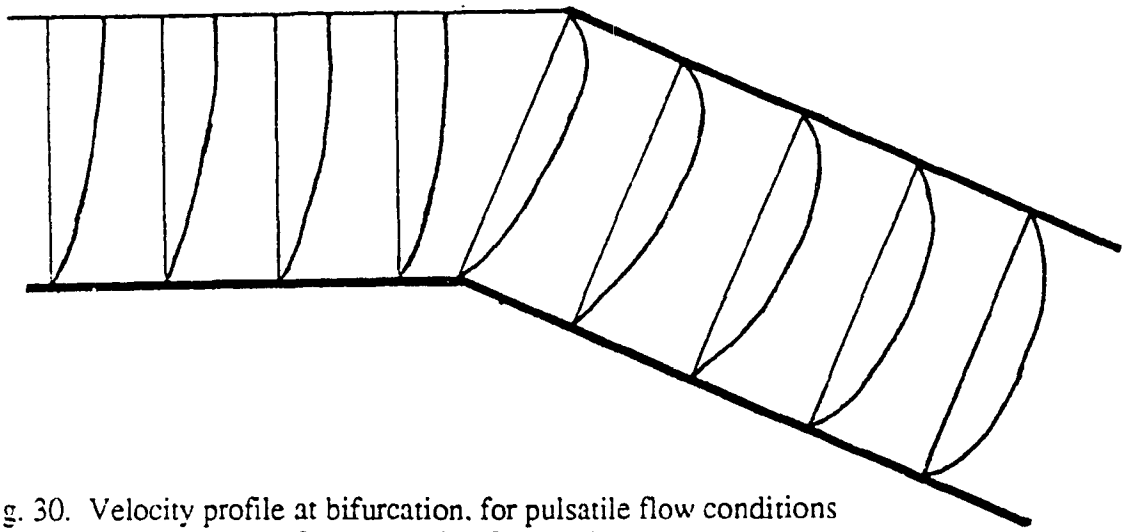

Fig. 30. Velocity profile at bifurcation, for pulsatile flow conditions
($T = 1.0$ sec, $A = 0.1\ Q_{1MEAN}$)

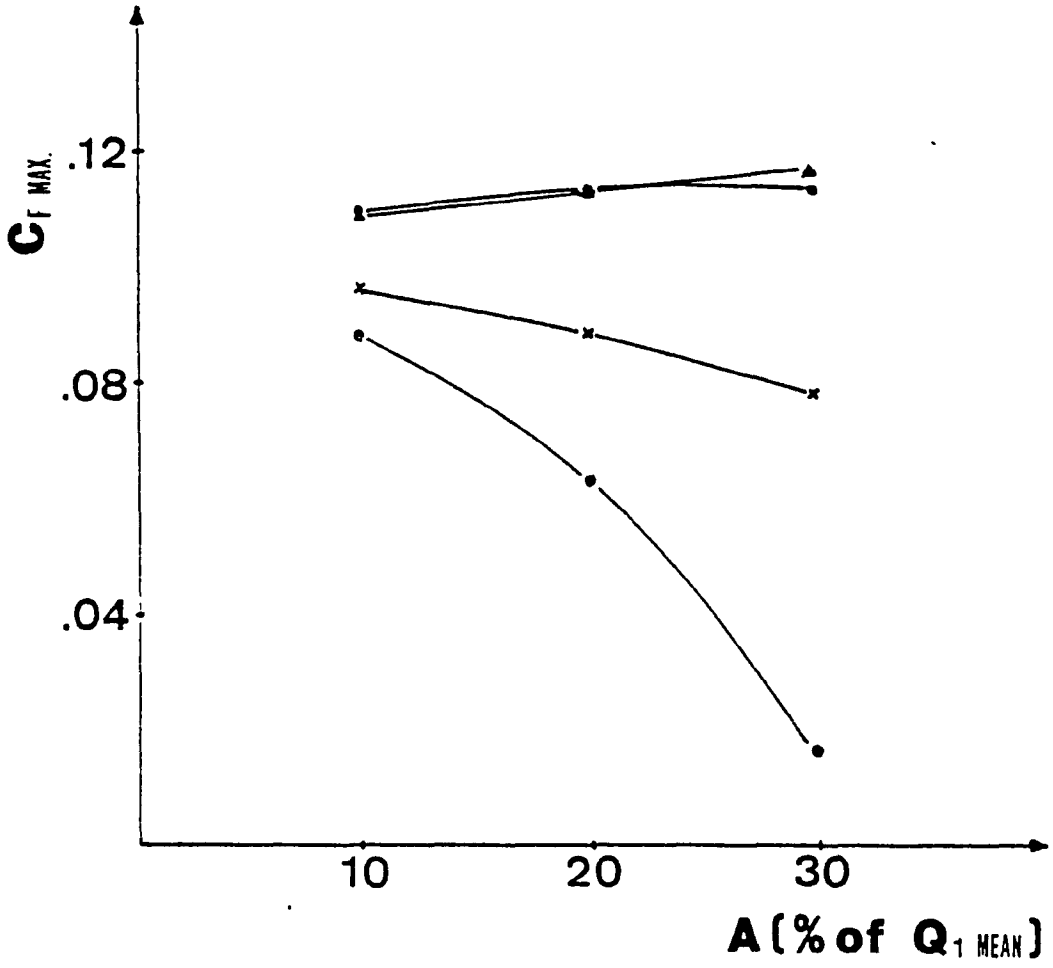

Fig. 31. C_{fmax} vs amplitude of oscillation A for T = 1.0 sec, first and second walls
(• - T/4, x - t/2, 0 - 3T/4, ▲ - T)

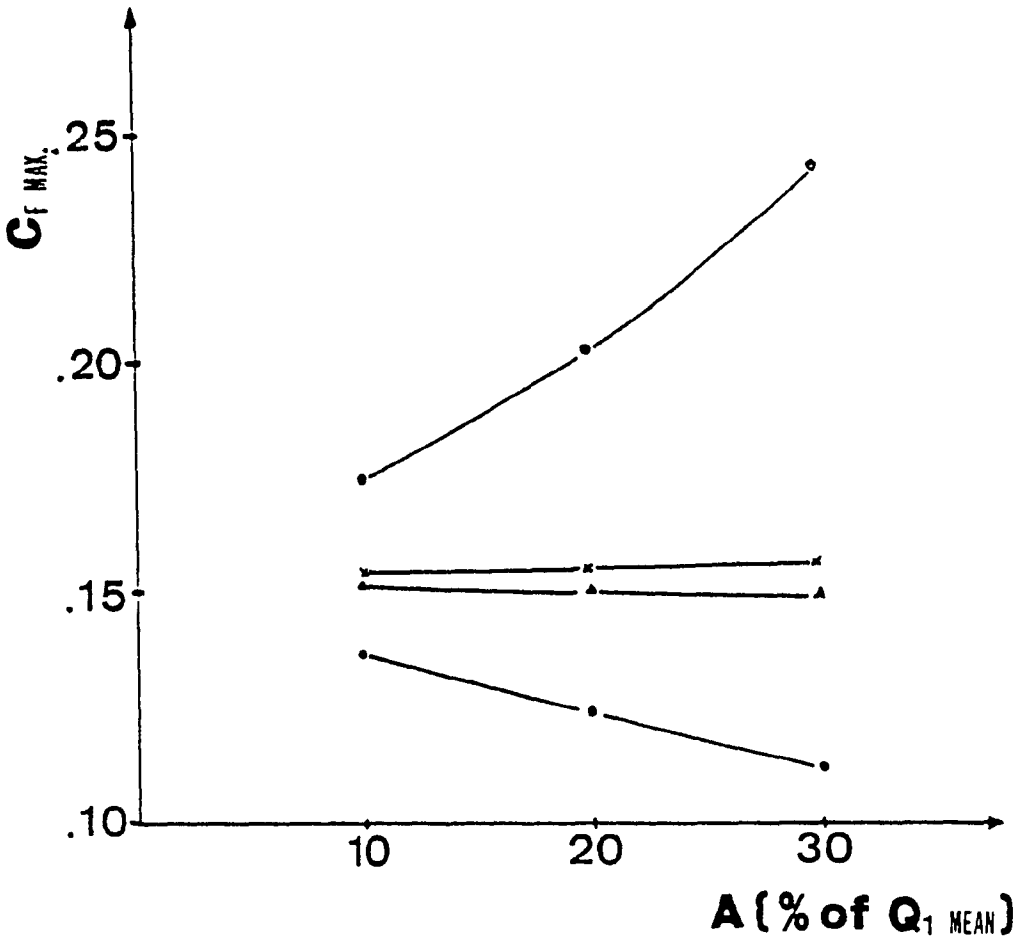

Fig. 32. C_{fmax} vs amplitude of oscillation A for T = 1.0 sec, third walls
(• - T/4, x - t/2, 0 - 3T/4, ▲ - T)

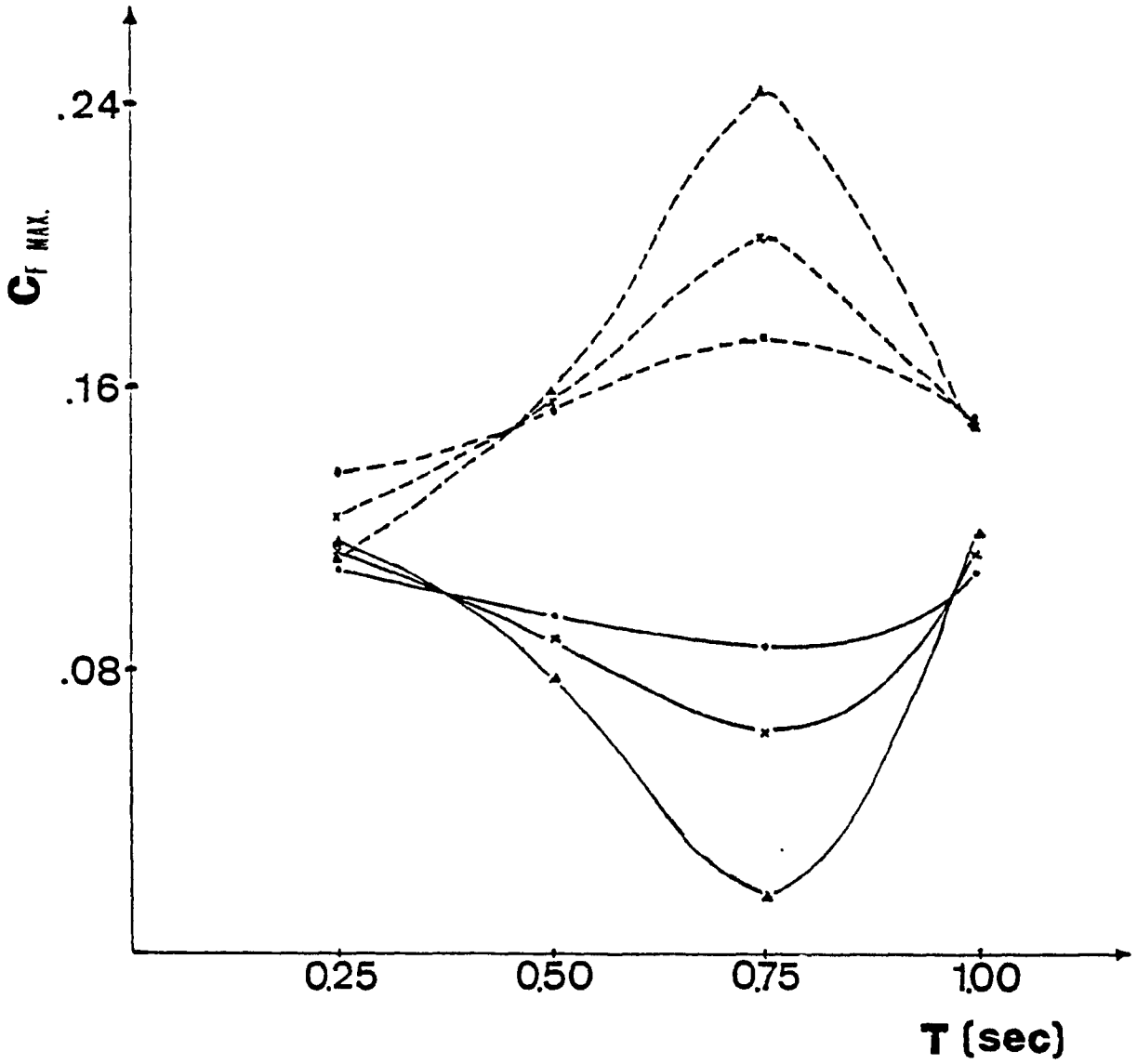

Fig. 33. C_{fmax} vs time for T = 1.0 sec (— first and second walls, ----third wall, • - A = 0.1, x - A = 0.2, ▲ - A = 0.3)

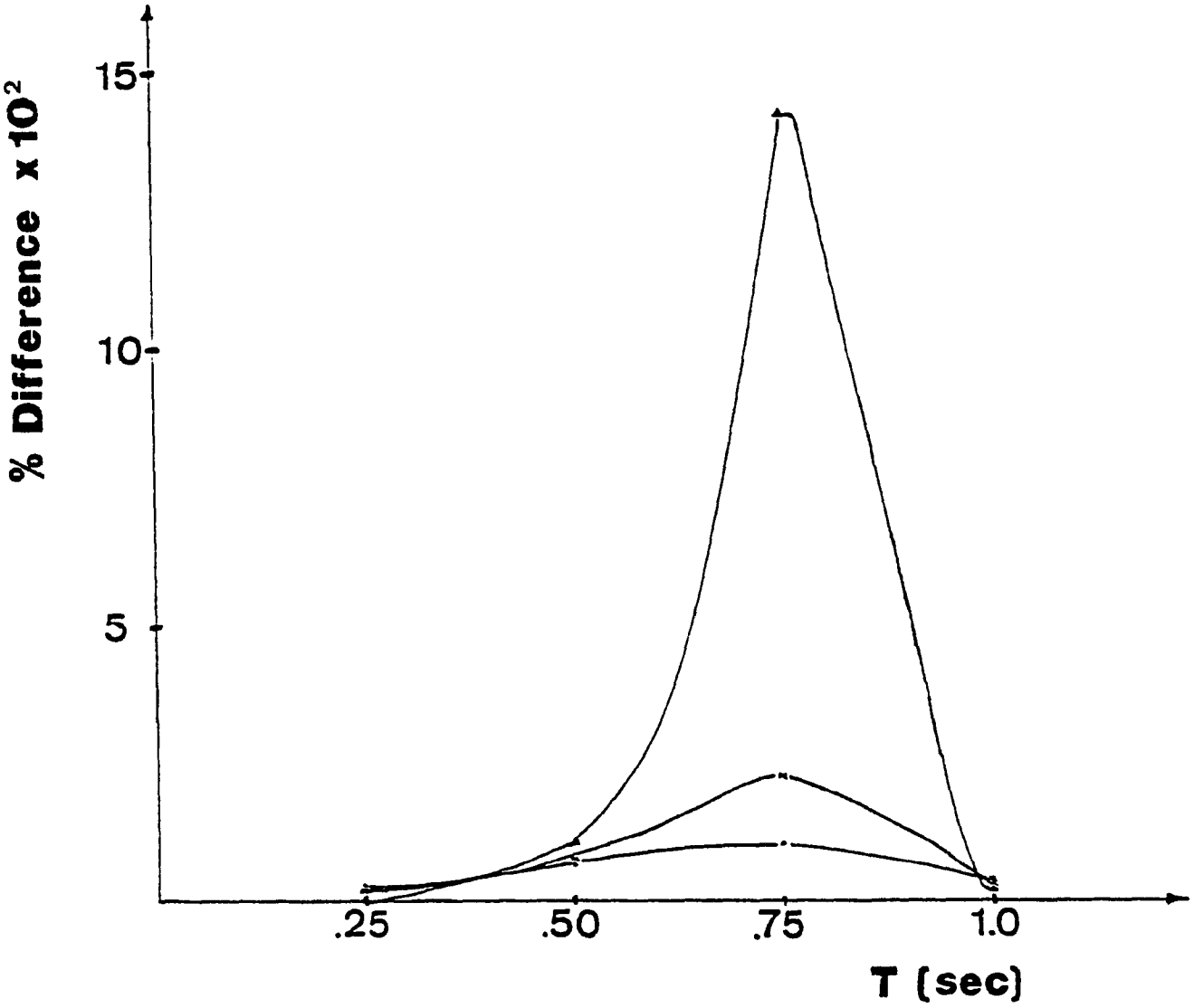

Fig. 34. Percent difference of C_{fmax} at third wall to C_{fmax} at first and second walls vs time for T = 1.0 (• - A = 0.1, x - A - 0.2, ▲ - A = 0.3)

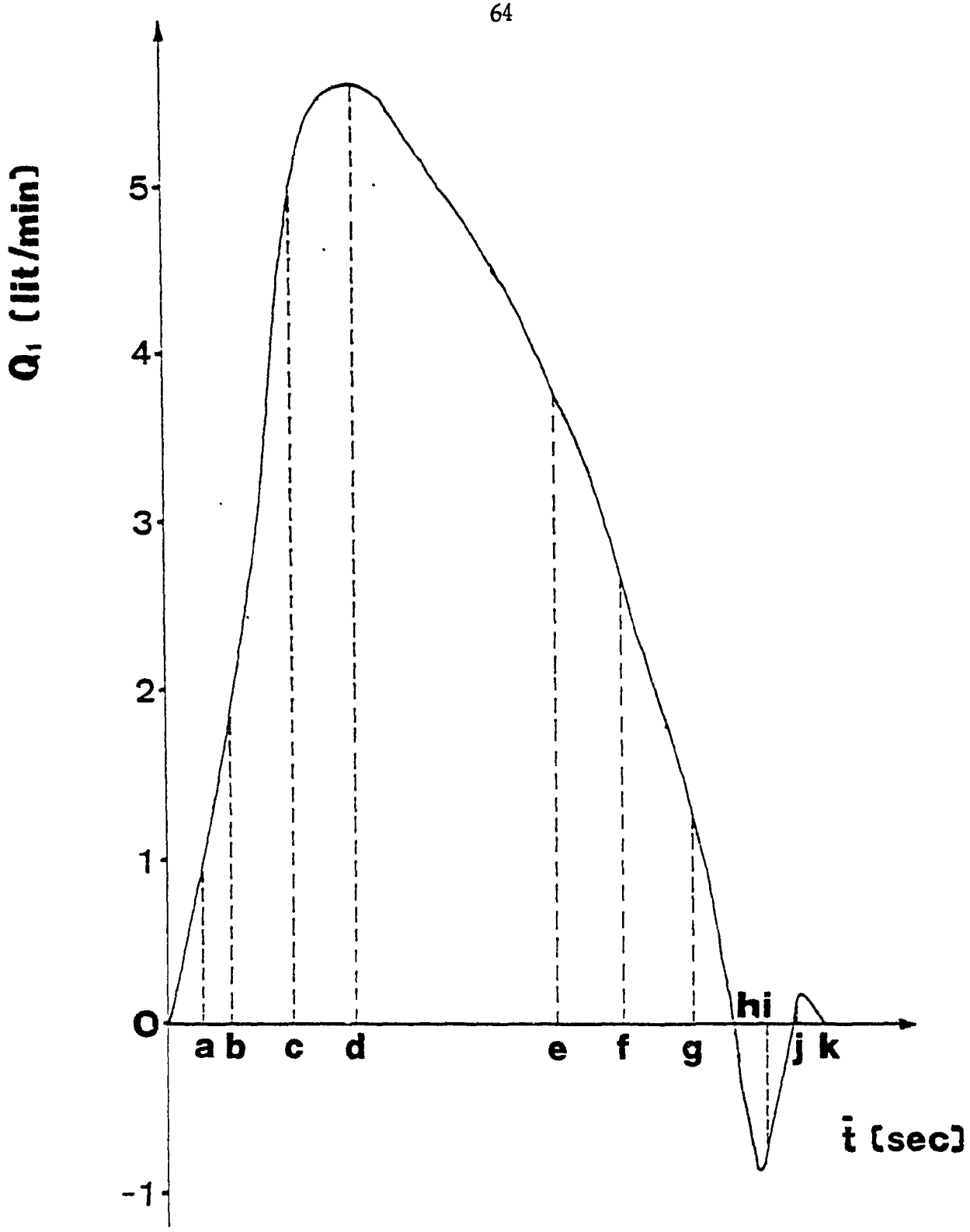

Fig. 35. Flow rate input for physiological flow conditions

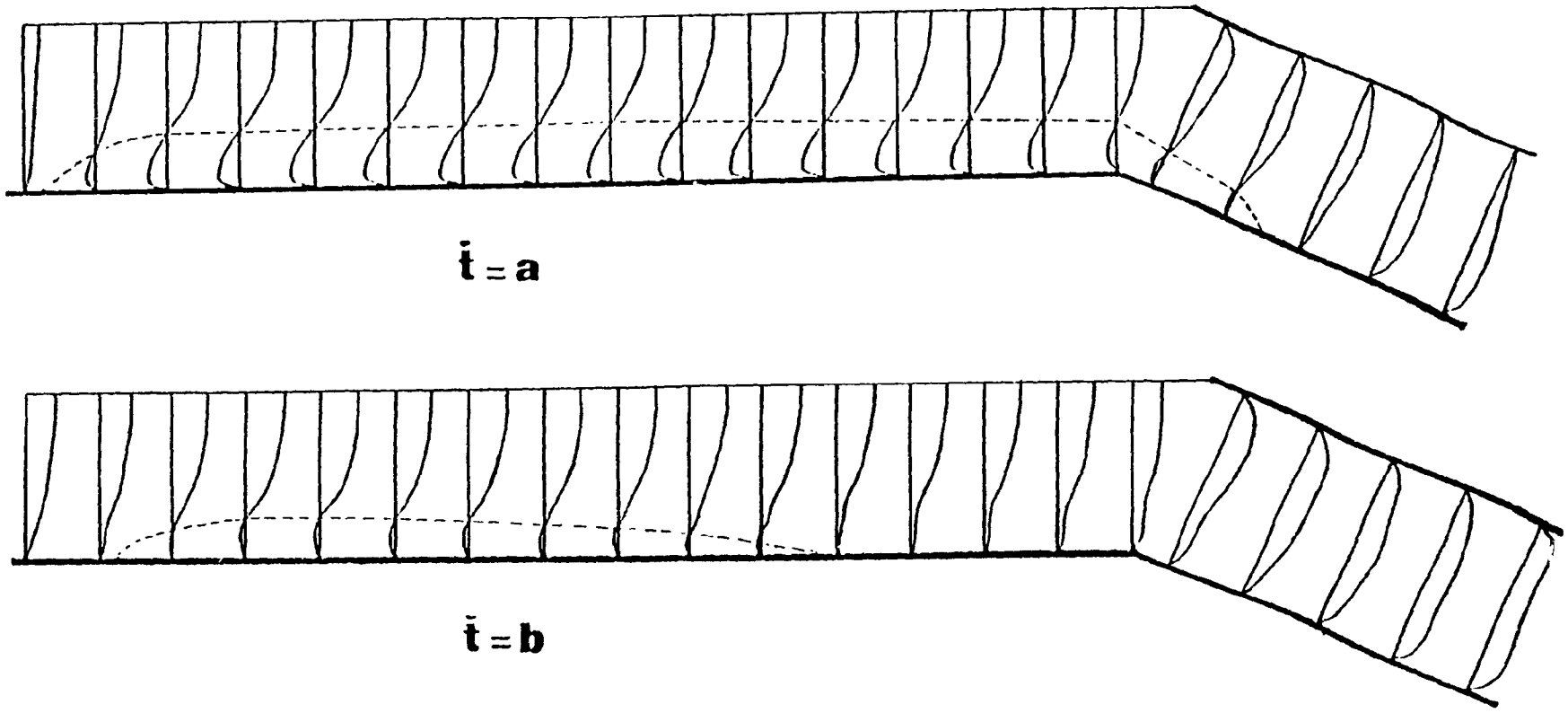

Fig. 36. Velocity profiles at early systole

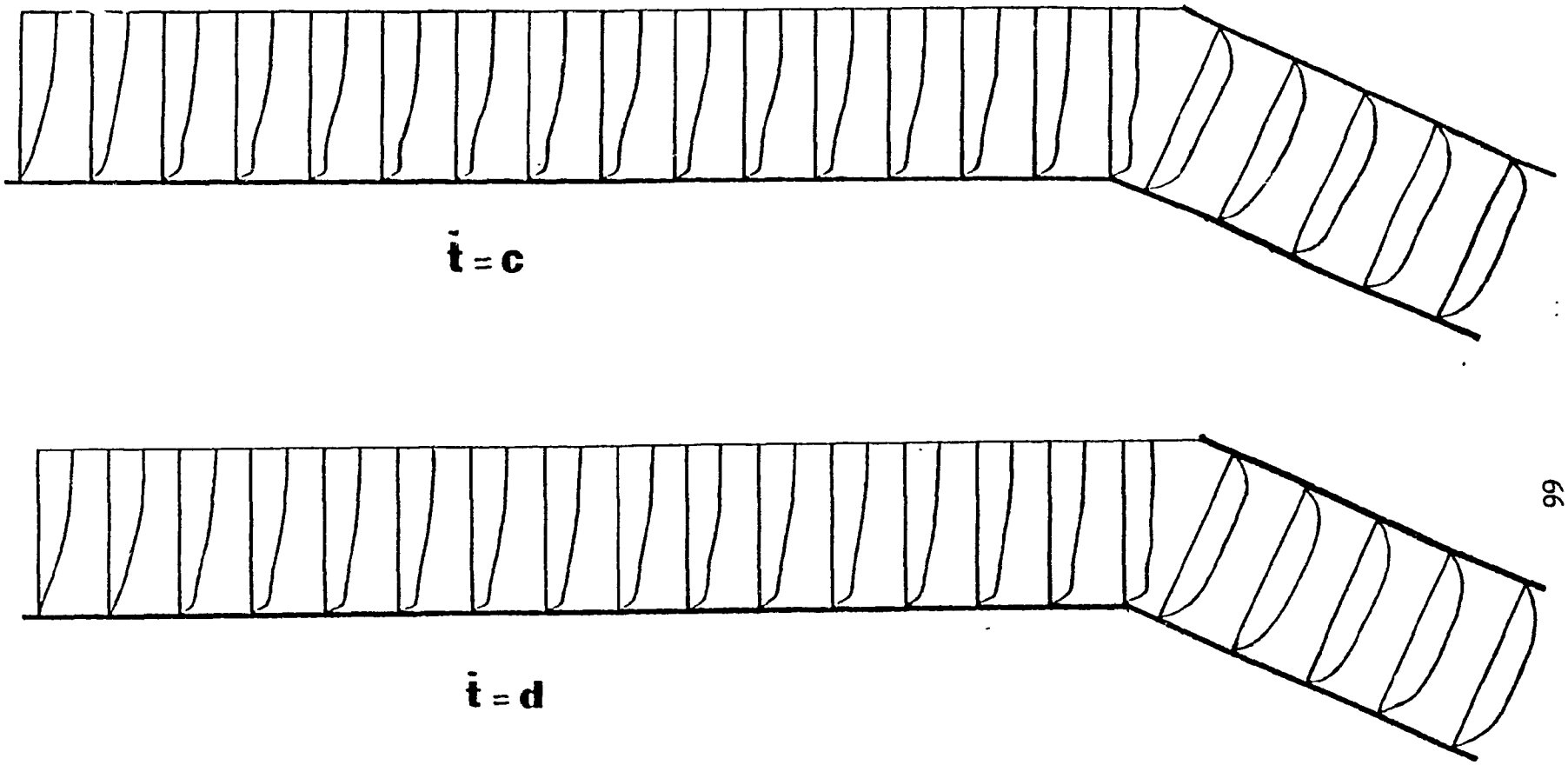

Fig. 37. Velocity profiles at peak systole

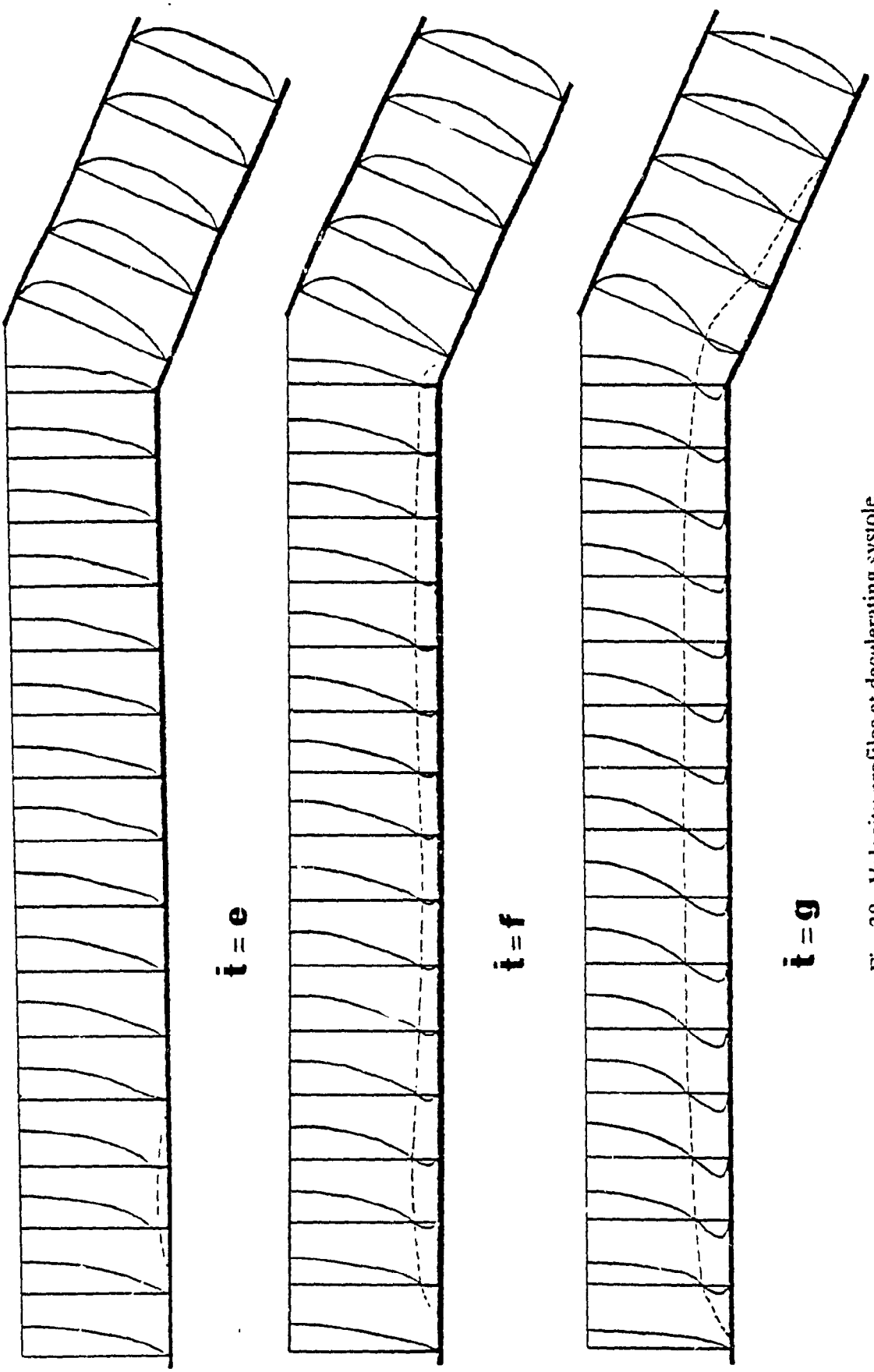

Fig. 38. Velocity profiles at decelerating systole

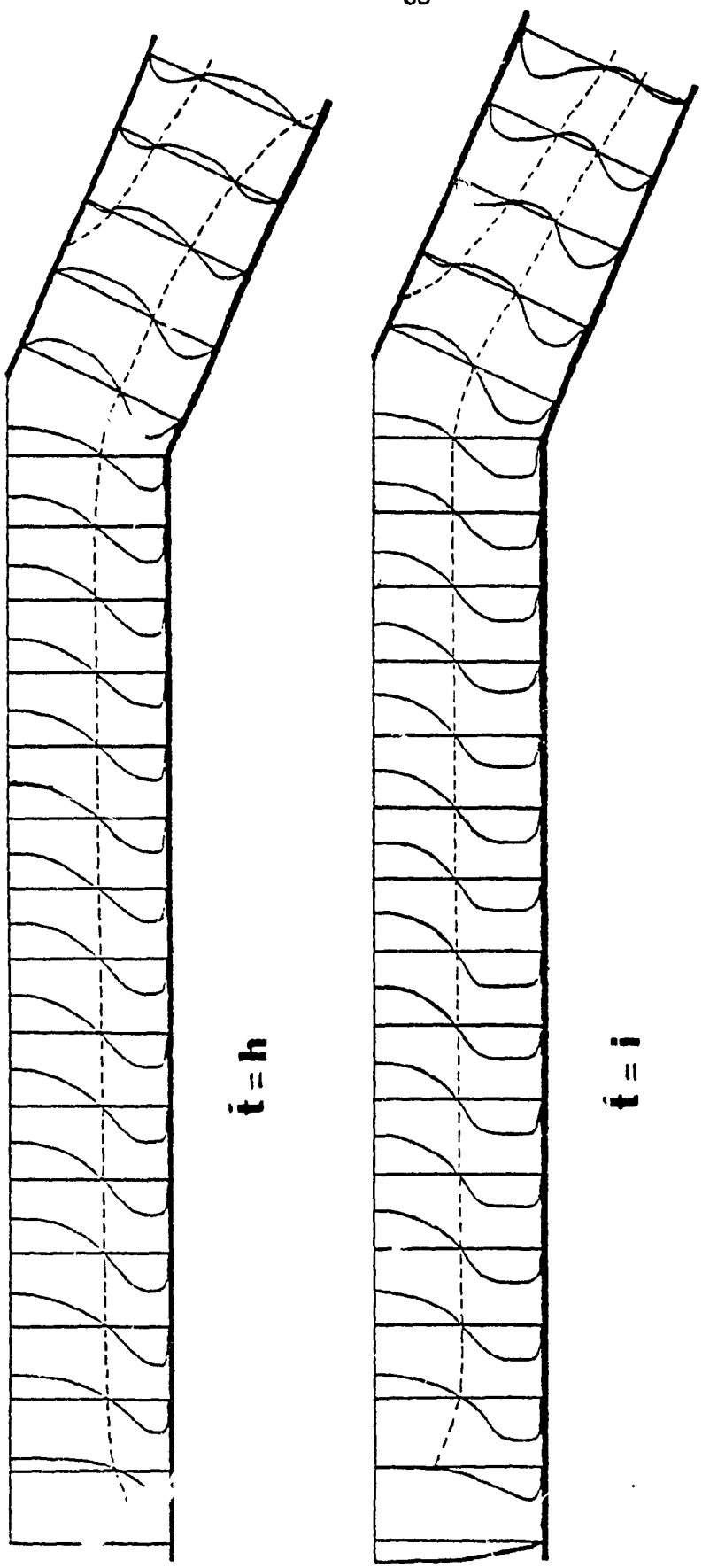

Fig. 39. Velocity profiles at diastole

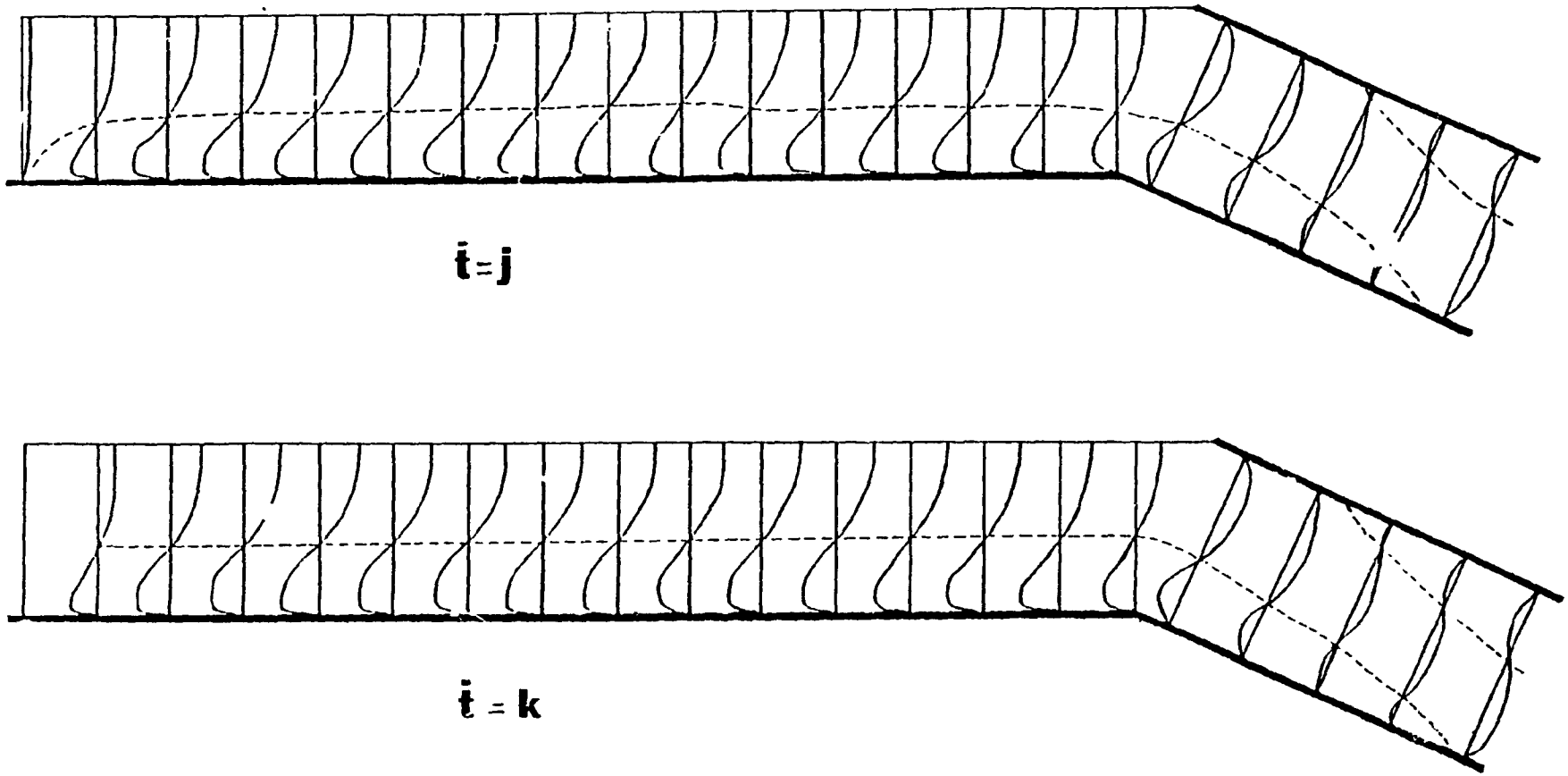

Fig. 40. Velocity profiles at last stages of period T

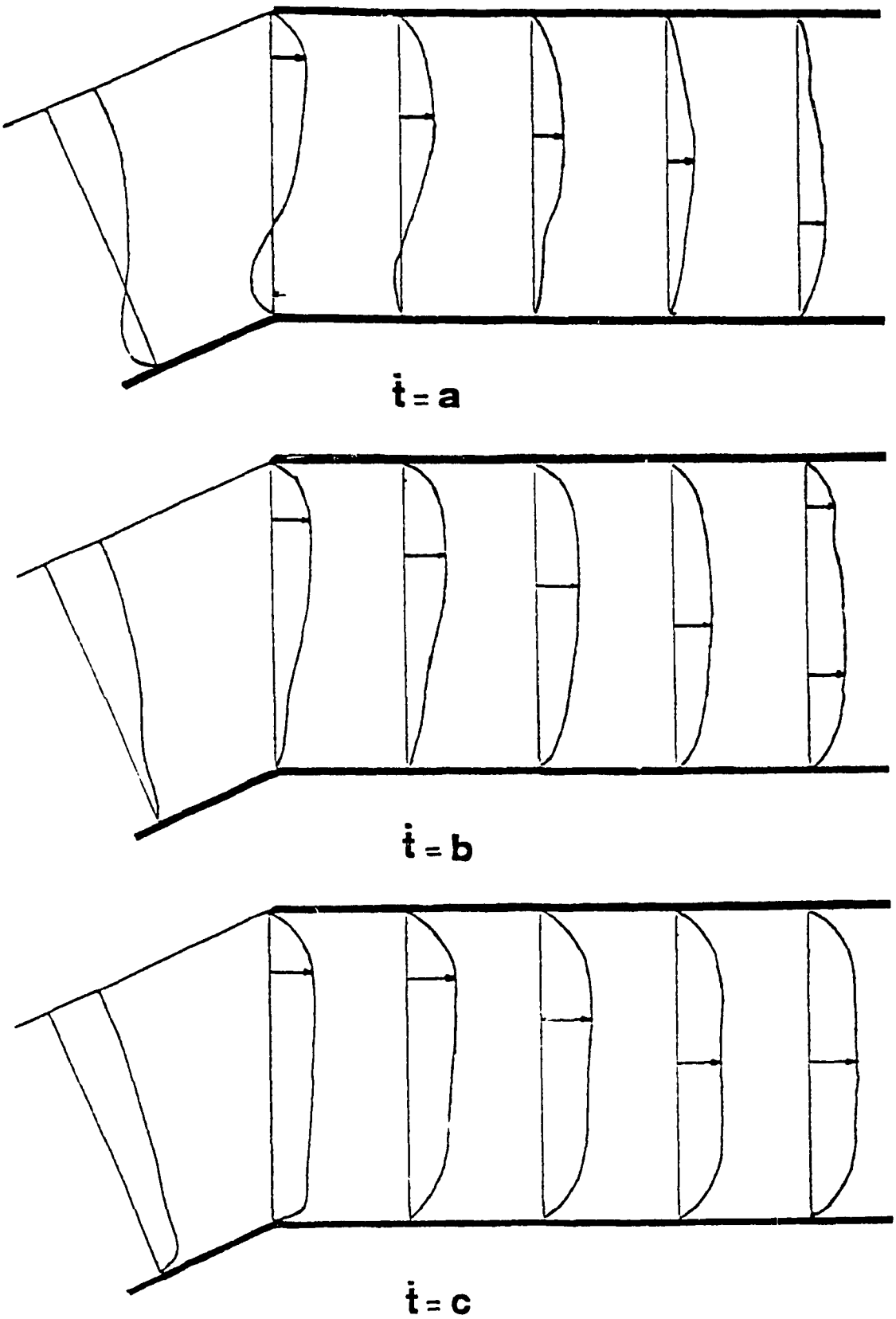

Fig. 41. Velocity profiles at the entrance of the daughter tube. The arrows show the position of maximum velocity

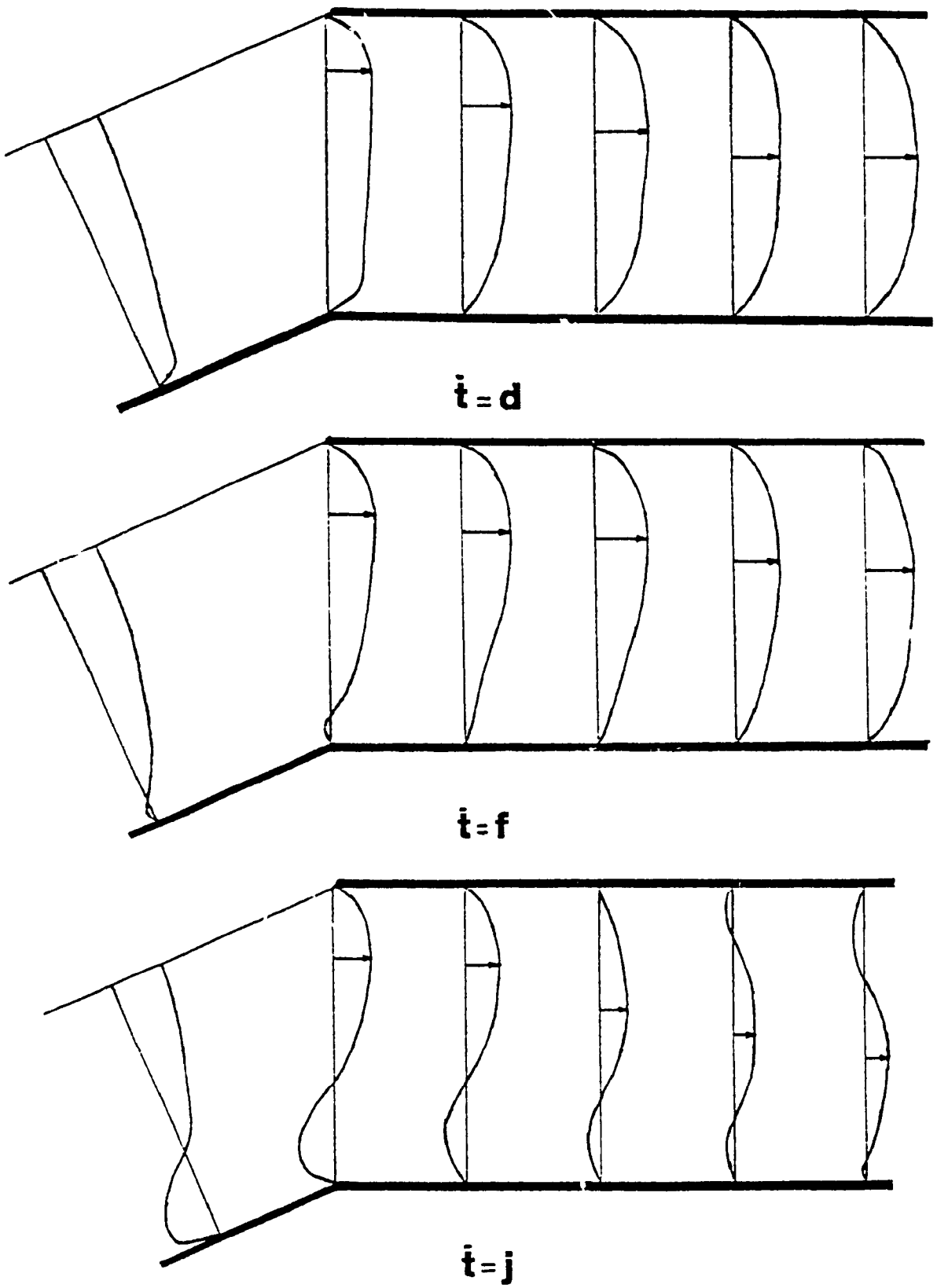

Fig. 42. Velocity profiles at the entrance of the daughter tube. The arrows show the position of maximum velocity

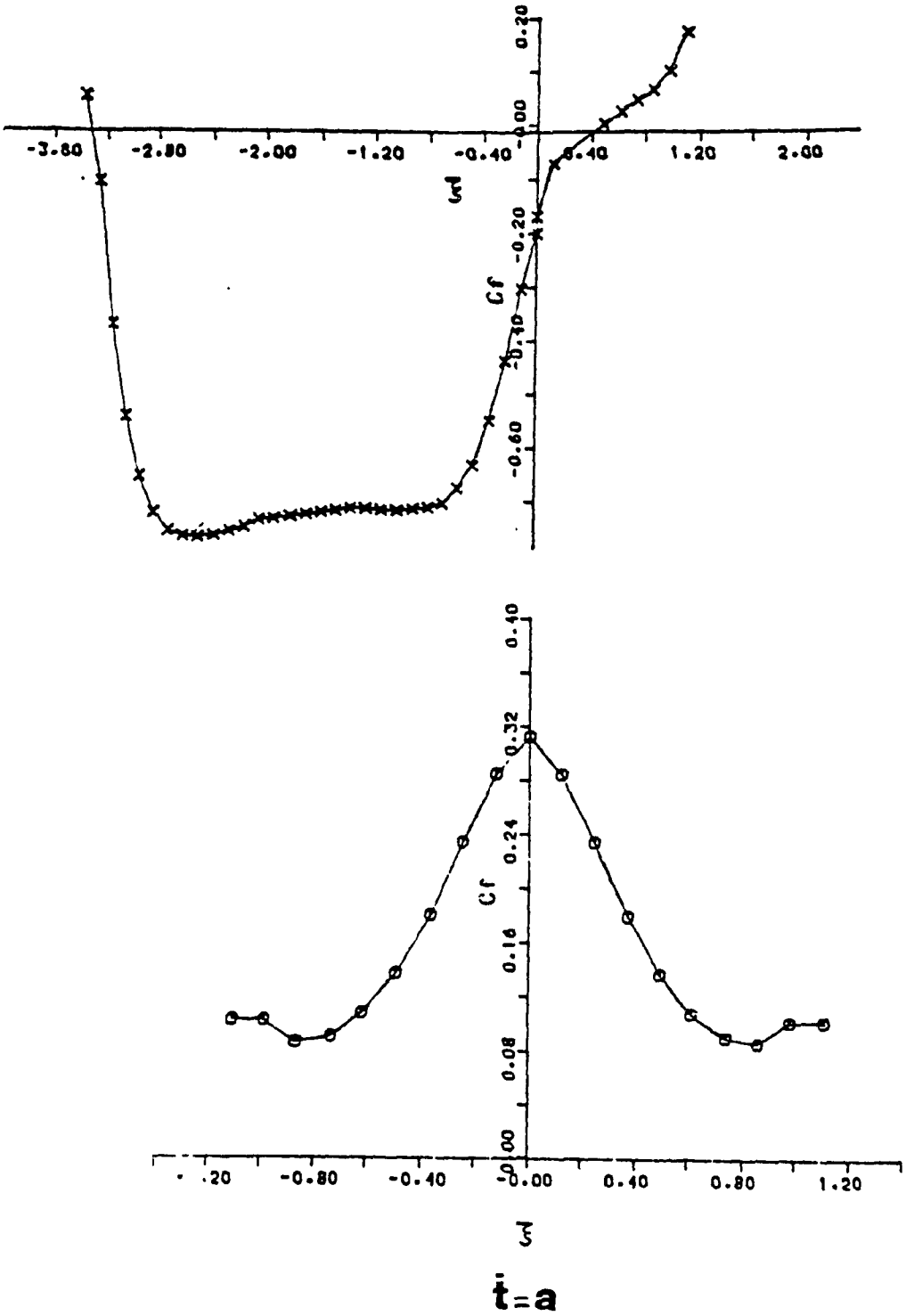

Fig. 43. C_f variation along the walls of the aortic model
(x - walls 1 and 2, 0 - wall 3)

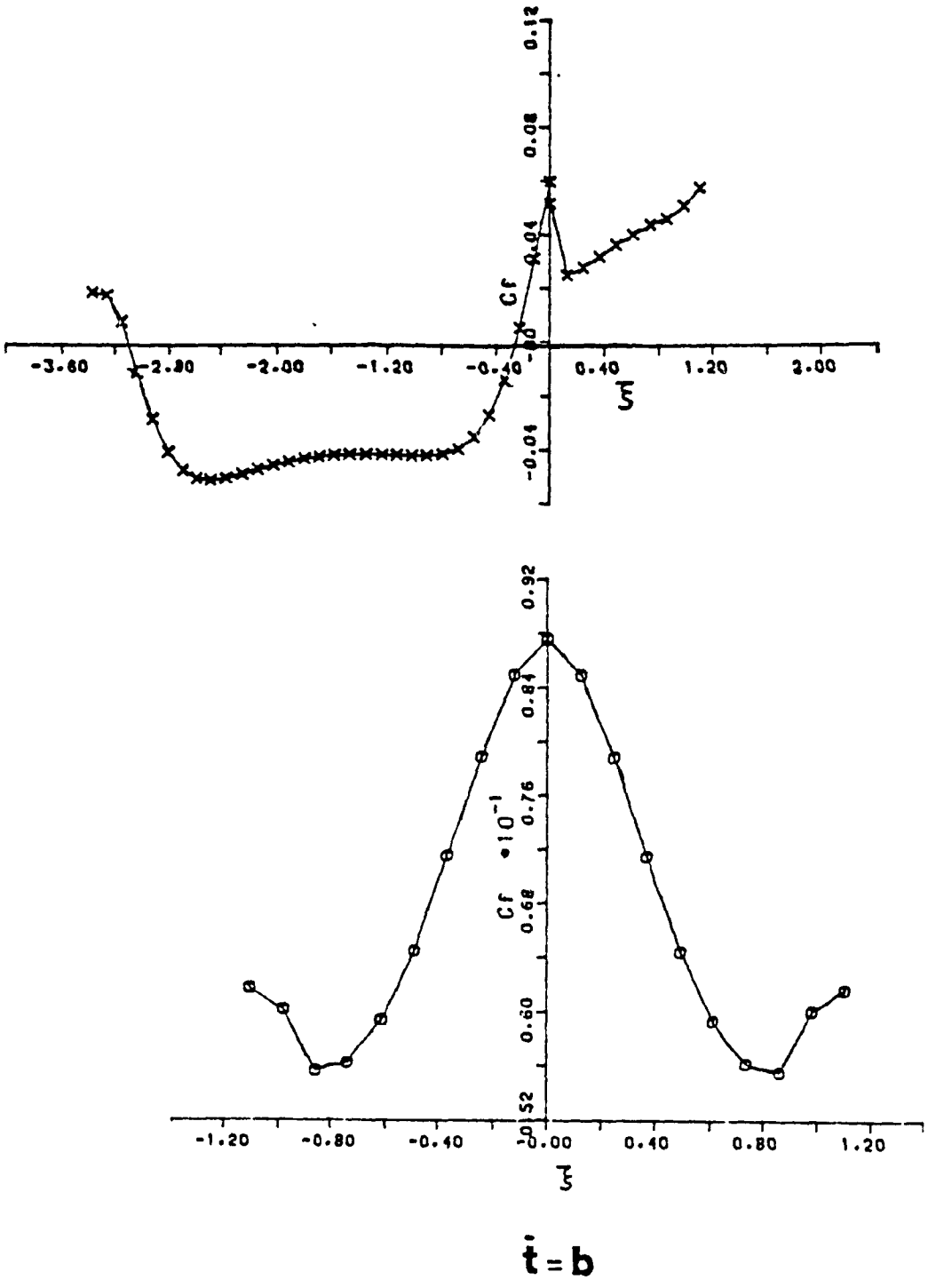

Fig. 44. C_f variation along the walls of the aortic model
(x - walls 1 and 2, 0 - wall 3)

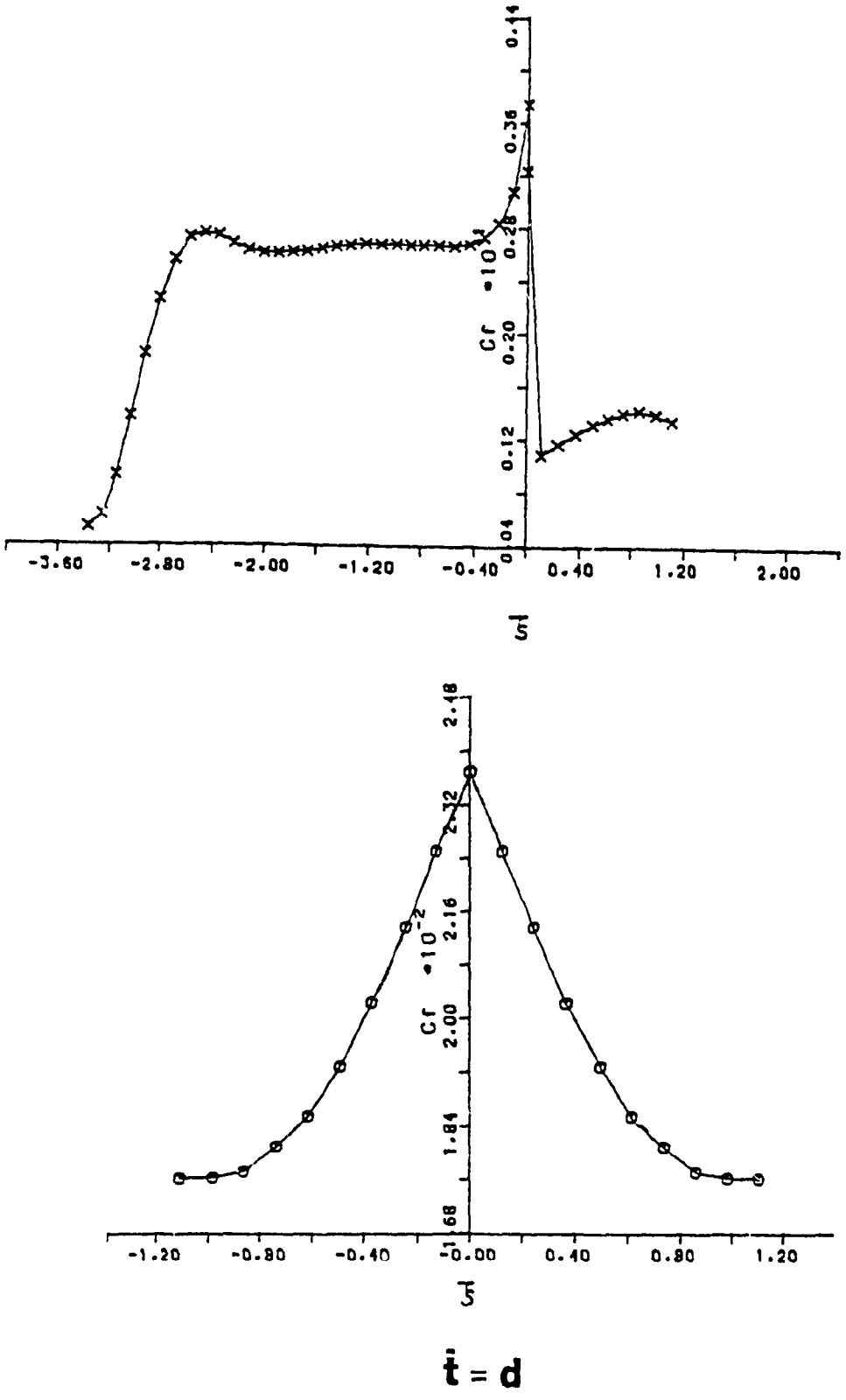

Fig. 45. C_f variation along the walls of the aortic model
(x - walls 1 and 2, 0 - walls 3)

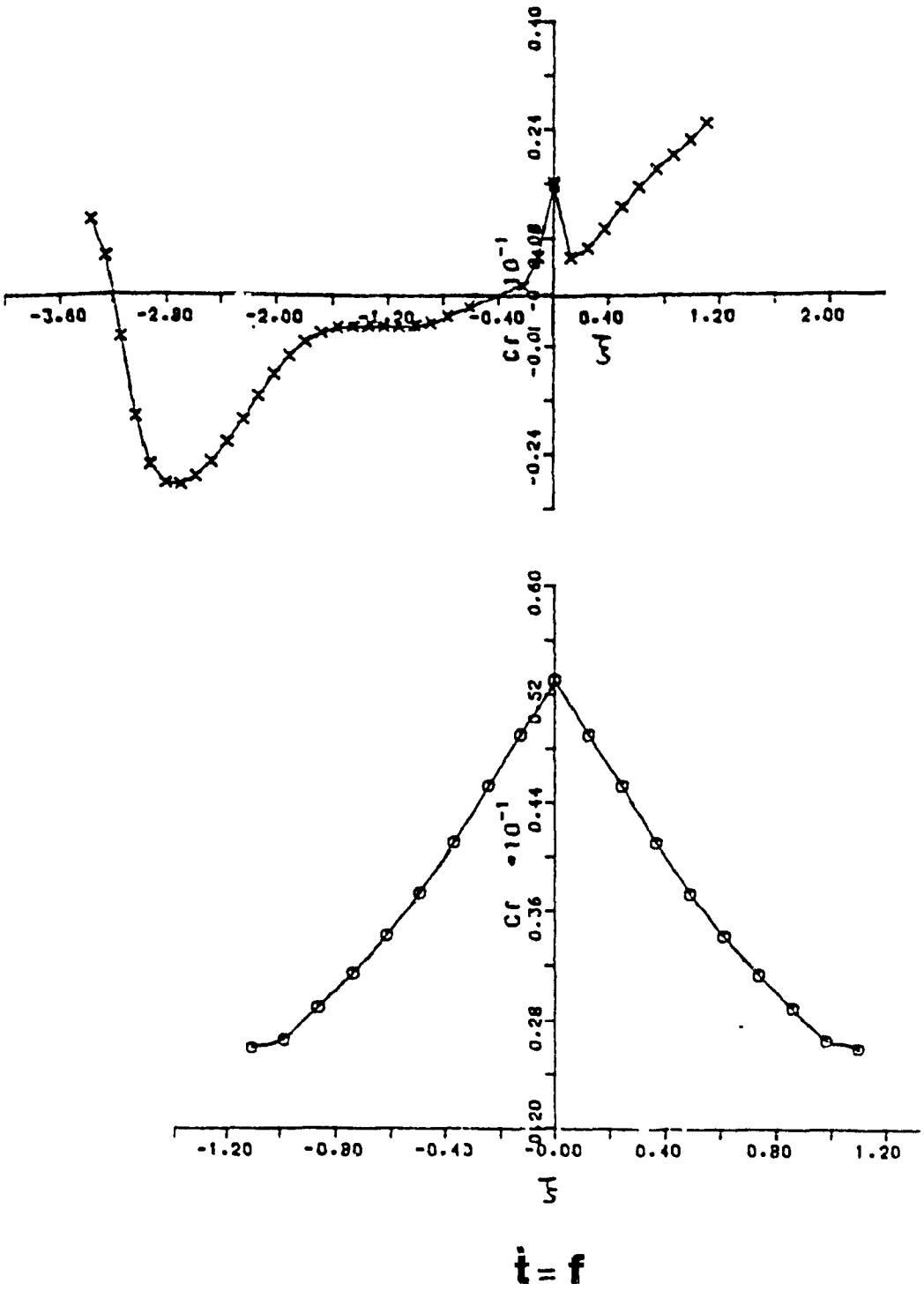

Fig. 46. C_f variation along the walls of the aortic model
(x - walls 1 and 2, 0 - wall 3)

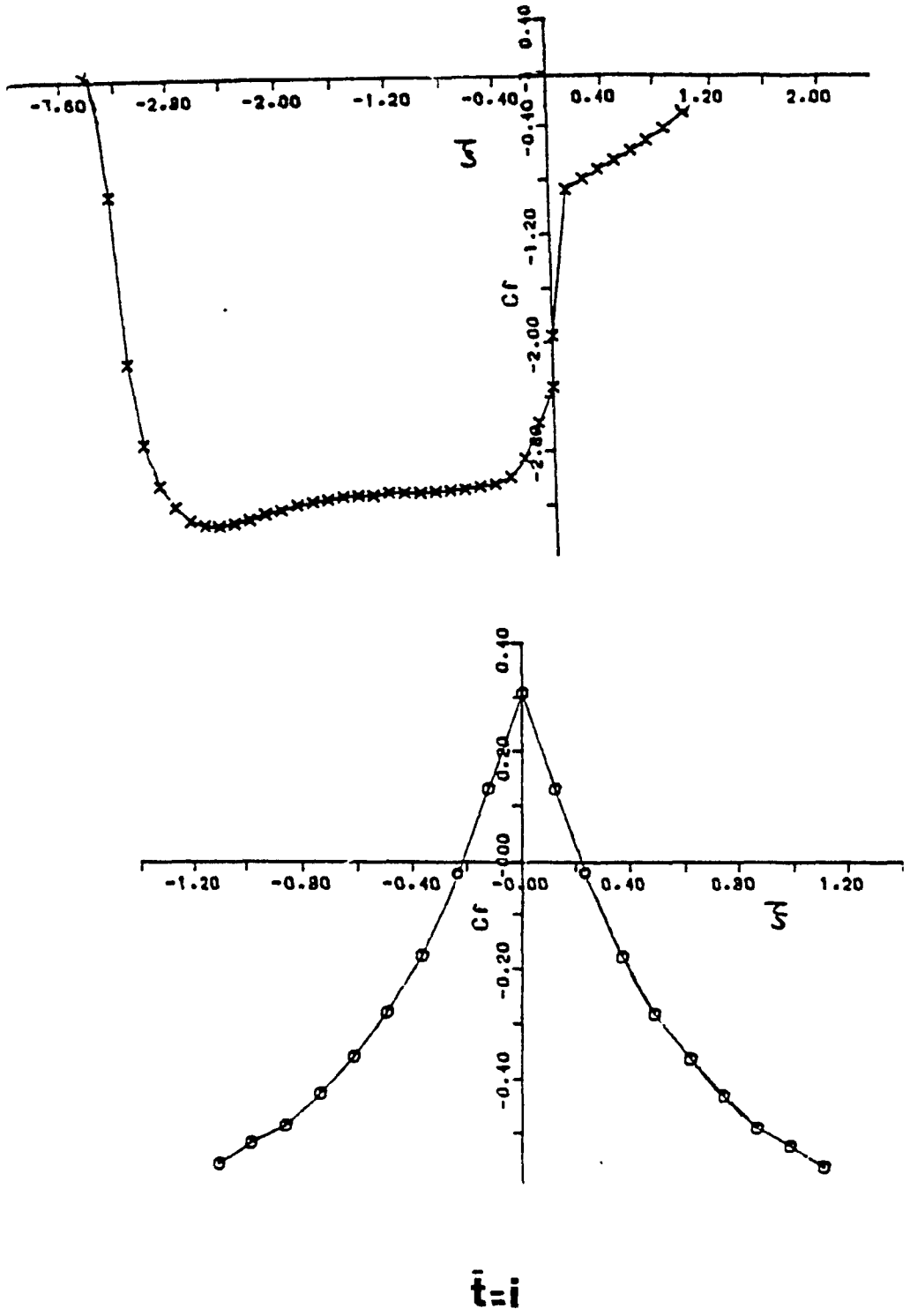

Fig. 47. C_f variation along the walls of the aortic model
(x - walls 1 and 2, 0 - wall 3)

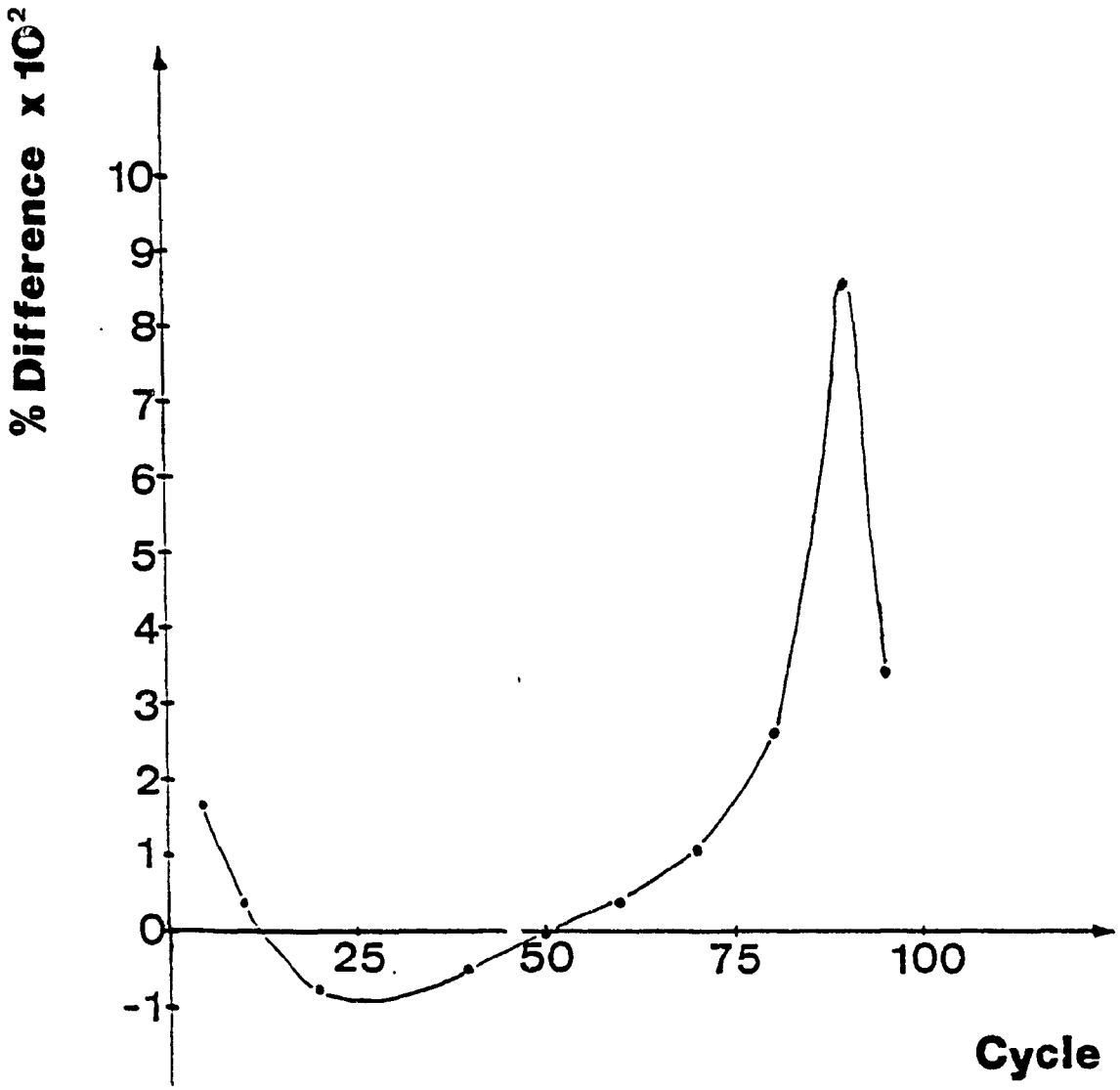

Fig. 48. Difference of C_f between the third and first walls, as a percentage of the third vs cycles

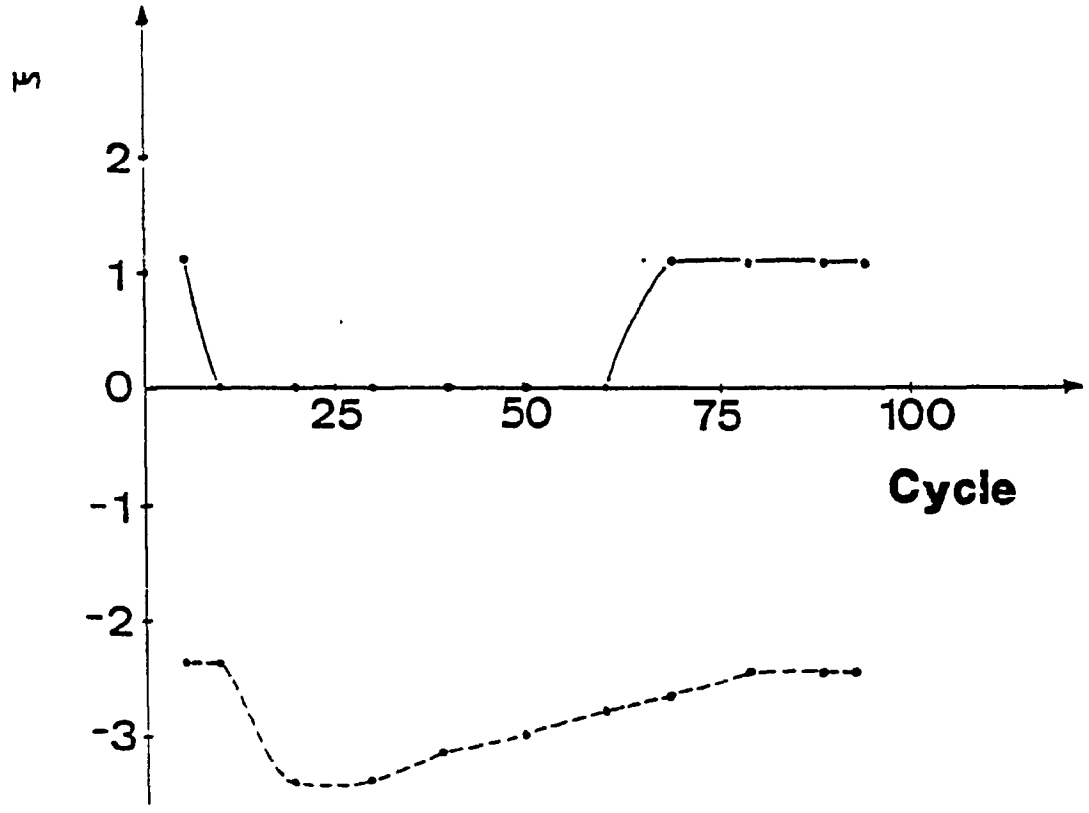

Fig. 49. Position of C_{fmax} (—) and C_{fmin} (---) for one period

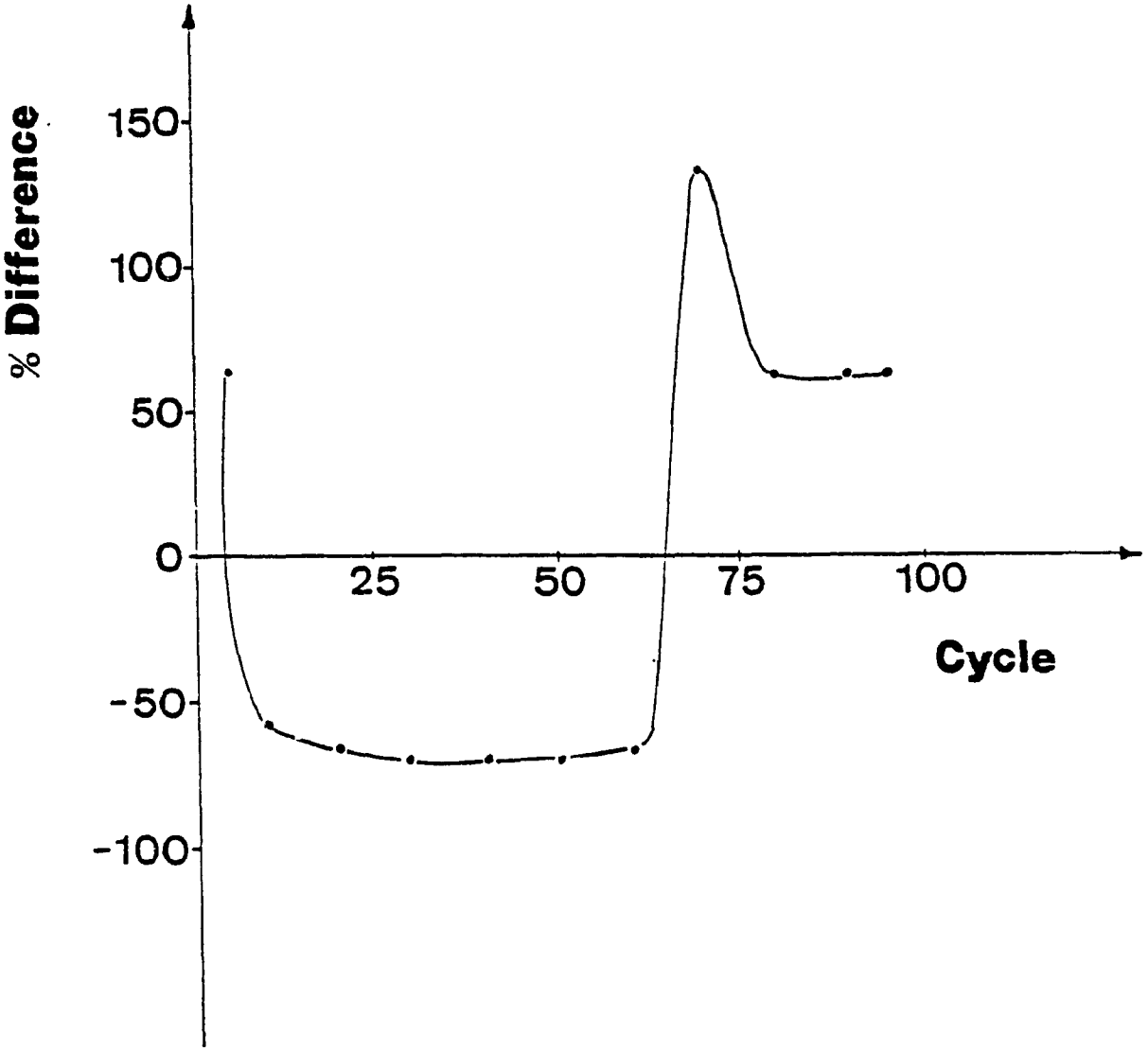

Fig. 50. Difference of C_f between points D and C, as a percentage of C_f at C, for one period

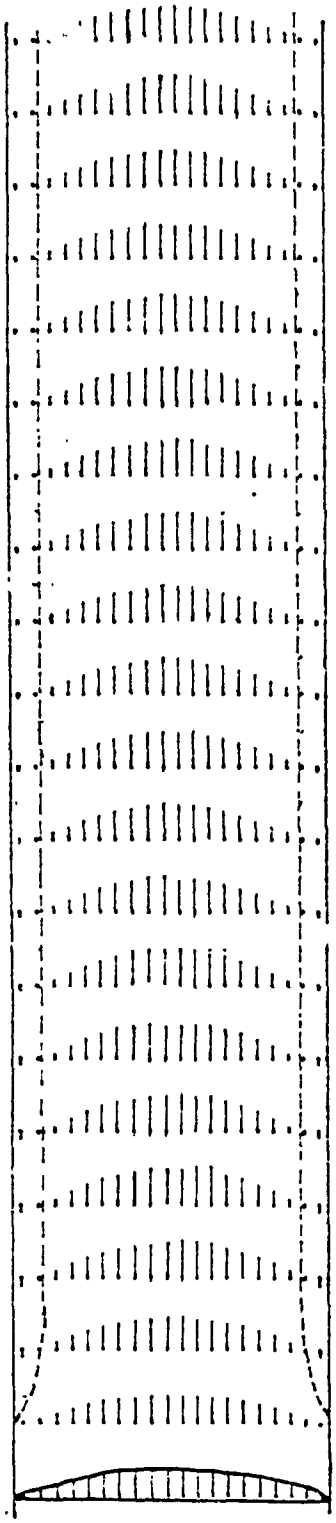

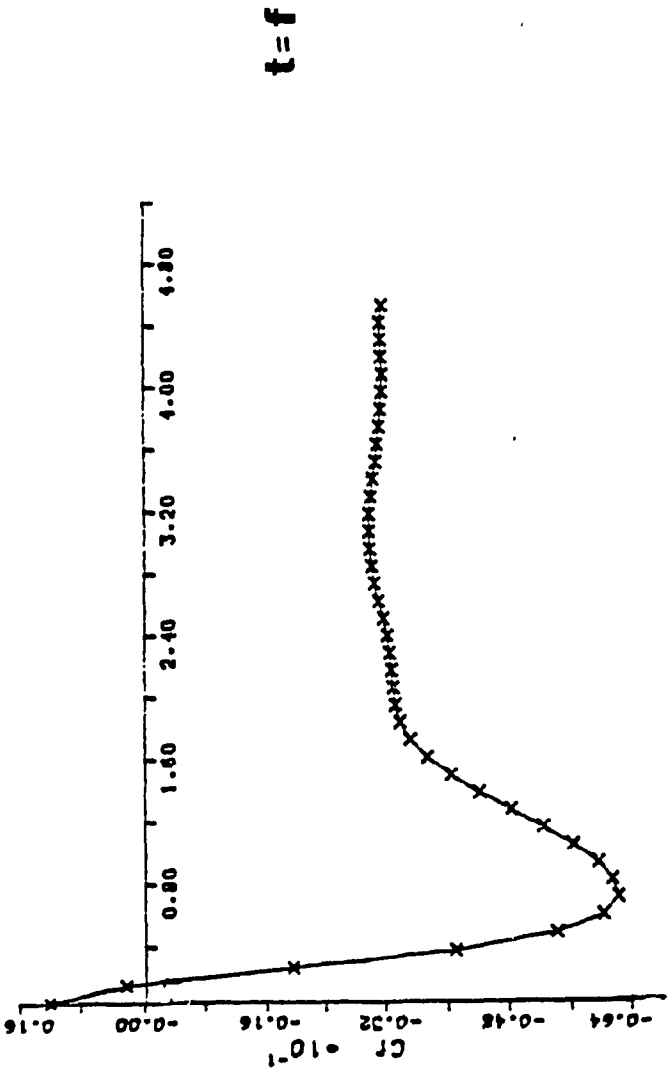

Fig. 51. Velocity profile and C_f variation along walls 1 and 2 for model III

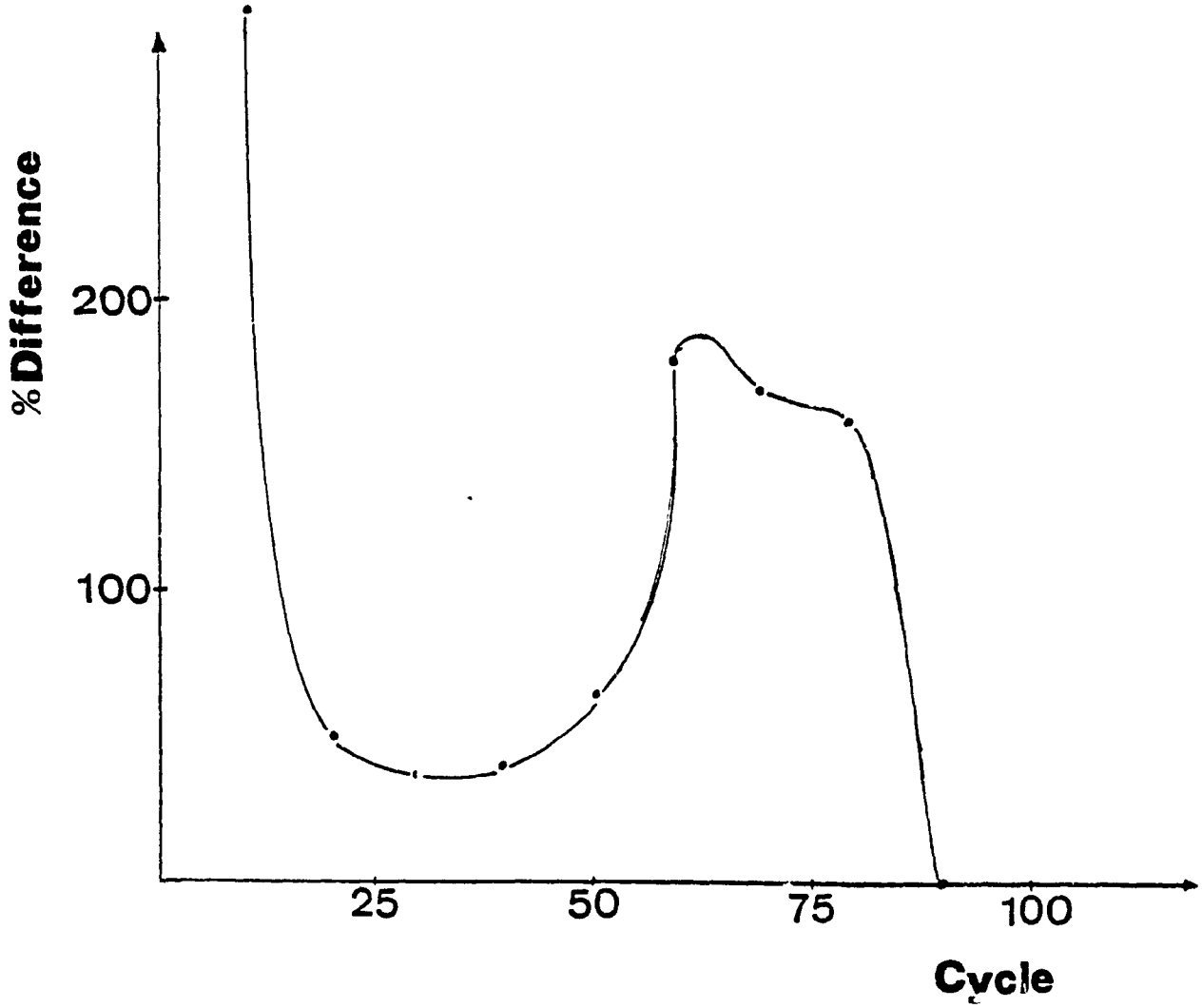

Fig. 52. Difference C_{fmax} between models I and III as a percentage of C_{fmax}, model III, for one period